GLACIOLOGICAL INVESTIGATIONS IN EAST GREENLAND USING DIGITAL LANDSAT IMAGERY

Anne-Marie Nuttall
Scott Polar Research Institute
University of Cambridge

Thesis submitted in partial fulfilment of the requirement for the degree of Master of Philosophy in Polar Studies

New Hall
June 1993

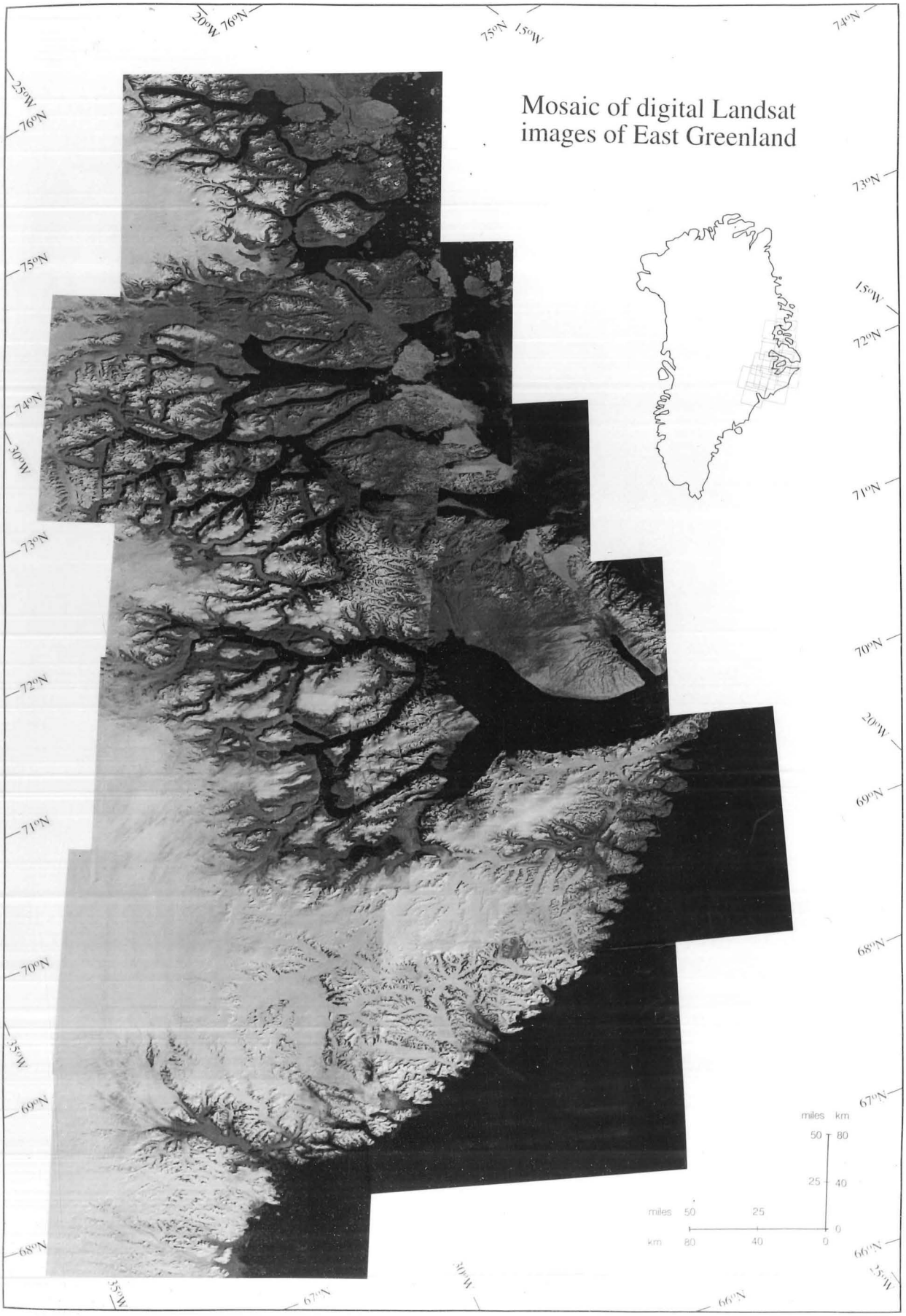
Mosaic of digital Landsat
images of East Greenland
miles km
50 80
25 40
0
miles 50 25 0
km 80 40 0

DECLARATION

In accordance with University of Cambridge regulations I hereby declare that this thesis entitled 'Glaciological Investigations in East Greenland Using Digital Landsat Imagery':

—represents my own original work and conforms to accepted standards of citation in those instances in which I have availed myself of the work of others.

—is not substantially the same as any I have submitted for a degree or diploma or other qualification at any other University

—does not exceed the prescribed limit of 20,000 words, excluding footnotes, tables, appendices and list of references.

Frontispiece: Mosaic of sixteen Landsat MSS band 4 scenes of East Greenland acquired in August or September between 1986 and 1989, as used in this study. Inset map shows location of scenes relative to Greenland. Note that images are distorted in the ratio 56 : 79 due to the rectangular shape of the pixels (see scale bar).

ABSTRACT

Sixteen late summer Landsat MSS scenes of East Greenland from 1986 to 1989 were acquired for use in glaciological and marine geological investigations. Drainage basin areas and snowline elevations were determined for 74 tidewater glaciers in the study area, and turbid meltwater plumes were identified.

A method of correcting digital Landsat MSS data for the effects of atmospheric haze has been developed and tested. The method consists of subtracting the radiance value of clear, open water measured in each of the four bands from the total radiance of each band. Verification of the haze correction technique, by comparing two overlapping scenes acquired two days apart, showed that the results were consistent to within 6% or less in all bands over four terrain types: bare ice, snow, bare rock and turbid lakewater.

Analysis of band 4 Landsat MSS data (0.8 to 1.1 μm) has been used to identify ice divides and drainage basin areas for tidewater glaciers in East Greenland between 67°N and 75°N. Basin areas ranged from approximately 50,000 km^2 for Daugaard-Jensen Gletscher and Kangerdlugssuaq Gletscher, both fast-flowing outlet glaciers draining the Greenland Ice Sheet, to about 20 km^2 for small local glaciers. The largest basins lie mostly outside the study area, and estimates of their area were obtained from published elevation maps, where available. Smaller glaciers could not be resolved because of problems with delineating their boundaries due to shadowing, new snow and surface moraine. The ratio of basin area to terminus width of a glacier was shown to give an indication of dynamic regime, as a glacier with a large drainage basin, but only a narrow terminus is likely to be fast flowing, and *vice versa*.

The late-summer snowlines were located for glaciers within the study area using MSS band 3 reflectance data (0.7 to 0.8 μm), and the elevations of these snowlines were determined from the published 1:250,000 topographic maps. A trend was seen in the snowline elevations increasing northwards from about 200 m for glaciers south of Kangerdlugssuaq Fjord (68°N) to over 1000 m at the head of Kejser Franz Josef Fjord (74°N). The reliability of these estimates was investigated by using overlapping imagery where possible, and it was seen that much of the variability in the values could be explained if the snowline was still rising on the earlier images, or if new snow had fallen shortly before acquisition of the

later images. Meteorological data and a time series of imagery would be needed to confirm this hypothesis.

Areas of higher reflectance in the vicinity of tidewater termini and river mouths were identified using MSS band 1 data (0.5 to 0.6 μm). These are interpreted to be turbid meltwater plumes, and this conclusion is supported by comparison with photographs from the field. Meltwater plumes are an important mechanism for transporting suspended sediments to the marine environment, and their presence implies that at least part of the glacier bed is at the pressure melting point or above, and thus gives an indication of the thermal regime of the glacier. Sediments deposited in the fjords and on the adjacent shelves form a record of the palaeoclimate of the polar North Atlantic and the fluctuations of the Greenland Ice Sheet. Information useful for the interpretation of sediment cores could therefore be obtained by studying the distribution of meltwater plumes and their variation with latitude and drainage basin area.

ACKNOWLEDGEMENTS

I would like to express my sincere gratitude to my supervisor, Dr Julian Dowdeswell for his thorough supervision and stimulating discussions. I have learnt a lot about rigorous scientific investigation and the intricacies of Arctic glaciology from him. Andy Diament taught me how to operate the image analysis system, and wrote the algorithms for the data correction and conversion described in Chapter 3. He was a very patient teacher and (nearly) always had the answers when I got stuck. Anne Jackson draughted some of the figures, for which I am most grateful, and Mark Brandon very kindly volunteered to develop the black and white screen photographs. I would like to thank Barry Rowe for taking the photograph of the frontispiece mosaic, and Bob Headland for putting me in touch with him. Stephen Wells, Ann-Britt Broström and Torben Christensen gave practical assistance and moral support in various ways. Anita Dey, Debra Enzenbacher and the two nightwatchmen, Ron and Dick, kept me company during the late night sessions, which became more frequent as time passed. The library staff at SPRI, Sharon, Shirley and Pat, were unfailingly helpful in locating references. Thank you to Peter Speak, MPhil course director, for arranging a stimulating series of seminars in the first two terms of the year.

A special mention must be made of my colleagues on the MPhil course and their families for their companionship and stimulating discussion. I discovered from them that the social and physical sciences have a lot to learn from each other, and I hope they feel the same way.

I acknowledge the support of the Brian Roberts Fund, which enabled me to attend a workshop at the Byrd Polar Research Center in Ohio. This was a valuable and interesting experience, and gave me a useful insight into the broader context of Arctic research.

Finally, thanks must go to my parents for their patience and moral support.

CONTENTS

Chapter 1

INTRODUCTION

1.1 BACKGROUND

The Greenland Ice Sheet is the second largest ice mass in the world after Antarctica, and is by far the largest in the northern hemisphere. It acts as a vast reservoir of fresh water, and currently accounts for 7% of the world's total. The ice sheet gains mass in the form of snow, which is formed as moist air from the North Atlantic rises and cools over the elevated interior of the ice sheet. In the interior, this snow is slowly compacted by the weight of subsequent snowfalls, and eventually becomes ice, which gradually begins to deform and flow outwards towards the coasts. Here the ice is either melted on the surface or at the bed of the glacier, or eventually reaches the sea and calves as icebergs.

In either case, the water is returned to the oceans, and as long as the rate at which mass is gained equals the rate at which it is lost, then a balance is maintained. If the ice sheet is losing mass by melting or calving faster than it is accumulating snow, then water is effectively being released from the 'reservoir' to the oceans, and sea level will rise as a result. For this reason, it is important to determine the mass balance of the Greenland Ice Sheet, and understand its response to changes in climate, either natural or anthropogenic.

Due to the vast extent of the ice sheet and the difficulties associated with fieldwork in this harsh and remote environment, very little was known about the ice sheet until the technological advances of the last few decades enabled a new approach to be taken. Airborne and satellite remote sensing techniques have revolutionized the study of glaciology in Greenland and elsewhere, as repeated synoptic measurements of many parameters can now be obtained. However, detailed information on basic parameters such as the surface topography have, to date, only been determined for some areas due to constraints imposed by the satellite orbits. Largely due to difficulty of access, the basic glaciology of East Greenland is particularly poorly known. Field observations of precipitation, melting, iceberg calving rates and flow velocities are very limited, and remote sensing techniques are therefore especially applicable in this area.

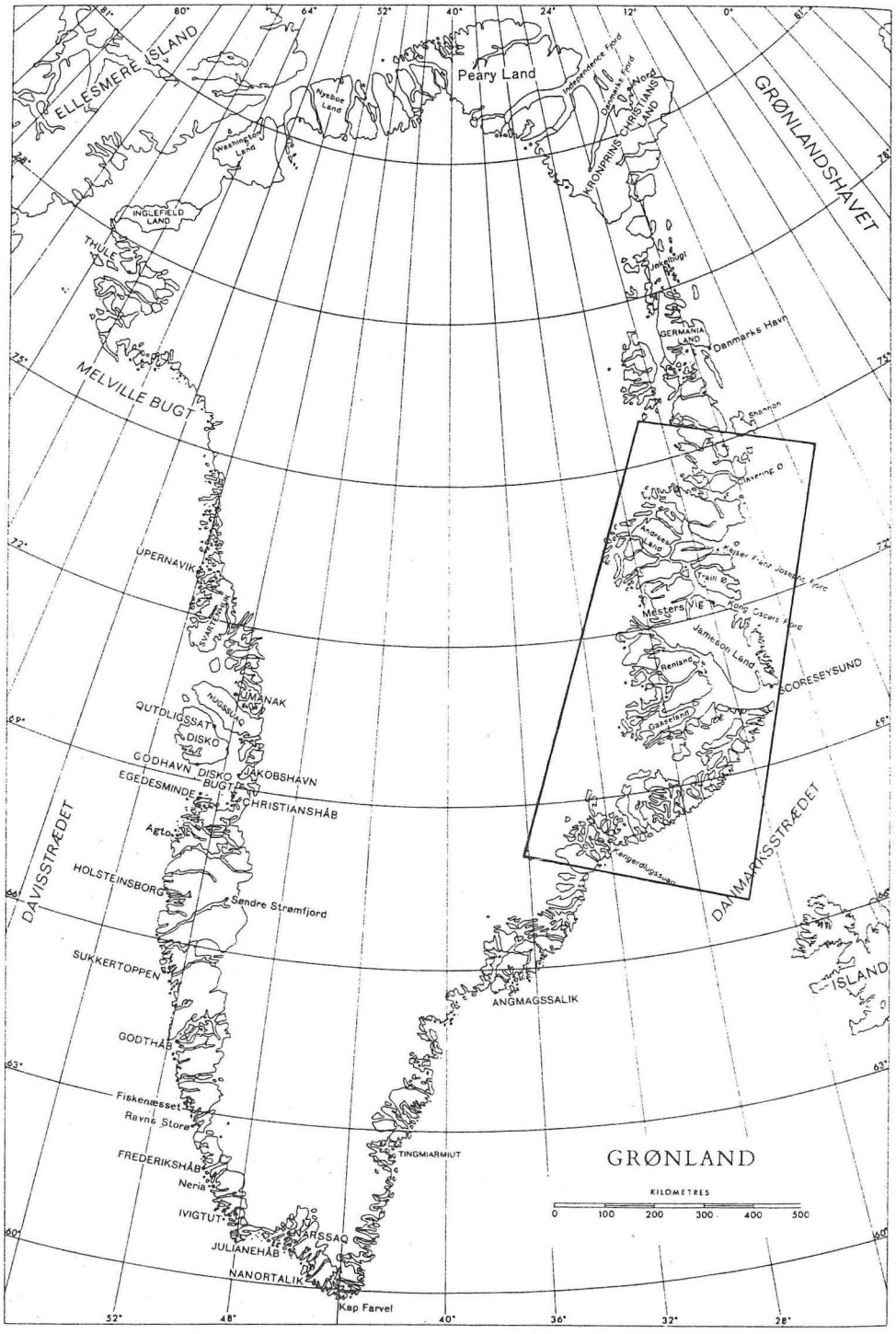

Figure 1.1 Map of Greenland showing location of the study area.

1.2 STUDY AREA

The study area covers nearly 1000 km of the coastal margin of East Greenland from about 68° to 75°N, as shown in Fig. 1.1. This area encompasses the extensive fjord systems of Kangerdlugssuaq, Scoresby Sund, Kong Oscars and Kejser Franz Josef Fjords, as well as the many islands and peninsulas which characterize this part of the Greenland coast. Figure 1.2 shows an outline map of the study region giving place names used in the text.

Glaciologically, this region comprises several large, fast-flowing outlet glaciers draining the Greenland Ice Sheet, of which Daugaard-Jensen and Kangerdlugssuaq Gletschers (Fig. 1.2) are the largest, together with a number of intermediate and smaller glaciers. Many of these smaller glaciers drain the ice cap occupying the Geikie Plateau, and form a complex flow pattern independent of the main ice sheet. North of Scoresby Sund, the glaciers become more widely spaced, an the frequency of small local glaciers decreases.

The dataset for this study consists of 16 Landsat Multi-Spectral Scanner (MSS) images acquired in late summer over the years 1986 to 1989. For the Scoresby Sund region, there is considerable overlap between the images, and in two cases images were acquired of the same scene in two different years. The data thus form an extensive latitudinal transect, over a more limited time series.

1.3 AIMS OF THE STUDY

The aims of this study were to determine basic glaciological data for the tidewater glaciers of central East Greenland using digital Landsat MSS data, and to investigate the use of MSS data for identifying the presence of suspended sediment in near-surface waters. The glaciological parameters investigated for tidewater glaciers in the study area were the locations of the ice divides, the drainage basin areas, the widths of tidewater termini, and the elevations of the snowlines, as a step towards determining the mass balance of these glaciers.

The mass balance of the Greenland Ice Sheet has yet to be determined with sufficient accuracy to know whether it is currently gaining or losing mass on balance, as this requires detailed, accurate measurements of either surface elevation or accumulation and ablation rates over a very large spatial scale. One approach to determining the mass balance of the Greenland Ice Sheet is to determine the extent of the individual drainage basins, and to assess the mass balance of each individually, and this is the approach taken in this study.

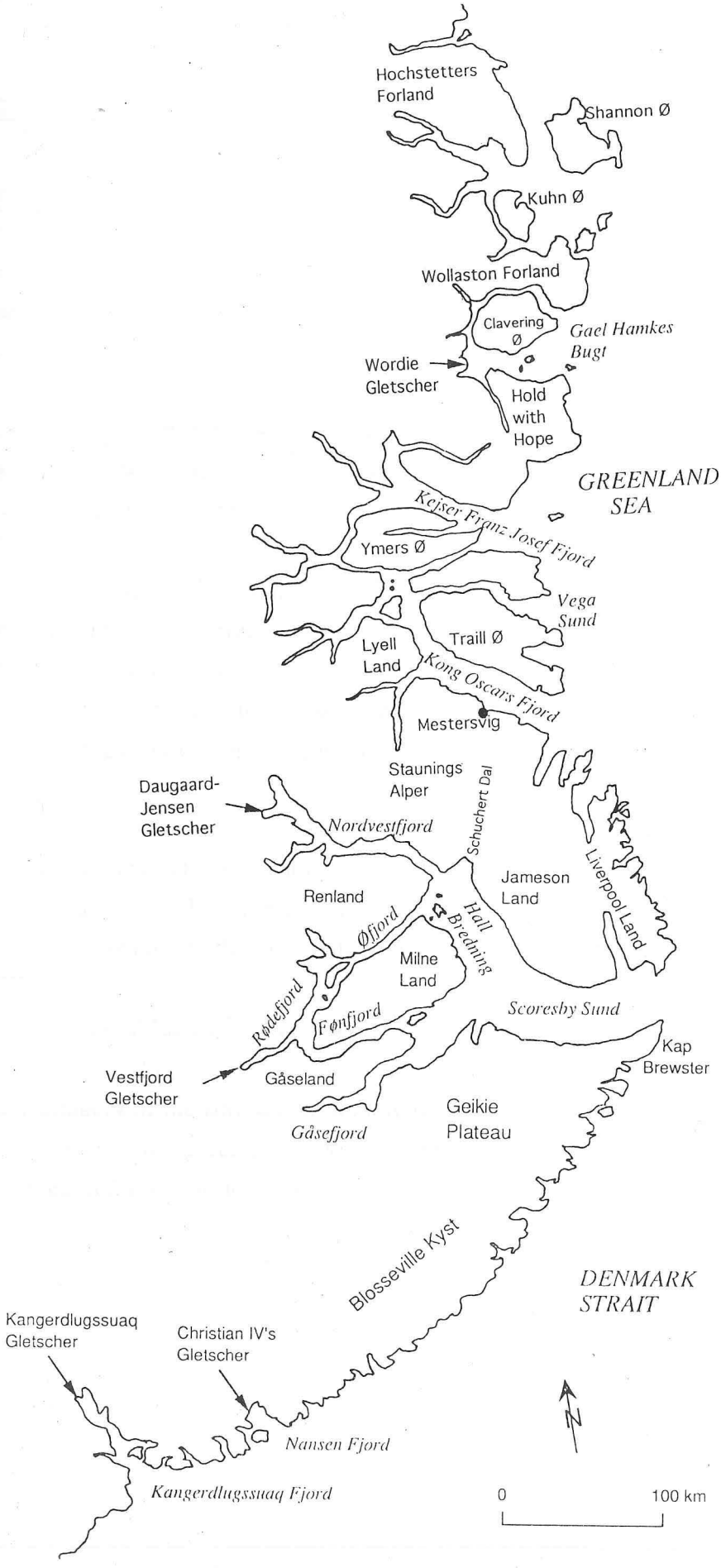

Figure 1.2 Outline map of the study area of East Greenland, giving place names used in the text.

1.4 STRUCTURE OF THE THESIS

Chapter 2 presents a summary of the characteristics of the Greenland Ice Sheet, and the current state of knowledge about the glaciology of East Greenland. The bedrock geology and Late Quaternary history of the ice sheet are outlined, as far as they are relevant to the present day glaciology.

To be able to compare quantitative results between scenes, it was necessary to correct for the effects of solar elevation and varying degrees of atmospheric haze at the time of acquisition. The digital values recorded at the satellite were then converted to physical values of reflectance. These procedures are described in Chapter 3.

The methods used to determine ice divides, drainage basin areas and terminus widths from digital imagery are described in Chapter 4. The results for each of the 74 tidewater glaciers within the study area are presented in the form of tables and maps. The ratio of drainage basin area to terminus width was examined, and compared to observed values of flow velocity and iceberg calving rates where available.

In Chapter 5, the elevations of the late-summer snowlines are determined for each of the tidewater glaciers in the study area using reflectance profiles extracted from the MSS band 3 digital data. The elevation of the snowline is an indication of the mass balance of a glacier, and so trends in the mass balance with latitude and continentality can be inferred.

The use of digital Landsat data to identify near-surface suspended sediments is investigated in Chapter 6. Turbid meltwater plumes off the coast of East Greenland are identified on the band 1 imagery of the Blosseville Kyst region, which shows that the basal temperature of at least some of the glaciers is above the pressure melting point. The glaciological and marine geological implications of the presence and distribution of such plumes are discussed.

Chapter 2

REGIONAL GLACIOLOGY OF EAST GREENLAND

In this chapter, the factors influencing the glaciology of the Greenland Ice Sheet as a whole are described, as a background for understanding the constraints on the glaciological system of East Greenland. The current state of knowledge specific to East Greenland is then summarised. The bedrock and marine geology are outlined as far as they are relevant to the glaciology, and the present state of the ice sheet is discussed in the context of Late Quaternary glacial-interglacial cycles.

2.1 INTRODUCTION TO THE GLACIOLOGY OF GREENLAND

2.1.1 Surface Topography and Ice Thickness

The Greenland Ice Sheet covers an area of about 1.7 million km^2 or 78% of the total area of Greenland, and accounts for 7% of the world's fresh water (Holtzscherer & Bauer, 1954; Radok *et al.*, 1982). Local glaciers account for a further 65,000 km^2 or 3% of the land area, leaving 19% ice-free (Weidick, 1985). The general features of the surface topography are a large dome occupying the north and central areas, and a smaller southern dome. The elevations of these domes are 3200 m and 2830 m respectively, with the saddle reaching about 2500 m (Fig. 2.1). The bedrock under the ice sheet is below the present sea level in the centre of Greenland and generally rises towards the margins reaching 1500 m above sea level in parts of East Greenland (Radok *et al.*, 1982). The combination of the roughly parabolic surface topography and the slightly bowl-shaped bedrock ensures that the ice sheet is thickest in the centre, with a maximum measured thickness of 3420 m, and thins increasingly rapidly towards the coasts (Fig. 2.2). Ice thicknesses over the Greenland Ice Sheet were obtained by airborne radio-echo sounding during the Greenland Ice Sheet Program (GISP) in 1971-82. To determine the bedrock topography, these thicknesses were subtracted from surface elevations as obtained by aircraft pressure altimetry, or more recently satellite radar altimetry up to 72 ^{o}N (Bindschadler *et al.*, 1989). Given the large area of the ice sheet, these data are necessarily sparse, and detailed elevation data are only

available for a few areas, mostly in southern and western Greenland. The new ERS-1 satellite radar altimeter (launched July 1991) is expected to provide detailed elevation data up to 82° N/S, which will significantly improve our knowledge of the topography of North and East Greenland, as well as much of Antarctica (Ridley *et al.*, 1992).

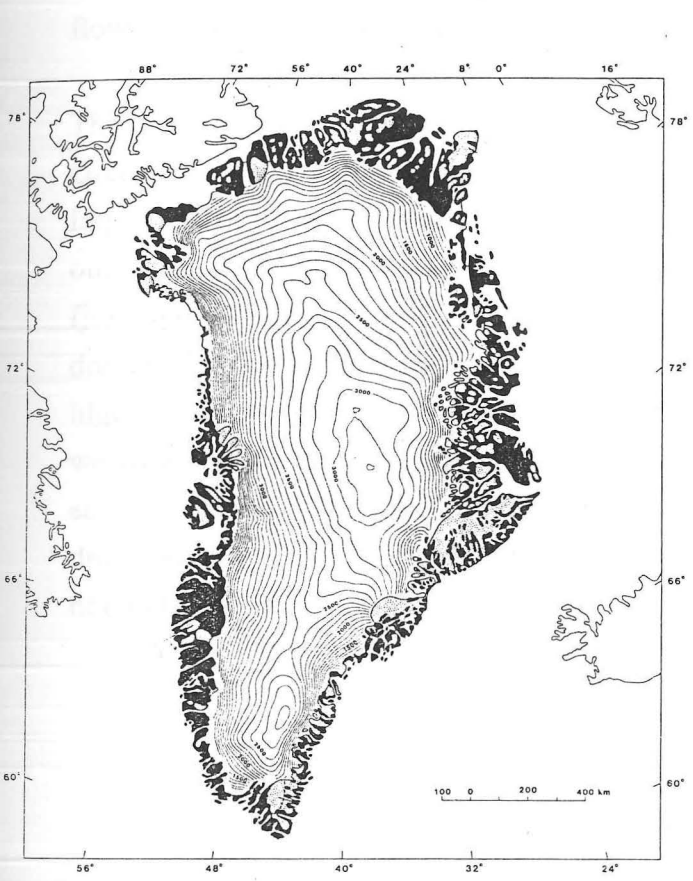

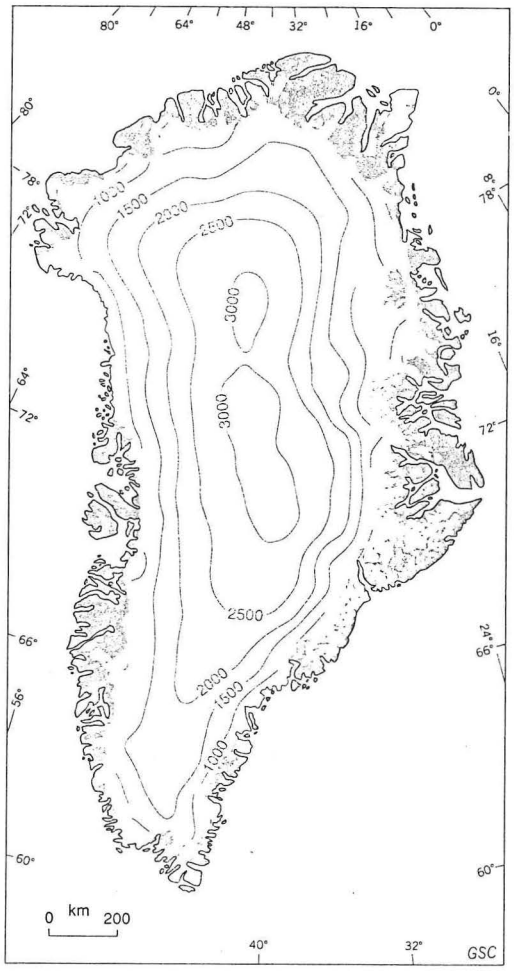

Figure 2.1 (left) Elevation map of the Greenland Ice Sheet with a 200 m contour interval, showing northern and southern domes. Dotted areas indicate major local glaciers and ice caps (from Weidick, 1992).

Figure 2.2 (right) Ice thickness map of the Greenland ice sheet, with a 500 m contour interval (from Reeh, 1989, after Radok *et al.* , 1982)

2.1.2 Ice Sheet Morphology and Dynamics

Ice generally flows outwards from topographic maxima in the direction of the maximum surface slope (Paterson, 1981), so a summit or a ridge acts as an ice divide. Hence, in Greenland, flow is away from the two domes and the connecting ridge, leading to an east-west flow from the main north-south divide towards the coasts. At least for the gentle surface gradients of the interior of Greenland, which are typically about 1 in 200 (Reeh,

1989), flowlines can be constructed by drawing a perpendicular to elevation contours, thus defining drainage basins (Fig. 2.3). This method works well for areas of gentle topography where the elevations are known in detail, but is not sufficient for coastal areas where steeper slopes and complex surface and bedrock topography are prevalent. In these areas, detailed investigation of the surface features and local elevations can be used to identify flow patterns and drainage basins (Chapter 4).

The pattern of bedrock topography also affects the flow pattern. In most coastal regions of Greenland, flow is restricted by mountain ranges to a few narrow valleys which means that large areas of the ice sheet drain through a small number of relatively narrow, fast-flowing outlet glaciers. Of these, Daugaard-Jensen Gletscher, at the head of the Scoresby Sund fjord system (Figs. 1.2 and 2.3), is the largest on the east coast and Jakobshavns Isbræ, draining into Disko Bugt (Figs. 1.1 and 2.3), is the largest on the west coast. The generally higher bedrock elevations in East Greenland mean that a larger area of the ice sheet drains westwards towards Baffin Bay and Davis Strait, hence shifting the ice divide closer to the east coast (Figs. 2.1 and 2.3). Weidick (1985) estimates that 408,000 km^2 of the ice sheet drains via East Greenland, while 627,000 km^2 drains to the west coast and the remaining 668,000 km^2 drains northwards.

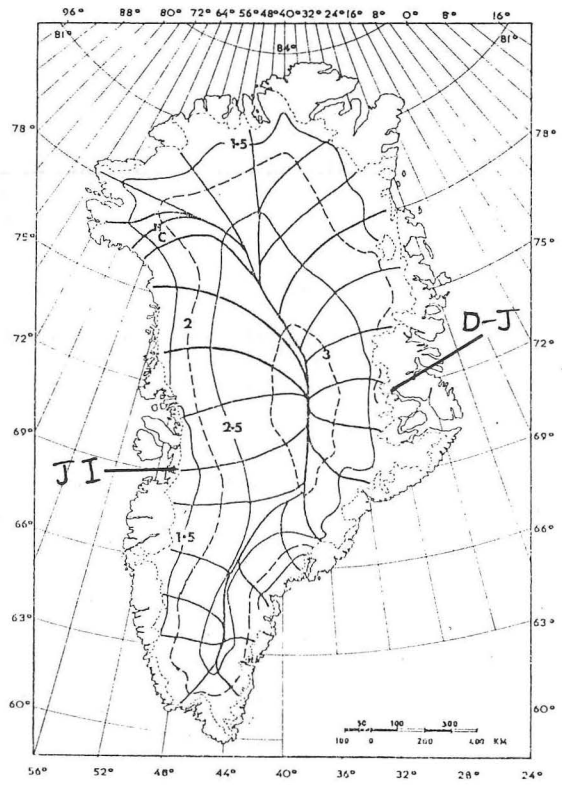

Figure 2.3 Flowline map of the Greenland Ice Sheet deduced from elevation gradients. Daugaard-Jensen (D-J) and Jakobshavn Isbræ (JI) basins are marked. (Budd *et al.*, 1982)

Horizontal velocities are theoretically zero at the central ice divide and increase outwards, attaining a maximum velocity which is dependent on the nature of the ice margin. For an ice margin terminating on land, and hence losing mass by melting, velocities are at most about 20 m yr^{-1}. By contrast, many Greenland glaciers drain a large inland area through a narrow outlet, and the resultant strongly convergent flow can produce velocities at the calving terminus of more than 20 m day^{-1} (>7 km yr^{-1}) (Lingle *et al.*, 1981). Jakobshavns Isbræ, which drains approximately $1.1x10^5$ km^2 of the ice sheet area (Fig. 2.3) through a terminus just 10 km wide (Bindschadler *et al.*, 1989), exhibits the fastest persistent flow velocities observed on any glacier in the world (Echelmeyer *et al.*, 1991).

2.1.3 Mass Balance of the Greenland Ice Sheet

The mass balance of an ice sheet is the change in mass due to accumulation and ablation, and is the primary link between climate and glacier response (Paterson, 1981, p.42). The ice sheet accumulates mass by precipitation, mainly in the form of snow, and loses mass by melting and iceberg calving. The law of mass conservation for an ice sheet can be expressed mathematically as:

$$\frac{\partial V}{\partial t} = Q_p - Q_m - Q_c \qquad \text{(Equation. 2.1)}$$

where $\frac{\partial V}{\partial t}$ is the rate of change of volume with time, Q_p is the annual precipitation, Q_m is the annual melting flux (comprising surface runoff, subglacial meltwater and basal melting from floating termini), and Q_c is the calving flux per year, all expressed as water-equivalent volumes. The detailed field measurements needed for an accurate assessment of mass balance are impractical for a large ice mass, so data are generally sparse. For this reason, it is not yet clear whether the Greenland Ice Sheet as a whole is gaining or losing mass, which is of importance for calculation of possible sea-level rise and global warming. Results so far indicate that the ice sheet is not significantly out of equilibrium with the present climate (Reeh, 1985), although the uncertainties are still large.

Satellite radar altimetry from the Geosat, Seasat and GEOS-3 satellites has been used to monitor changes in the elevation of the southern part of Greenland south of 72 °N (Zwally, 1989a, 1989b). It was concluded that this part of the ice sheet was thickening by 0.23 m/yr, although the accuracy of the results has been questioned due to uncertainties in the satellite orbits (Douglas *et al.*, 1990; Zwally *et al.*, 1990). The new ERS-1 radar altimeter will provide surface elevations up to 82° N and will help to resolve the question of surface

elevation changes, as well providing more accurate delineation of drainage basins for the whole ice sheet.

Net mass balance can be estimated directly by quantifying and summing the individual terms of the mass balance equation - precipitation, melting and iceberg production - or by measuring the mass balance as a whole by monitoring changes in surface elevation over time. An alternative approach is to estimate mass balance indirectly using proxy indicators such as the equilibrium line altitude (ELA) (see Section 2.1.7 and Chapter 5) (Braithwaite, 1984) or accumulation area ratio (AAR) (Meier & Post, 1962). The precipitation rates, melt rates, iceberg production and snowline elevations for the Greenland Ice Sheet are described in the following sections.

2.1.4 Precipitation Distribution

Precipitation over the ice sheet is estimated from accumulation rates recorded in firn pits and ice cores (Paterson & Waddington, 1984). Data have been compiled from many expeditions and surveys to produce a map of precipitation over the ice sheet (Fig. 2.4), which includes measured data from coastal stations. Data points on the ice sheet are widely spaced, particularly in the north and east, so the contours represent regional trends only. It can be seen from Fig. 2.4 that, although precipitation is very high in south-east Greenland (up to 200 g cm^{-2} a^{-1}), this drops off to more typical values towards Kangerdlugssuaq, and is further depleted towards north-east Greenland where only about 15 g cm^{-2} are received per year. Pilot studies for the drilling of an ice core on the isolated Renland Ice Cap, in the interior of Scoresby Sund, gave accumulation values of between 0.42 m and 0.52 m ice equivalent per year.

2.1.5 Surface and Basal Melt Rates

Melt rates from the ice surface have been studied in some areas of south-west Greenland in connection with planning of hydroelectric power schemes (Braithwaite & Thomsen, 1984) but other than this, very little is known about the rates of surface ablation by melting. Where melt rates over the whole ice sheet have been used in mass balance studies, these have been based on correlations between local meteorological conditions and observed surface melt rates from West Greenland (Braithwaite, 1980).

Echelmeyer *et al.* (1992) have studied ablation rates for Jakobshavns Isbræ as part of a mass balance assessment of the drainage basin, which occupies approximately 6% of the total area of the ice sheet. They estimated that the surface meltwater flux is 8–15 km^3 yr^{-1} which is approximtely 4–7 % of the total surface meltwater flux as estimated by Reeh (1985). Basal melting was calculated to be 2–3 km^3 yr^{-1}, or about 20% of the total

meltwater flux. The contribution due to basal melting from the floating ice tongue was not determined in this study, but could be significant, as over 100 km^2 of the terminus is floating (Echelmeyer *et al.*, 1991).

2.1.6 *Iceberg Production Rates*

A significant proportion of mass loss from the Greenland Ice Sheet is by iceberg calving from fast-flowing outlet glaciers fed by large drainage basins, although quantitative data are sparse. Echelmeyer *et al.* (1992) estimate that the ratio of calving flux to meltwater flux (surface and basal) is about 2:1 for Jakobshavns Isbræ, although this may be anomalously low due to the large ablation area. Direct observations of calving rates are particularly sparse for those parts of Greenland where pack ice is consistently found offshore, and hence are often inaccessible to ships (i.e. the north and east coasts). Figure 2.5 shows the estimated calving flux for each region of the coast, as compiled from observations of terminus velocities and thicknesses. Where observations are lacking, estimates are given from modelling studies, assuming steady state velocities (Reeh, 1985).

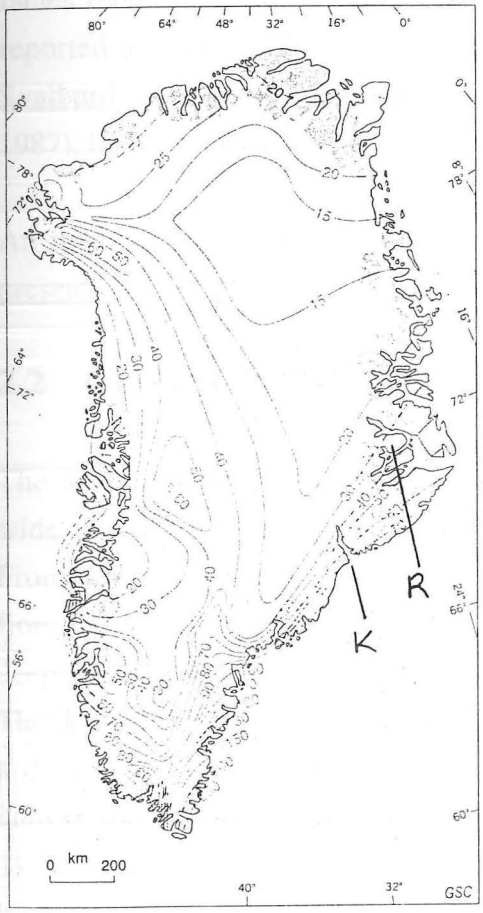

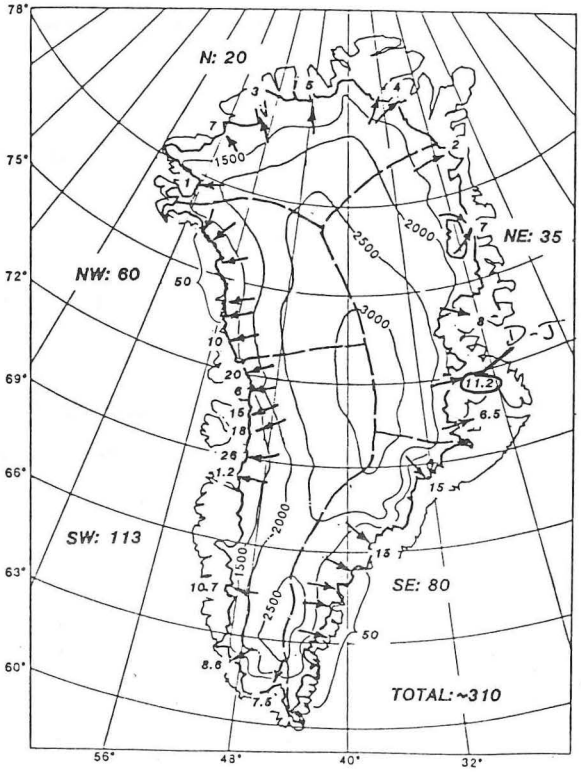

Figure 2.4 (left) Precipitation distribution for the Greenland Ice Sheet (g cm^{-2} yr^{-1}) (after Reeh, 1985). The locations of Kangerdlugssuaq (K) and Renland (R) are marked.
Figure 2.5 (right) Estimated iceberg calving fluxes for the Greenland Ice Sheet (km3 yr-1 water equivalent) (after Reeh, 1985). Daugaard-Jensen Gletscher (D-J) is indicated.

2.1.7 Snowline Elevations

The transient snowline on an ice mass at the end of the melt season has been shown to be approximately equivalent to the equilibrium line (Braithwaite, 1984), which is the line separating the accumulation zone from the ablation zone, and can thus be used as an indicator of mass balance (Paterson, 1981, p. 53). Reported values from the west coast of Greenland vary from about 1000 m in the north rising to about 1700 m in the south (Holtzscherer & Bauer, 1954; Benson, 1962; Braithwaite & Thomsen, 1984). Calculations of equilibrium line altitude (ELA) for the Jakobshavn area on the west coast for a period of 23 years show that there is considerable interannual variation, however. Although the average ELA between 1961 and 1983 was about 1300 m, individual years gave values from about 1000 m to 1450 m (Braithwaite & Thomsen, 1984).

Superimposed ice, which occurs when surface meltwater refreezes, is an important problem when determining the equilibrium line, as it blurs the distinction between snow facies representing accumulation and ice facies representing ablation zones. It has been reported to occur in West Greenland (Schytt, 1955; Echelmeyer *et al.*, 1992) as well as Svalbard (Jonsson & Hansson, 1990) and the Canadian Arctic (Gruell & Oerlemans, 1987), but it is not clear whether or not it is significant in East Greenland.

An investigation of snowline elevations in East Greenland using Landsat imagery is presented in Chapter 5.

2.2 GLACIOLOGY OF EAST GREENLAND

The Scoresby Sund fjord system, penetrating 350 km into the interior and up to 40 km wide, divides the east coast of Greenland into two distinct physiographic zones (Fig. 1.2). From Scoresby Sund northwards, the coastal region is characterised by complex branched fjord systems with wide, relatively shallow outlets, such as Hall Bredning (up to 600 m deep) leading in to the steep-sided, narrow and often extremely deep fjords of the interior. The deepest of these, Nordvestfjord at the head of the Scoresby Sund fjord system, attains a depth of about 1500 m. South of Scoresby Sund, the fjords are generally shorter, narrow and unbranched, with Kangerdlugssuaq being by far the longest at nearly 100 km. The terrain is alpine in style, with valley glaciers forming steep aretes and pinnacles. The highest mountains in Greenland occur in this area, with elevations of up to 3700 m. The Geikie Plateau occupies the peninsula between Christian IV's Gletscher and Scoresby Sund, and is largely covered by an ice cap which is connected to the main ice sheet, but has an independent flow regime (Fig. 4.4) (Bindschadler *et al.*, 1989). It is this ice cap which

feeds the numerous valley glaciers terminating in the short fjords along the Blosseville Kyst (Chapter 4).

In general, the east coast margin of the Greenland Ice Sheet is dominated by a few very large outlet glaciers. In the southern part, Kangerdlugssuaq Gletscher drains an area of approximately 50,000 km^2 (Bindschadler *et al.*, 1989) and, together with other less productive glaciers in the region, calves an estimated 15 $km^3\ yr^{-1}$ of ice (Fig. 2.5) (Reeh, 1985). Christian IV's Gletscher, draining into Nansen Fjord north of Kangerdlugssuaq (Fig. 1.2), has a wide terminus (Table 4.1), but does not appear to be very productive, based on the numbers of icebergs observed offshore (Koch, 1945).

Several major glaciers drain into the Scoresby Sund fjord system, which can be divided into a northern and a southern branch with Renland in between (Fig. 1.2). Daugaard-Jensen Gletscher, Charcot Gletscher and Graah Gletscher drain into the northern branch at the head of Nordvestfjord (Figs. 4.1 and 4.4). Olesen and Reeh (1969) estimated the total calving flux of the northern branch to be 11.2 $km^3\ yr^{-1}$, of which 10 $km^3\ yr^{-1}$ is from Daugaard-Jensen Gletscher. This estimate was based on their observations of a mean velocity of 10.2 m day^{-1}, terminus width of 5.7 km and a frontal height of 62 m; equivalent to a thickness of about 500 m. These velocities have more recently been confirmed by theodolite measurements, and the thickness estimates supported by observations of overturned icebergs (Reeh & Olesen, 1986). Dowdeswell *et al.* (1992) also found the modal keel depth of icebergs in the Scoresby Sund ford system to be 400 - 500 m with the largest keel depths occurring in Nordvestfjord. The drainage basin of Daugaard-Jensen Gletscher is of the order of 50,000 km^2 (Fig. 2.3), although the northern boundary of the basin is above the 72 °N limit of present satellite radar altimetry (Bindschadler *et al.*, 1989).

Rolige, Vestfjord and Magga-Dan Gletschers are the largest of the glaciers draining into the various fjords of the southern branch of the Scoresby Sund fjord system (Fig. 4.4, Table 4.3). Henriksen (1973) gives a calving flux estimate of 3.5 $km^3\ yr^{-1}$ for Vestfjord Gletscher, and unpublished results quoted in Reeh (1985) estimate the total flux of this branch to be 6.5 $km^3\ yr^{-1}$. In the absence of observations, steady-state modelling was used to calculate the calving flux for Kong Oscars and Kejser Franz Josef Fjords (Fig. 1.2), which was estimated to be 8 $km^3\ yr^{-1}$ in total (Reeh, 1985).

The drainage basins and terminus widths of all tidewater glaciers within the study area were delineated using digital Landsat data, and the results are presented in Chapter 4.

2.3 GEOLOGICAL AND GLACIAL HISTORY OF EAST GREENLAND

2.3.1 Bedrock Geology

The present geology of the ice-free margin of East Greenland falls into three major regions (Fig. 2.6). The southern section, from Kap Farvel to Kangerdlugssuaq consists of old crystalline rocks, such as gneisses, which are part of the Precambrian shield underlying much of the west coast and probably the ice sheet itself. The central section from Kangerdlugssuaq to Scoresby Sund consists of Tertiary volcanic rocks which form the Geikie Plateau with an elevation of about 2000 m. This area is deeply incised by valley glaciers, but the extensive fjords characteristic of the northern section of the coast are absent (Funder, 1989).

From the Scoresby Sund fjord system northwards (Fig. 2.6), the geology is dominated by Caledonian metamorphic and magmatic rocks which were formed from sediments deposited on the original Precambrian block (Funder, 1989). A major fault line running parallel to the coast, roughly along the present ice margin (Fig. 2.6), was caused by ocean floor spreading as the Norwegian Sea was formed (Escher & Watt, 1976). Minor faults also formed perpendicular to this line, which later determined the location of many of the fjords in this region during the ensuing glaciations (Fig. 1.2).

The main exception to this pattern is Jameson Land on the north side of Scoresby Sund (Fig. 2.6), which consists of Mesozoic sedimentary rocks overlain by much younger glacial deposits (Marienfeld, 1992). The topography of this area is also markedly more gentle, rising to only about 800 m.

2.3.2 Bathymetry and Marine Geology

The continental shelf off East Greenland developed as a sedimentary basin during ocean floor spreading in the early Tertiary, and accumulated up to 7 km of sediment during the Tertiary and Quaternary (Funder, 1989). In the northeast, the shelf extends to about 300 km offshore, decreasing to about 35 km in the far south (Fig. 2.7). In several places, substantial transverse channels cross the shelf at the mouths of the major outlet glaciers (Larsen, 1983). The channel off the mouth of Kangerdlugssuaq is about 50 km wide and 350 km long, for example (Larsen, 1983).

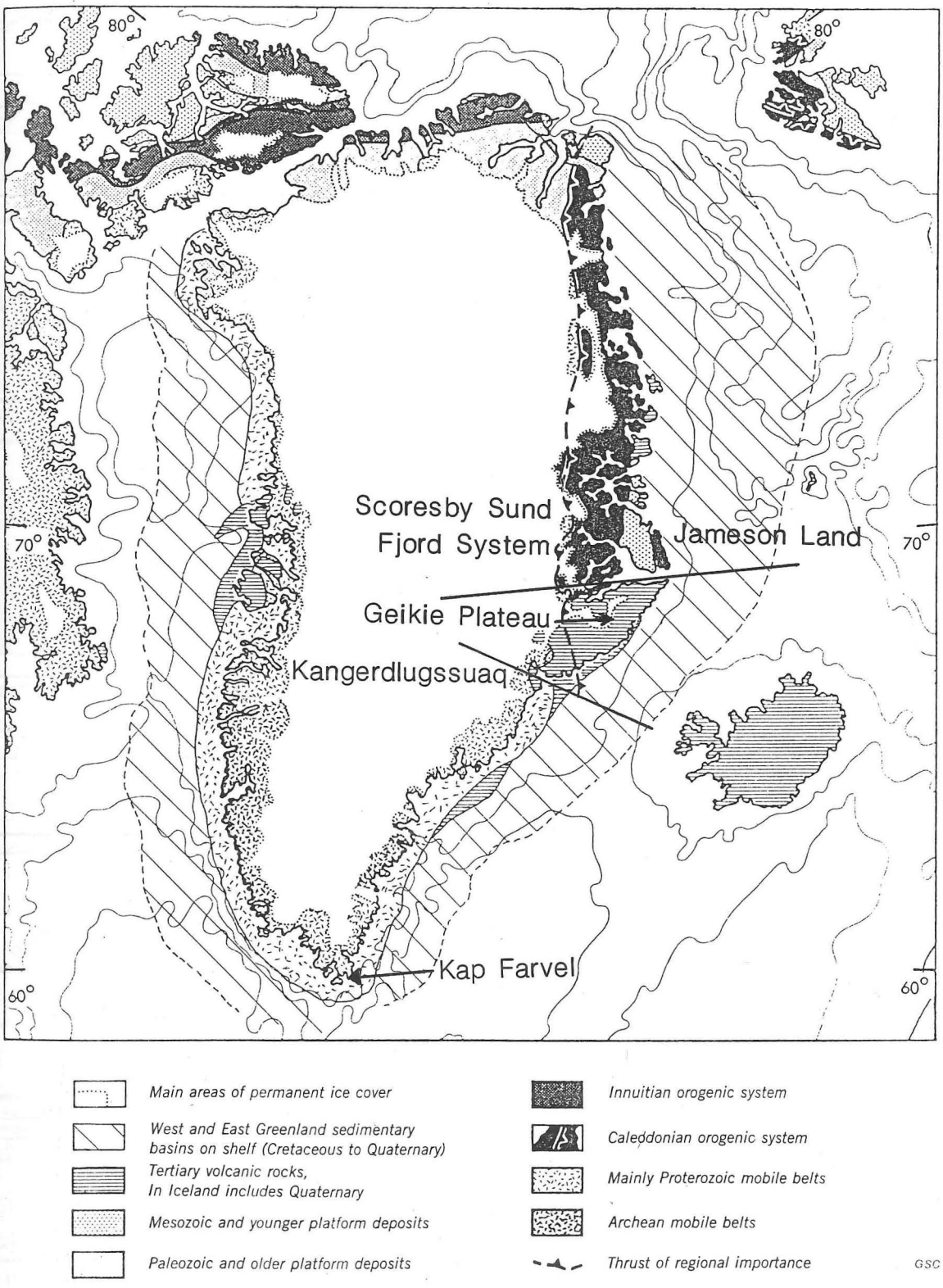

Figure 2.6 Geology of the ice free margins and shelves of Greenland. East Greenland can be divided into three geological regions, as indicated, with Jameson Land being the major exception (from Funder, 1989). Note the major fault parallel to the north-east coast.

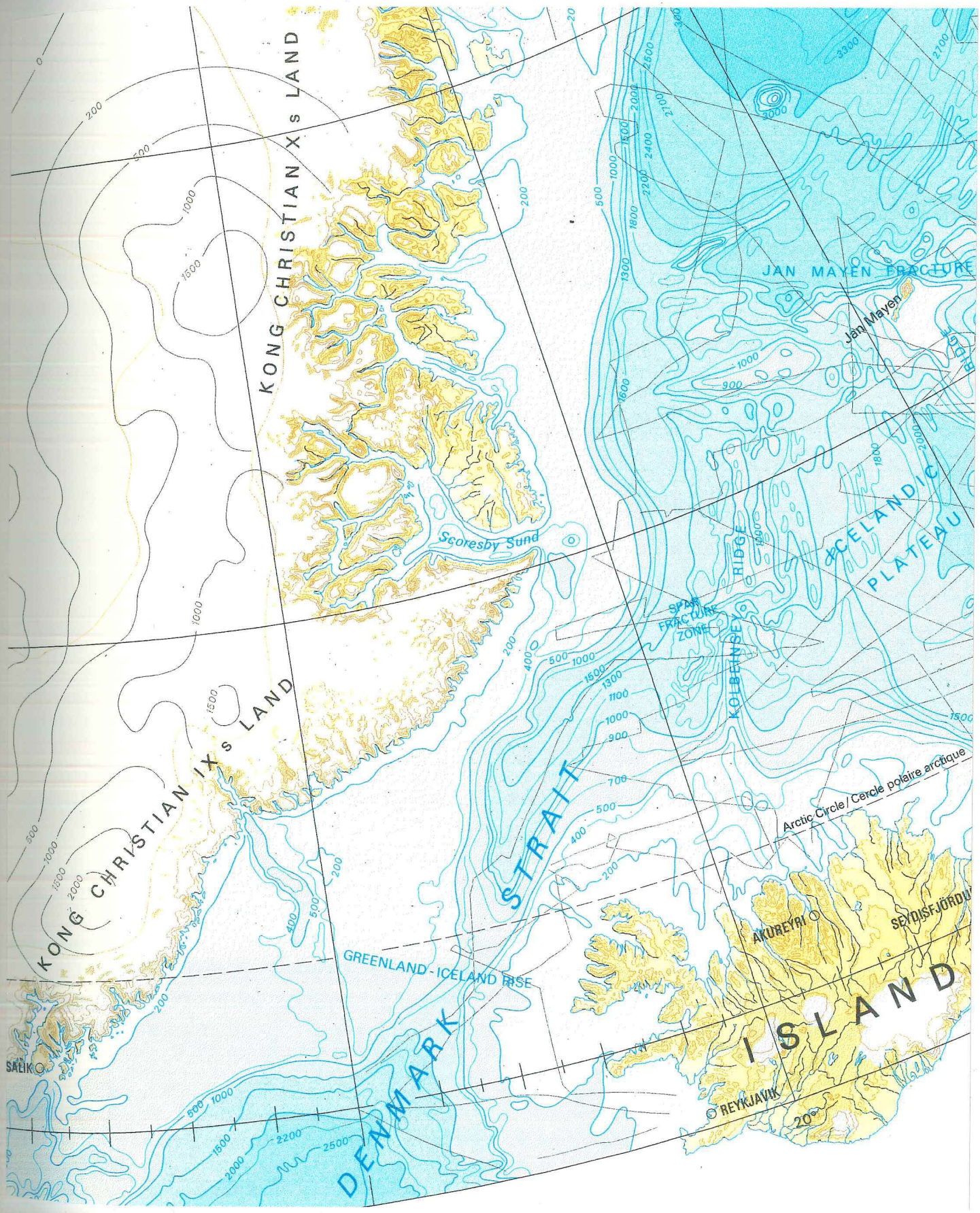

Figure 2.7 Bathymetric map of the shelf adjacent to the study area showing troughs offshore from the major outlet glaciers of the Scoresby Sund and Kangerdlugssuaq Fjords (Section 2.3.2). Scale is 1:6,000,000 at 75°N (GEBCO 1983).

Modern glacimarine depositional processes are still actively transferring material to the shelf via meltwater runoff and iceberg rafting, particularly in the vicinity of the large outlet glaciers such as Kangerdlugssuaq and Daugaard-Jensen Gletscher (Dowdeswell *et al.*, 1991; Marienfeld, 1992; Mienert *et al.*, 1992). In Chapter 6, further details of the marine geology are described, and the identification of turbid meltwater plumes using digital Landsat imagery is investigated.

2.3.3 Late Quaternary Glaciation in East Greenland

The Late Quaternary in East Greenland is characterised by a succession of advances and retreats of the ice sheet. The evidence for this lies in a series of moraines on the presently ice-free coastal regions, as well as the depositional record on the East Greenland shelf. The earliest recorded, and most extensive of these advances, at about 130 ka, is known as the Scoresby Sund glaciation (Funder & Hjort, 1973). This glaciation was succeeded by the Langelandselv interglacial, which has been correlated with oxygen isotope stage 5e (Funder, 1989). This warm interglacial period was followed by a cooler, but still non-glacial period known as the Jameson Land marine episode during which thick marine and deltaic beds were deposited at the mouths of the major fjords.

The ice sheet last advanced to or beyond the present coast during the Flakkerhuk Stade. This period probably dates to the Late Weichselian (ca. 18,000 yr BP). The Flakkerhuk Stade ended with the ice sheet receeding, then readvancing in the valleys and fjords during the Milne Land stade, which is thought to correlate with the European Younger Dryas (Funder & Hjort, 1973). These glaciers, which generally did not reach the outer coast, retreated rapidly from about 11,500 yr BP, eventually retreating behind their present margins by 6-7000 yr BP. Little Ice Age moraines, dated at about 1750-1850 AD, are evident up to ca. 1 km in front of many present day termini, both on land and in the fjords, and mark the maximum extent of the late Holocene readvance (Funder, 1989), since which time the glaciers have retreated to attain their present positions.

2.3.4 Climate History of East Greenland from Ice Cores

It has long been recognised that the Greenland Ice Sheet contains a wealth of palaeoclimatic information recorded in the chemical and physical properties of the ice (Oeschger & Langway, 1989). About 15 intermediate and deep ice cores have been recovered from Greenland to date, including one from the isolated Renland Ice Cap in the interior of Scoresby Sund (Johnsen *et al.*, 1992b). This is thought to record approximately 130,000 years of climate information, which would include the whole of the last glaciation, and possibly the previous (Eemian) interglacial. The oxygen isotope ratio recorded in the ice,

$\delta\ ^{18}O$, has been shown to reflect temperature at the time of precipitation (Robin, 1977), and this has been verified by comparison with air temperature measurements from Iceland and central England (Dansgaard *et al.*, 1985). The Renland $\delta\ ^{18}O$ temperature record (Fig. 2.8), shows the dramatic warming which followed the Younger Dryas at the end of the last glacial, and the series of brief, irregular interglacials which mark the mid to late glacial period (Johnsen *et al.*, 1992a; Johnsen *et al.*, 1992b). Further analysis of the core will eventually reveal a detailed temperature and precipitation record for central East Greenland over the past glacial-interglacial cycle.

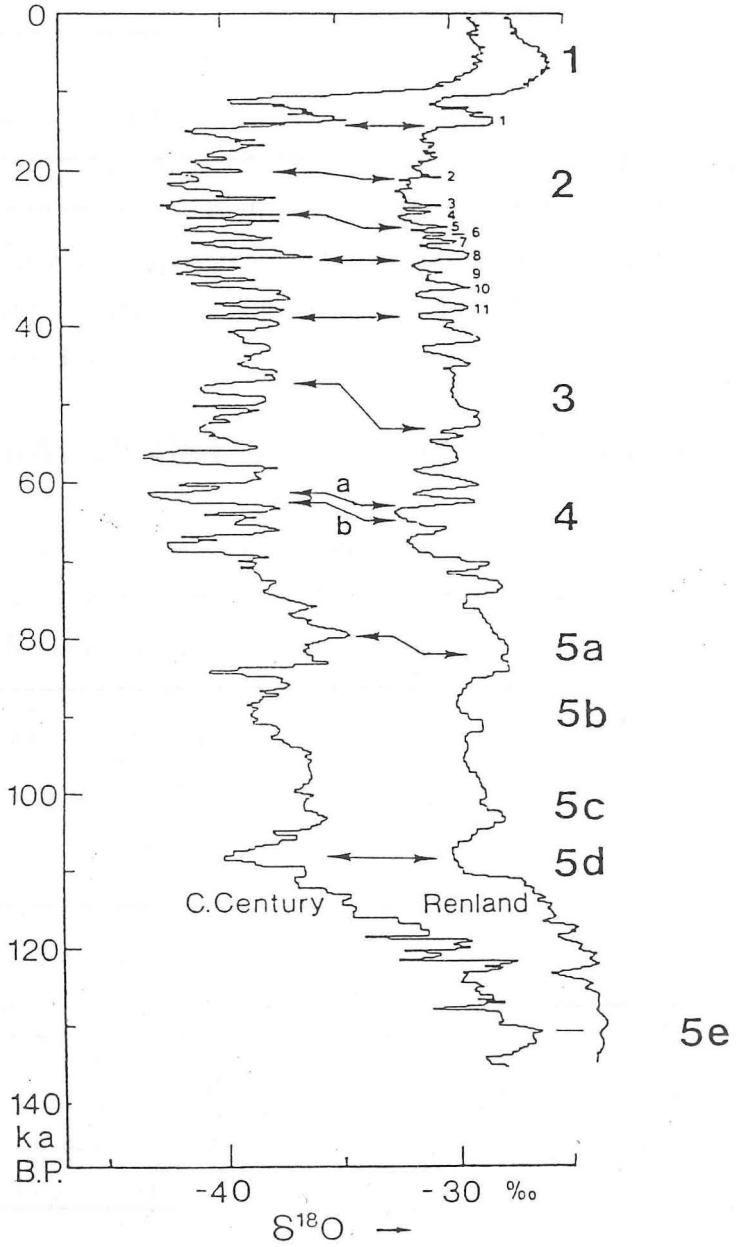

Figure 2.8 $\delta\ ^{18}O$ record for Renland, East Greenland (right) compared to that for Camp Century, North-West Greenland (marked as C on Fig. 2.3). A more negative $\delta\ ^{18}O$ value indicates a lower air temperature at the time of precipitation. Marine oxygen isotope stages are given on the far right, and the smaller figures indicate mid to late glacial interstadials defined by Johnsen *et al.* (1992). The Younger Dryas event is indicated (YD).

Chapter 3

PREPARATION AND PROCESSING OF DIGITAL LANDSAT DATA

In this chapter, the technical details of the acquisition and format of the digital Landsat data from East Greenland are outlined. The haze correction procedures which were applied, and the conversion of the data from digital numbers to reflectance values, are then explained in detail. The conversion to physical values is an important step when attempting to compare scenes recorded for different solar elevations, atmospheric conditions and sensor calibrations (Robinove, 1982).

3.1 CHARACTERISTICS OF LANDSAT DATA

The first of the Landsat series of satellites was launched in July 1972. The latest in the series, Landsat 5, was launched in March 1984 and is equipped with a Multispectral Scanner (MSS) and a Thematic Mapper (TM) sensor. All the digital data used for this thesis were acquired by the Landsat 5 MSS, which records in four radiometric bands (Table 3.1). TM images offer a finer resolution than MSS scenes both spatially (30m) and radiometrically (seven bands), but are significantly more expensive, and represent a shorter time series than MSS data.

Band designation	Wavelength
MSS Band 1 (former Band 4)	0.5 - 0.6µm (Visible, green-blue)
MSS Band 2 (former Band 5)	0.6 - 0.7µm (Visible, red)
MSS Band 3 (former Band 6)	0.7 - 0.8µm (Near infra-red)
MSS Band 4 (former Band 7)	0.8 - 1.1µm (Near infra-red)

Table 3.1 Characteristics of Landsat 5 MSS bands (Note that bands 1 to 4 were formerly referred to as bands 4 to 7 for Landsats 1 to 3).

The area covered by each MSS image is 185 km by 185 km, with a nominal pixel size of 79 m by 56 m. Landsat 5 follows a near-circular sun-synchronous orbit at a height of about 700 km, and images the surface of the earth up to a nominal 81° north and south with a repeat time of 16 days (Massom, 1991). At 80° N/S there is an overlap of 84% between adjacent paths as the successive orbits converge towards the poles (USGS, 1984). The MSS system uses an oscillating scan mirror which sweeps across the direction of flight, sampling brightness values every 56 m across the 185 km swath (Fig. 3.1). Brightness values from each sweep of the scan mirror are recorded by 6 detectors for each band. These brightness values are digitised to 64 levels (6-bit quantisation).

Landsat images are identified using a path and row coordinate system known as the Worldwide Reference System (WRS). Landsats 4 and 5 have different orbital characteristics from Landsats 1 to 3, and hence use a slightly modified reference system known as WRS-2. Under this system, paths are numbered 001 to 233, increasing eastwards whereas rows are numbered 1 to 119 increasing southwards. An image is thus uniquely identified by specifying a path and row number (e.g. 226/011) together with a date (USGS & NOAA, 1982).

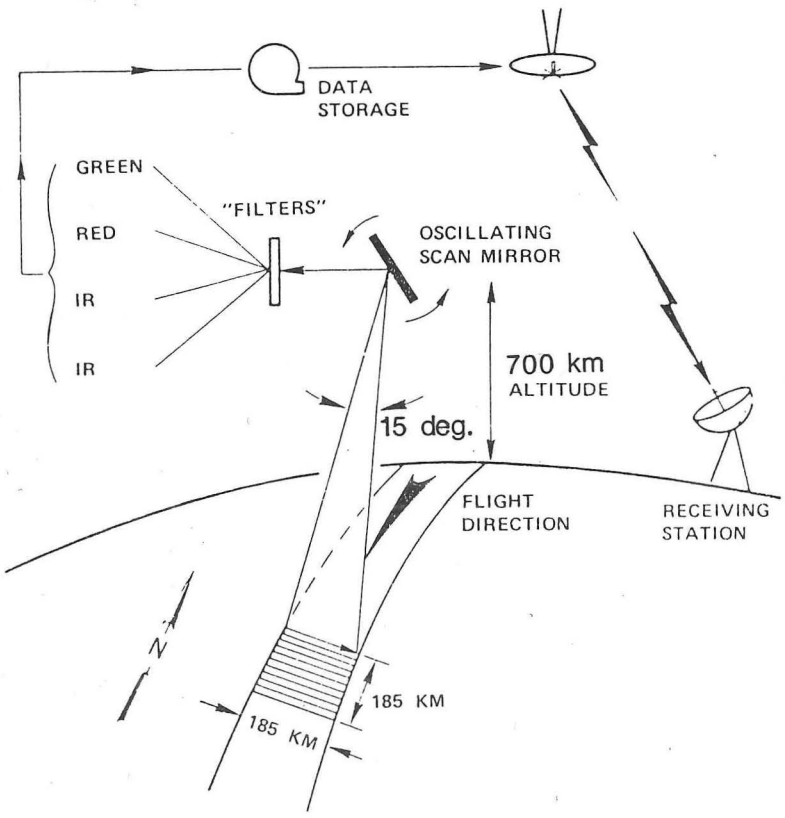

Figure 3.1 Schematic illustration of Landsat multispectral scanner (MSS) system for Landsats 4 and 5 (Cracknell, 1981).

3.2 DATA SELECTION AND ACQUISITION

The sixteen Landsat 5 MSS scenes of East Greenland which were used in this study are listed in Table 3.2, and their locations are illustrated in Fig. 3.2. The images cover a total of about 8° of latitude from 67°N to 75°N. The data were downloaded by the European Space Agency's ground-receiving station at Kiruna in northern Sweden, where the preliminary processing stages of resampling, radiometric calibration and geometric correction were performed. The images were purchased through the National Remote Sensing Centre (NRSC) in Farnborough, Hampshire and were delivered in the form of 9-track computer compatible tapes (CCTs) recorded at 1600 bits per inch. Each band of each image represents approximately 8 megabytes of data.

In order to select the images to be purchased, a computer archive search was instigated at NRSC. The resulting listings indicate the date and cloud cover of the images available for the specified paths and rows. The cloud cover is estimated on a 0-9 scale for each quadrant of an image using a manual procedure. This proved to be somewhat unreliable, particularly over the interior of the ice sheet where it can be difficult to distinguish visually between snow and cloud. In several cases, a black and white 'quick look' print of an image was also purchased in order to confirm the precise spatial coverage and quality of the image before ordering the digital data. These quick-look images are not always of sufficient quality for cloud cover estimation or other detailed interpretation.

For monitoring the snowline elevation as an indicator of mass balance (Chapter 5), it was necessary to obtain scenes recorded close to the end of the balance year when, in the absence of superimposed ice, the transient snowline is equivalent to the equilibrium line (Paterson, 1981, p. 53). Hence, as far as was possible, scenes acquired in August and September were selected. The solar elevation at that time of year is also advantageous, as it is generally low enough to give sufficient contrast to identify subtle surface topographic features (Chapter 4), but high enough to avoid problems with large areas of shade. The additional limitation of requiring virtually cloud-free images made it necessary to utilise data from several different years in order to obtain complete coverage of the area. In the case of scene 229/010, the latest available cloud-free image was from 30 June when the solar elevation was 41.8°. In this image, all sensors, including the band 4 sensor, were saturated (i.e. the brightness level of the surface was beyond the dynamic range of the sensor), which made it difficult to identify flow features from this area (figure 10, Appendix 1). Saturation of bands 1 to 3 is common over ice masses at high solar elevations, but does not usually occur in band 4 (Dowdeswell & McIntyre, 1986).

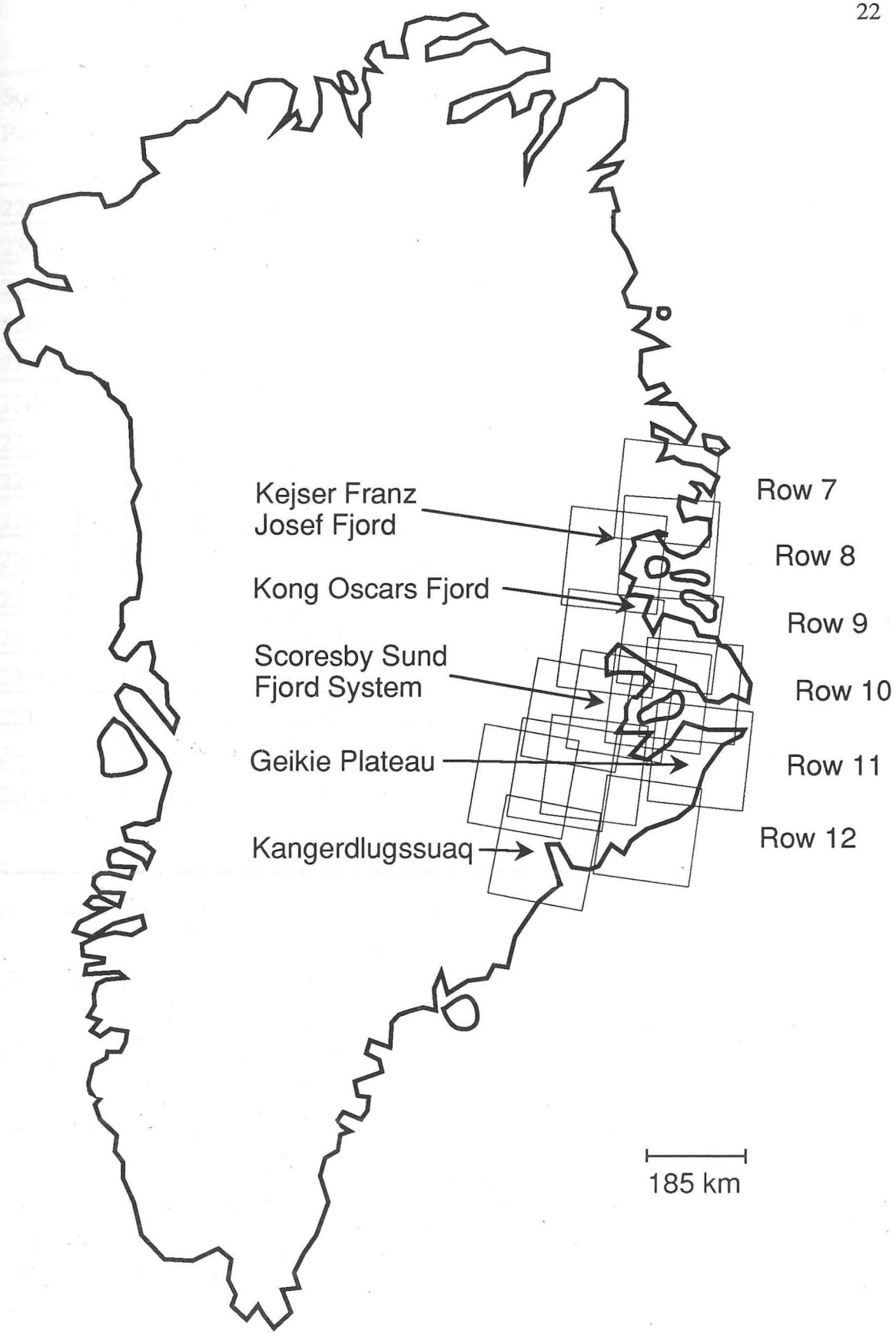

Figure 3.2 Location of Landsat MSS scenes used in this study. Note that scene 231/011 to the north-west of Kangerdlugssuaq was not used as it was substantially obscured by cloud. Scene dates are given in Table 3.2.

Scene Path/Row	Date	Solar Elevation (Deg.)	Area covered by image
227/012	20 Sept. 1988	21.8	Blosseville Kyst
230/012	04 Sept. 1986	27.6	Kangerdlugssuaq glacier and fjord
226/011	08 Sept. 1989	25.1	Geikie Plateau, Kap Brewster
226/011	10 Aug. 1987	35.2	Geikie Plateau, Kap Brewster
229/011	31 Aug. 1987	28.3	Christian IV's Gletscher
230/011	04 Sept. 1986	27.6	Christian IV's Gletscher, interior
227/010	06 Aug. 1989	35.0	Outer Scoresby Sund, Hall Bredning
227/010	20 Sept. 1988	19.4	Outer Scoresby Sund, Hall Bredning
228/010	24 Aug. 1987	29.6	Inner Scoresby Sund, outer fjord system
229/010	30 June 1988	41.8	Inner Scoresby Sund fjord system
230/010	22 Aug. 1987	30.2	Inner fjord system, interior
228/009	24 Aug. 1987	28.4	Kong Oscars Fjord
230/009	22 Aug. 1987	29.1	Nordvestfjord, Kong Oscars Fjord
229/008	15 Aug. 1987	30.2	Kejser Franz Josef Fjord
231/008	29 Aug. 1987	25.5	Kejser Franz Josef Fjord and interior
230/007	22 Aug. 1987	26.8	Wordie Gletscher, Wollaston Forland

Table 3.2 The Landsat MSS scenes acquired for East Greenland (see Fig. 1.2 for place names and Fig. 3.2 for image locations). Scenes are listed from south to north.

3.3 DATA CORRECTION PROCEDURE

Since the intention is to compare physical values from scene to scene, for example when looking for gradients in meltwater turbidity (Chapter 6), it is necessary to correct for the different solar elevation angles at the time of acquisition, and for atmospheric haze, which is usually present to some degree. Although all the images were acquired by the same satellite, the data were also corrected for the individual sensor calibration at the time of acquisition to enable comparison with data from other satellite sensors and ground measurements.

Data are recorded as a digital number (DN) for each pixel, representing a brightness value from 0 to 63. These values are later resampled during the geometric correction to give values from 0 to 255. The aim of the following three-stage correction procedure is to convert the data from raw DNs to the physically meaningful values of within-band reflectance, expressed as a percentage. First, the brightness values are converted to at-satellite radiance

values, then the haze component is estimated, converted to radiance and subtracted, and finally the resulting radiance values are converted to exo-atmospheric reflectances.

3.3.1 Conversion to At-Satellite Radiance Values

At-satellite radiance is a measure of the electromagnetic energy arriving at the sensor and is linearly related to the raw brightness value recorded at the sensor. The brightness values, provided to the user on CCTs as digital numbers (DNs), have been calibrated for drift in detector sensitivity or electronic gain with time. The dynamic range ($Lmax_\lambda$ - $Lmin_\lambda$) is calibrated for each band sensor of each mission before launch and can thus be used to convert DNs to spectral radiances using the following equation (Markham & Barker, 1986):

$$L_\lambda = L\min_\lambda + \left(\frac{L\max_\lambda - L\min_\lambda}{Qcal\,max} \right) \bullet Qcal \qquad \text{(Equation 3.1)}$$

where:

L_λ = Spectral radiance
$Lmin_\lambda$ = Spectral radiance at Qcal = 0
$Lmax_\lambda$ = Spectral radiance at Qcal = Qcal max
Qcal max = Maximum value of calibrated DNs

However, the calibration procedure used by the Swedish Space Corporation in Kiruna uses in-band radiance values rather than spectral radiances, i.e. the radiance over the range of wavelengths represented by each band rather than per µm of the spectrum. The values of Lmin and Lmax used for Landsat 5 data processed at Kiruna during the relevant period are given in Table 3.3 (A. Diament, pers. comm.). The parameters used for data processed in the USA are slightly different and are published in Markham and Barker (1986).

Band	$Lmin_{in\text{-}band}$	$Lmax_{in\text{-}band}$	Qcal max
1	0.0	2.905	255
2	0.0	1.976	255
3	0.0	2.035	255
4	0.0	3.669	255

Table 3.3 Post-calibration in-band radiances (mW cm^{-2} $ster^{-1}$) and maximum digital number values for Landsat 5 MSS data processed in Kiruna during the relevant period.

3.3.2 *Atmospheric Haze Subtraction*

Although cloud is impenetrable at the wavelengths used by the MSS detectors and thus prevents acquisition of useful imagery, water vapour is always present in the atmosphere to some degree and influences all Landsat MSS images. Together with other aerosols, water vapour causes scattering of light into the line of sight of the satellite, thus affecting the apparent brightness of the surface being imaged. This effect is known as atmospheric haze. Scattering is inversely proportional to wavelength and is therefore most significant at shorter wavelengths, i.e. at the blue end of the spectrum (Band 1), and decreases towards the infra-red (Band 4).

The method used to correct for the influence of haze is based on three assumptions:
i) that the effect of haze is additive
ii) that haze can be considered constant over the whole image
iii) that areas of clear, open water should show zero reflectance, and thus any reflectance recorded over these areas can be ascribed to haze.

Each image contained areas of open water, although in the case of image 230/011 only about 40 km^2 of water was present. For each band of each image, at least two areas of ice-free, non-turbid water were selected for analysis. A polygon of 12 by 12 pixels was defined in each area, and a histogram of raw brightness values was plotted for each. A multiple of six pixels was chosen deliberately for these polygons in order to average out the effects of striping due to the variation in sensitivity of the 6 detectors recording each sweep of the scan mirror (USGS, 1984). The average of the peak values of the two (or more) histograms for each image was calculated for each band, and was taken to represent the contribution of haze for that day. The results are expressed as a digital number on a brightness scale of 0 to 255, and are shown in Table 3.4 together with mean and standard deviations for each band.

In four cases, more than one scene was acquired on the same date, so a direct comparison is possible. Scenes 228/009 and 228/010 were both acquired on 24 August 1987 and overlap by about 20%. The haze values, which were assessed independently, show good agreement (Table 3.4). In both scenes, about 20% of the area is open water. Similarly, scenes 227/010 and 227/012 acquired on 20 September 1988 show reasonable agreement despite not having any overlap, and have approximately 25% and 60% open water respectively. However, the haze estimates for the two scenes acquired on 4 September 1986 (230/011 and 230/012) and for the three scenes acquired on 22 August 1987 (230/007, 230/009 and 230/010) show a greater disparity (Table 3.4).

Of the two scenes from 4 September, scene number 230/011 has a total open water area of only about 40 km^2, or 0.1% of the whole scene (Fig. 6, Appendix 1), which is immediately adjacent to a glacier terminus. As the haze estimates for this scene are anomalously high (Table 3.4), which would be consistent with the presence of turbid water or sub-pixel scale ice, it was decided to apply instead the haze estimates from scene 230/012, which is immediately adjacent to the south and has an open water area of about 17%.

Path/row	Date	Band 1	Band 2	Band 3	Band 4
226/011	8 Sept 1989	25	15	11	5
226/011	10 Aug 1987	27	12	11	5
227/010	6 Aug 1989	32	15	10	5
227/010	20 Sept 1988	24	10	10	6
227/012	20 Sept 1988	23	14	10	8
228/009	24 Aug 1987	23	10	9	5
228/010	24 Aug 1987	23	11	10	6
229/008	15 Aug 1987	27	13	11	6
229/010	30 June 1988	32	15	12	7
229/011	31 Aug 1987	24	13	11	7
230/007	22 Aug 1987	28	12	10	7
230/009	22 Aug 1987	28	11	10	5
230/010	22 Aug 1987	30	18	14	5
230/011	4 Sept 1986	30	20	14	9
230/012	4 Sept 1986	24	10	10	4
231/008	29 Aug 1987	25	10	9	7
Mean haze values		26.6	13.1	10.7	6.1
Standard deviation		*3.1*	*2.9*	*1.4*	*1.3*
Revised mean haze values		26.2	12.4	10.5	5.7
Revised standard deviation		*3.0*	*2.3*	*1.2*	*1.1*

Table 3.4 Atmospheric haze values for each band of each scene as estimated by open water analysis method (expressed as DNs on a scale of 0 to 255).

All three scenes from 22 August are reasonably consistent in bands 1 and 4. These are the most relevant bands for identifying sediment plumes, and snow and ice surface features respectively (the latter since band 4 is the least likely to saturate (Dowdeswell & McIntyre, 1986)). For bands 2 and 3, scene 230/010 gave values higher than those from 230/009 and 230/007 but it was decided that, since the sample areas for scene 230/010 were approxi-

mately 250 km south of those for 230/009, this may represent a genuine gradient in haze conditions, and so the estimates were not adjusted.

The mean and standard deviations were recalculated for the revised estimates, and are also presented in Table 3.4. Band 1 still has a relatively high standard deviation, which is largely attributable to the high band 1 haze estimates from scenes 229/010 (30 June 1988) and 227/010 (6 August 1989). This could be explained by the fact that, of the sixteen scenes, these two are from earliest in the year. In both cases, significant amounts of pack ice are still present in Scoresby Sund fjord (Figs. 10 and 7, Appendix A), so sub-pixel scale ice may have caused an overestimation of the haze. Band 1 also has the highest absolute DN values, and the proportional deviation is no higher than for the other bands.

It can be concluded that, given sufficient clear open water areas, this method of haze correction appears to be consistent. Where the results deviate from the expected values, this can be explained by the presence of turbid water or sub-pixel scale ice, and values from adjacent, simultaneously-acquired images can be substituted. An assessment of the validity of the correction procedure is made in Section 3.3.4 by comparing overlapping scenes acquired two days apart.

The haze values obtained by this method were converted to radiance by the procedure described in Equation 3.1, and then subtracted from the total radiance. The resulting haze-corrected radiance values were transformed to reflectance as described in the following section.

3.3.3 Conversion to Within-Band Reflectance Values

The corrected radiance values are independent of sensor parameters and atmospheric conditions, but are still dependent on the solar radiation incident on the surface at the time of imaging (Robinove, 1982). This varies with the earth-sun distance and the angle of solar elevation, which both in turn depend on the time of the year. Solar elevation also varies with latitude. The aim of the conversion to reflectance is to remove these dependencies, and thus make the data directly comparable in a quantitative way. Note that the apparent reflectance is still dependent on the slope of the surface and the orientation relative to the sun, but no attempt was made to correct for these effects since they serve to reveal topographic features.

The transformed values are expressed as effective at-satellite reflectance for each band, or within-band top of the atmosphere albedo, since the albedo of the atmosphere cannot be separated from the albedo of the surface. The combined surface and atmospheric reflectance of the earth is given as:-

$$\rho_p = \frac{\pi L_{in-band} d^2}{Esun_{in-band} \cos\theta_s} \qquad \text{(Equation 3.2)}$$

where:

ρ_p	=	effective at-satellite in-band planetary reflectance, expressed in %
$L_{in\text{-}band}$	=	in-band radiance at sensor (mW cm^{-2} $ster^{-1}$) calculated using eqn. 3.1
d	=	earth-sun distance in astronomical units (Duffett-Smith, 1990)
$Esun_{in\text{-}band}$	=	solar exo-atmospheric irradiance (mW cm^{-2}) (Markham & Barker, 1986)
θ_s	=	solar zenith angle (specified in tape header record)

It is these dimensionless reflectance values which are used in all subsequent analyses.

3.3.4 Verification of Correction and Conversion Procedure

To assess the effectiveness of the correction and conversion procedures, a comparison was made of data from two overlapping scenes recorded two days apart. The two scenes, which were 230/010 acquired on 22 August 1987 and 228/010 acquired on 24 August 1987, had an overlapping area of about 40% including Fønfjord and most of Renland, in the inner Scoresby Sund fjord system (see Figs. 9 and 11, Appendix 1). Four polygons of 18 by 18 pixels (equivalent to 1.4 km^2) were defined within the overlapping areas, each representing a different surface terrain type; bare ice, snow, rock and turbid lake water (Fig. 3.3). These areas were selected such that they could be visually located on both scenes, since the two coordinate systems are not co-referenced. The ice polygon is located on a small ice tongue in the lower part of Rolige Gletscher, while the lake is a small ice-dammed lake near the terminus of Eielsen Gletscher (Fig. 3.3). The rock and snow areas were less clearly delineated, so a small uncertainty in their positioning exists. The identification of the terrain types, in the case of the lake and rock areas, was confirmed by reference to the appropriate Dansk Kort og Matrikelstyrelsen 1:250,000 map sheets. For the snow and ice polygons, care was taken to select areas at high and low elevations on the respective glaciers in order to avoid the transition zone around the snowline. Histograms were plotted for each terrain type for each band, and the results compared for the two scenes (Fig. 3.4).

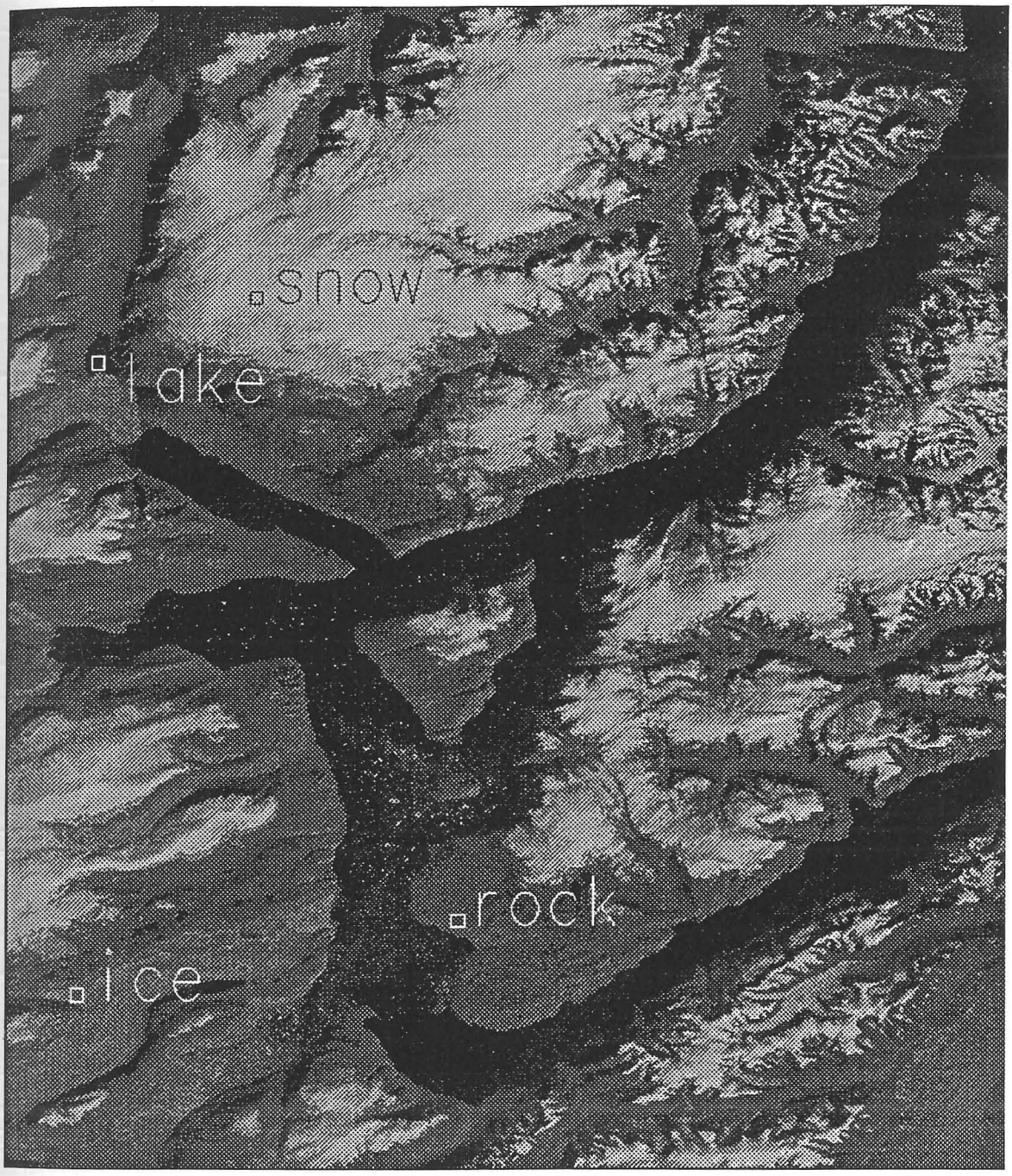

Figure 3.3 Test areas used in verification of haze correction procedure. Each polygon is 18 by 18 pixels, which is equivalent to 1.4 km in the x-direction and 1.0 km in the y-direction due to the rectangular pixels (Section 3.1). Area shown is part of image 228/010 (acquired 24 August 1987) and is approximately 80 km wide by 100 km.

It can be seen from Fig. 3.4 that the agreement between the two scenes is good, with the discrepancy generally being less than 2% and in no case more than 6%. The histograms exhibiting most difference between scenes are those for snow in band 1 (3%) and band 4 (6%). However, it appears that band 1 is saturated in both scenes, as all 324 pixels from each scene have the same reflectance values (Fig. 3.4c), so this discrepancy is unlikely to be physically significant. A possible explanation for the differing values in band 4 is that some change in the snow surface has occurred over the intervening two days, such as an increase in moisture content, or metamorphosis of the snow surface character due to the normal ageing processes whereby grain size gradually increases (O'Brien & Munis, 1975). The spectral albedo of snow at these wavelengths has been demonstrated to be more sensitive to both grain size (Wiscombe & Warren, 1980) and solar zenith angle (Yamanouchi, 1983) than at shorter wavelengths.

Snow is generally seen to have a high degree of spatial variability in band 4, so a small error in locating the sampling box on the two scenes could also cause the observed shift in the histograms. It should be emphasised that a difference of 6% represents only 4 DNs on the original scale of 0 to 63, so a rounding error in the resampling process, or a slight misjudgement of the haze contribution could also contribute to the mismatch. On this basis, it was decided to use band 3 data for the monitoring of snowline elevations, where scene-to-scene consistency in absolute reflectance values is important (Chapter 5).

In conclusion, it appears that the haze correction procedure and the conversion to reflectance values are both consistent and valid. The resulting corrected reflectance values show a high degree of scene-to-scene continuity, as illustrated by the frontispiece mosaic, although further comparisons could be made of overlapping scenes and simultaneously acquired scenes to confirm this conclusion. The corrected reflectance values were subsequently used in the analyses of drainage basin areas, snowline altitudes and meltwater turbidity for the East Greenland coastal region, as described in the following three chapters.

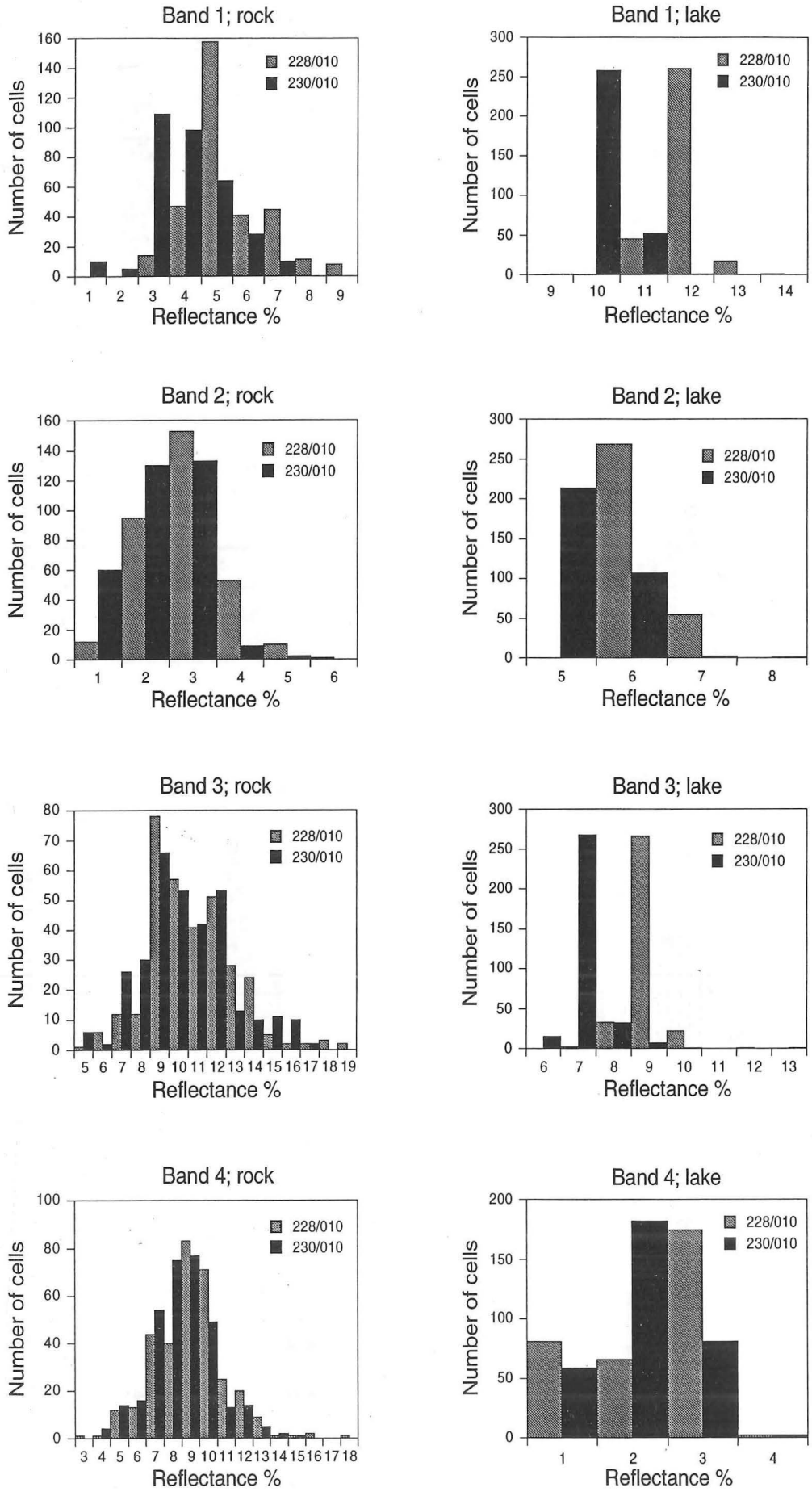

Figure 3.4 a,b Comparison of reflectance histograms for the four MSS bands for bare rock (left column) and turbid lakewater (right column) polygons for scenes 228/010 and 230/010.

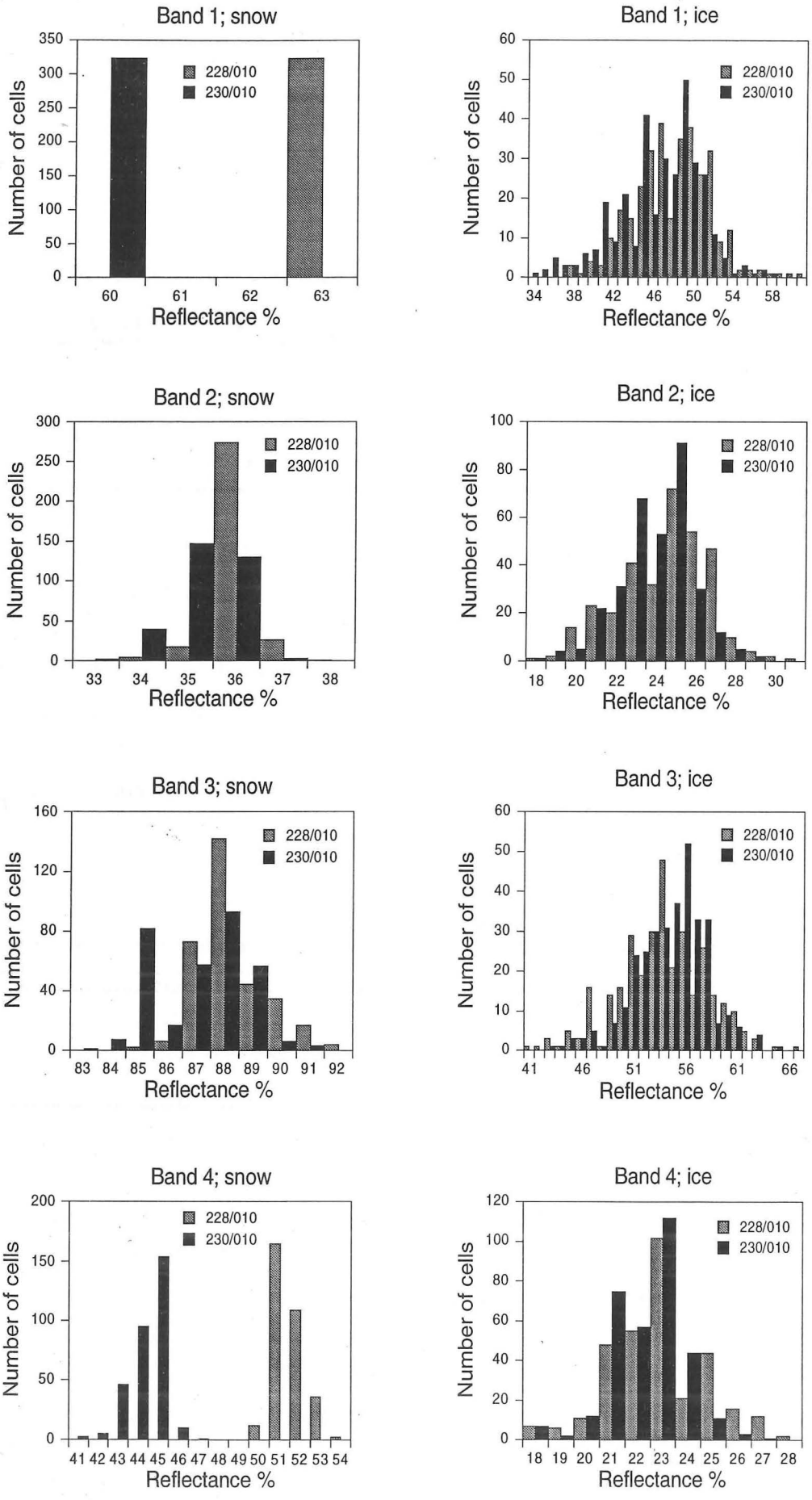

Figure 3.4 c,d Comparison of reflectance histograms for the four MSS bands for snow (left column) and bare glacier ice (right column) polygons for scenes 228/010 and 230/010.

Chapter 4

Drainage Basin Characteristics of Tidewater Glaciers in East Greenland

The mass balance of the Greenland Ice Sheet as a whole is, at present, only poorly determined (Reeh, 1985), and much of the uncertainty in the balance estimates is due to a lack of data from the East Greenland sector. A first step towards determining the mass balance of the glaciers of East Greenland is to define the limits of the individual drainage basins, as the balance of each basin can then be considered separately. The glaciers of West Greenland up to 71°N have recently been catalogued by Grønlands Geologiske Undersøgelse (Weidick *et al.*, 1992), but the glaciers of East Greenland have not been studied comprehensively to date.

The mass balance of a drainage basin is the difference between the mass accumulated within the basin area from precipitation, and the mass lost by basal and surface melting plus, in the case of tidewater glaciers, iceberg production (Section 2.1.3). If precipitation is constant over a region, then it is clearly those glaciers with the largest drainage basins that have the largest mass to transport to the ablation area if a balance is to be maintained. In practice, precipitation and temperature vary with both latitude and degree of continentality, so the balance velocity is not dependent on basin area alone.

For the tidewater glaciers of Greenland, mass loss occurs largely by iceberg calving rather than melting (Echelmeyer *et al.*, 1992). The elevation below which surface melting and runoff occurs (the snowline), tends to be low due to the sub-polar to polar climate, and thus the snowline occurs near the terminus of a glacier where flow is often constrained by local topography. Iceberg production is also influenced by the width of the terminus, as the valley sides exert a proportionally greater frictional force on a narrow glacier, thus acting to restrict the flow. The ratio of the drainage basin area to the terminus width can therefore give an indication of the dynamic regime or mass balance of a glacier, as the basin area determines the mass input to the system, and the terminus width influences the mass output and velocity. A glacier with a high basin area to terminus width ratio is likely to be either fast flowing or gaining mass.

4.1 METHODOLOGY

4.1.1 Determination of Drainage Basin Areas

A total of 74 glacier drainage basins terminating in tidewater within the study area were delineated using digital Landsat imagery, in conjunction with the Kort og Matrikelstyrelsen (KMS) and the US Army Mapping Service (AMS) 1:250,000 scale topographical maps. Of these glaciers, which are identified by arrows in Fig. 4.1, 73 were on the mainland and one, designated no. 74, was on the island of Milne Land. The study area (which stretches from about 68°N to 75°N, Fig. 1.1) was divided into four regions; Kangerdlugssuaq Region, Blosseville Kyst Region, Scoresby Sund Region and the Northern fjords region, as shown in Fig. 4.1.

Band 4 digital data were used for delineating the drainage basins, as this sensor seldom saturates, even over new snow (Section 3.2). The relatively low sun angles at the time of acquisition (generally between 20° and 30°, Table 3.2) gave good contrast in regions of gentle surface gradients, such as the summit of an ice dome, and enhanced the subtle surface flow features at all elevations on the glaciers (Fig. 4.2).

The drainage basin areas for each glacier within a scene were determined by tracing the ice divides back from the terminus towards the interior. In the vicinity of the coast, the flow pattern is usually determined by the mountainous local topography, and hence the watersheds often lie along the crests of mountain chains (Fig. 4.2). In a number of cases, snowfields lying on opposite sides of a mountain chain were found to feed glaciers which eventually drained through the same terminus (e.g. Bredegletscher, glacier no. 48 in Table 4.3, Fig. 4.2), but even these complex flow patterns could usually be inferred by close examination of surface flow features on the satellite imagery.

Further inland, only occasional mountains penetrate the ice sheet as nunataks and, in this region, medial moraines originating at these nunataks were used in conjunction with flowlines to infer flow patterns (Fig. 4.2). For the Geikie Plateau area, sufficient nunataks are present over the region to be able to trace the drainage patterns with a high degree of accuracy, except for in the vicinity of the main ice divide. Here, the boundary between drainage basins was easily identified by a change in reflectance values, which is interpreted as representing a break of slope at the summit ridge (Dowdeswell & McIntyre, 1987), and hence the ice divide (Martin & Sanderson, 1980). In several cases, a saddle point could be identified where linear surface features, interpreted to be flowlines (Crabtree & Doake, 1980), diverge at a pass (Fig. 4.2). This interpretation was sometimes supported by elevation contours from the KMS and AMS maps, although in many areas, elevation data on the maps are inadequate for determining flow directions.

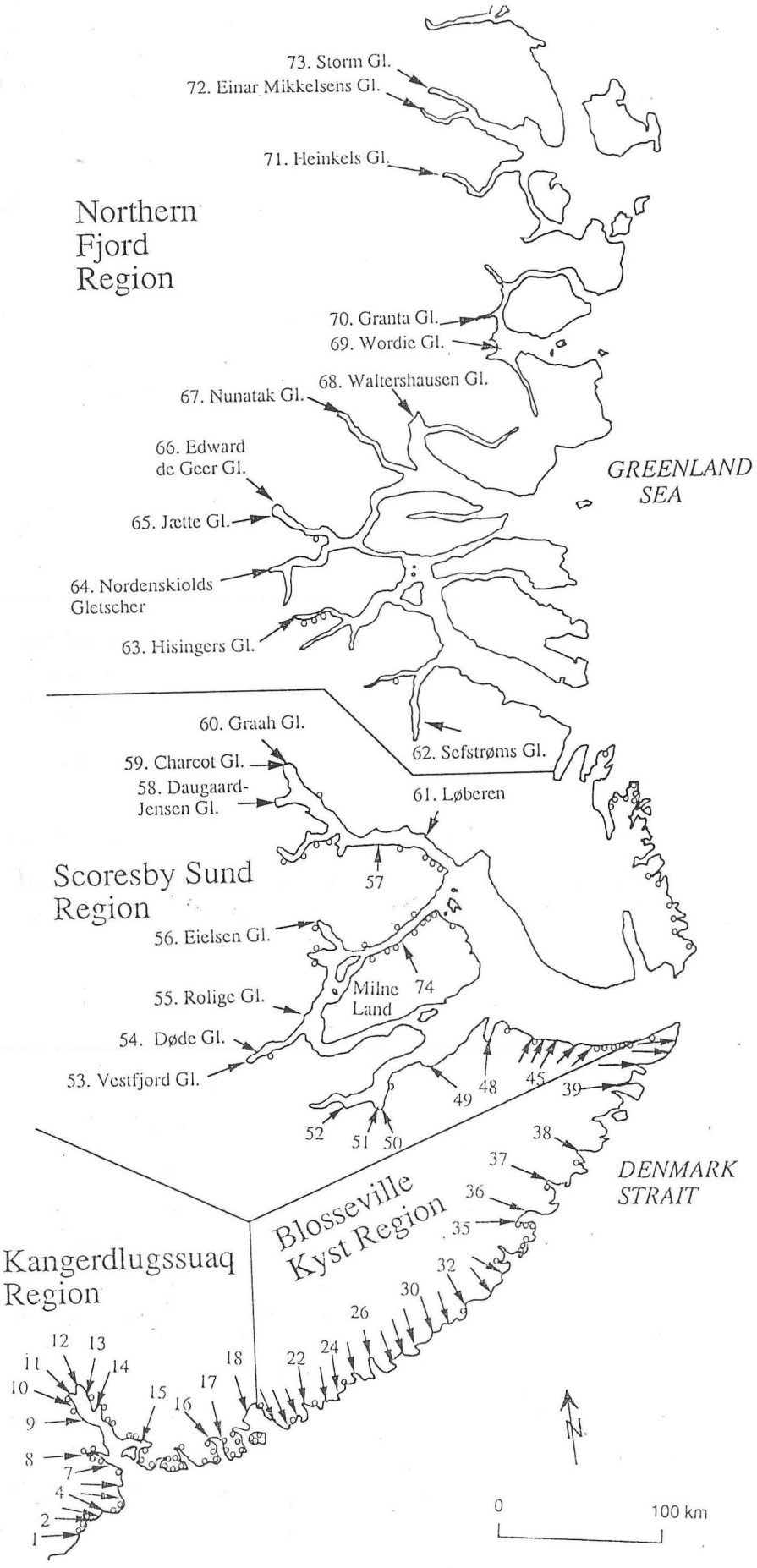

Figure 4.1 Map showing location of all termini ending in tidewater within the study region. Arrows and numbers refer to glaciers listed in Tables 4.1 to 4.4, while dots indicate terminus position of basins less than about 20 km^2 (Section 4.1.1).

For the larger drainage basins reaching further inland to the main ice sheet, or for the isolated ice caps, such as Renland (Fig. 4.3), it became necessary to use the subtle topographic features revealed by the relatively low solar elevation angles in order to delineate the drainage basins. The KMS and AMS maps were also consulted, but the elevation data in these areas were often absent, contradictory, or insufficiently detailed to be of assistance.

Basin areas are determined by using the image processing software to calculate the area of digitized polygons. Where a basin spanned more than one image, the total area was determined by summing the area of the basin for each image, then subtracting the overlapping areas.

Topographic details were, in some cases, obscured by small patches of cloud, which were easily distinguished from the snow surface by their characteristic texture. There is sufficient overlap between the images (Fig. 3.2) that this was not a significant problem except for scene 230/010 (Fig. 11, Appendix 1). In this scene, thin cloud partly obscured the divides between Vestfjord Gletscher, Døde Bræ and Rolige Bræ (nos. 53, 54 and 55, Table 4.3), which must therefore be considered less reliable, although the error would be a few kilometers at most. Scene 231/011, covering the northern part of the Kangerdlugssuaq drainage basin, could not be used at all, as cloud obscured much of the image, which had been mistakenly classified at the Kiruna ground station as almost cloud-free.

Many of the smaller glaciers could not be delineated accurately due to problems in interpreting their boundaries. Depending on their orientation relative to the sun, much of the area of these glaciers could be obscured by shadowing due to the steep local topography. In other cases, a snowfall shortly before the image was acquired had obscured the boundary between the glacier surface and the surrounding terrain. Similarly, if large amounts of morainal debris are present on a glacier, it is difficult to differentiate the glacier surface from the adjoining rocky terrain. In practice, these limitations meant that glacier basins smaller than about 20 km^2 could not usually be determined accurately unless the orientation was favourable. Sfinx Gletscher (no. 42, Table 4.2) faces south-west, and could be delineated despite having an area of only 19 km^2. A total of 105 smaller tidewater glaciers were identified from the KMS or AMS maps, and are marked as dots on Fig. 4.1.

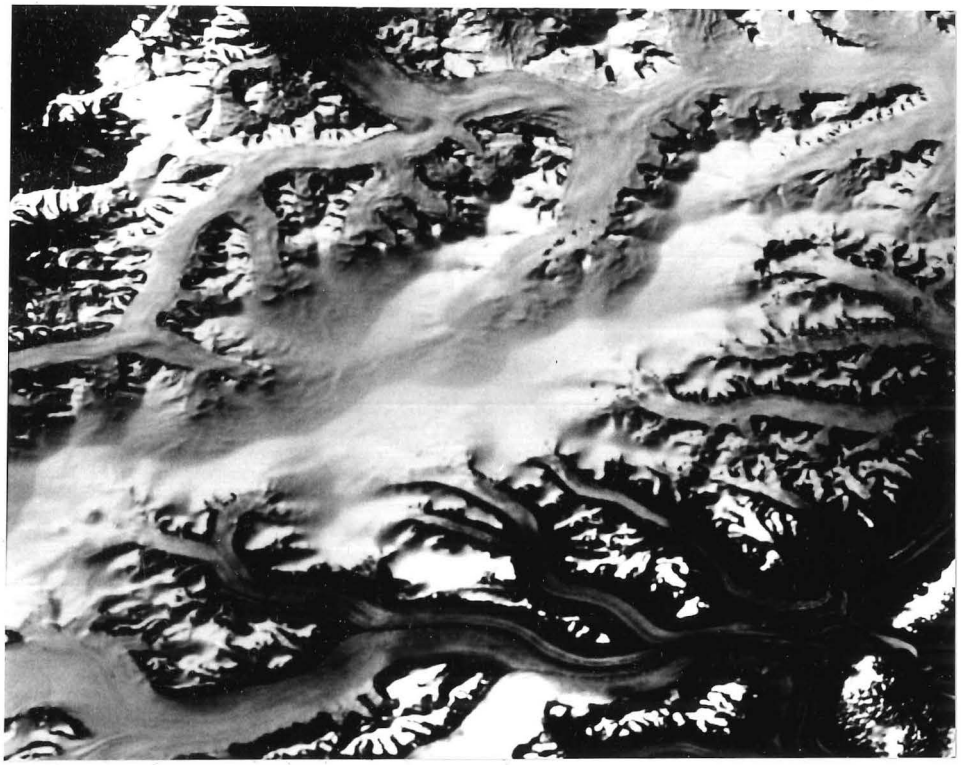

Figure 4.2 Screen photograph of a portion of scene 226/011, band 4 of 8 Sept 1989 (Fig. 3, Appendix 1), showing drainage basin divides (Section 4.1.1). The terminus of Bredegletscher (no.48) can be seen at top left, and the medial moraines on the branches of glacier no. 38 (unnamed) can be seen at the bottom right of the photograph. The area shown is about 90 km wide. Note that all screen images are distorted in the ratio 56:79 due to the rectangular pixel shape (Section 3.1).

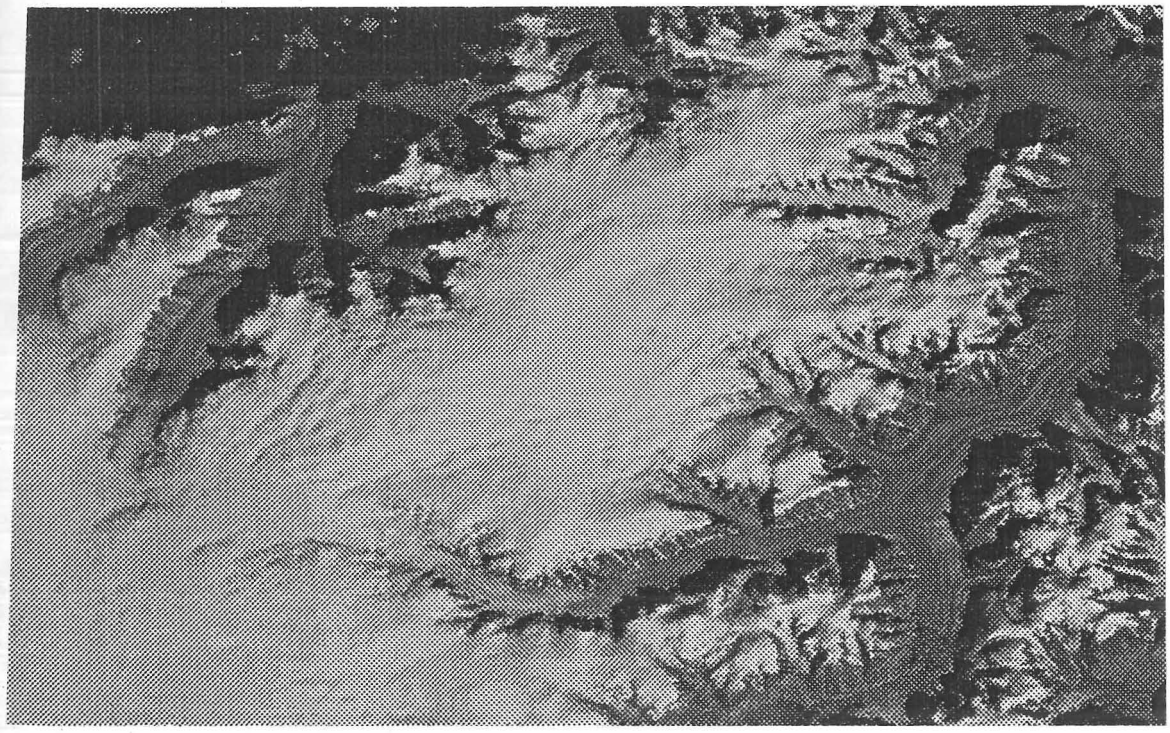

Figure 4.3 Subtle topography of the Renland Ice Cap is revealed by apparent shadowing. The image is part of scene 228/010, band 4 (Fig. 9, Appendix 1) acquired on 24 Aug 1987, with a solar elevation angle of 30°. Area shown is about 50 km wide.

4.1.2 *Determination of Terminus Widths*

The terminus width of each of the 74 drainage basins was determined using the digital satellite imagery where possible, or from the maps otherwise. In many cases it was not possible to determine the terminus width unambiguously from the MSS imagery, due to mountain shadows obscuring part or all of the terminus, or due the presence of fast ice with a similar reflectivity to glacier ice, making identification of the terminus uncertain. In these cases, an estimate of the terminus width was made using the 1:250,000 KMS and ICAO maps.

The width of the terminus was defined to be the perpendicular distance across the terminus at the point where it is in contact with the water, as opposed to the length of the ice-water contact, or the limiting width of the outlet glacier. For a piedmont type glacier (such as Sefstrøms/Gully Gletscher, no.62 in Table 4.4) the ice-water interface is larger than the perpendicular width given.

For the widths determined from satellite imagery, the effect of the rectangular pixel shape must be taken into account. Although each pixel represents 79 m by 56 m on the ground (Section 3.1), it is assumed by the image processing software to be a square of 1 unit by 1 unit. Therefore, the digitized widths were transformed to real widths by simple trigonometry using the following formula:

$$w = \sqrt{(79 \cdot d \cdot \sin\theta)^2 + (56 \cdot d \cdot \cos\theta)^2} \qquad \text{(Equation 4.1)}$$

where:

w = width in metres
d = width in pixel units
θ = angle from horizontal

4.1.3 *Estimation of Errors*

For the determination of the basin areas, the main sources of error are uncertainties in the interpretation of basin divides and digitizing inaccuracies. The digitizing errors are constant over the region and usually represent a small proportion of the basin area. Repeated digitization of the same basin gave an variation of approximately 2 - 5% for basins where the divides were easily determined. The interpretation errors depend on several factors; the nature of the basin divide (subtle ice dome topography or complex flow patterns are more difficult to interpret), the solar elevation angle (either excessive shadowing in mountainous regions or insufficient shadowing in regions of gentle gradients), the presence of clouds,

and the degree to which surface flow features are evident. These errors are therefore different for each drainage basin, and have not been determined individually.

For the terminus widths, uncertainties are introduced by ambiguity in the location of the terminus due to the presence of fast ice, shadows obscuring the terminus, and new snow or surface moraine blurring the boundaries of the glacier. The digitized terminus widths could usually be determined with an accuracy of 1 or 2 pixels at either end of the glacier front, giving a maximum uncertainty of about 300 m. For those widths obtained from the maps, the error in measurement is approximately 1 mm, which represents 250 m on the ground. All values are therefore given to the nearest 250 m.

4.2 PRESENTATION OF RESULTS

The drainage basin areas and terminus widths are presented in the following section in the form of tables of results for each region, and diagrams of basin extent within the study area. The size-frequency distribution of each parameter is then examined.

4.2.1 Drainage Basin Areas and Terminus Widths

The drainage basins of tidewater glaciers in the study area are presented in Figures 4.4 and 4.5, and the detailed results for each basin are given in Tables 4.1 to 4.4. The reference numbers correspond to those shown on Figure 4.1, and are listed from south to north along the mainland coast, with the exception of no. 74 on Milne Land (Fig. 4.1). Glacier names from the KMS maps are given, where these are available and unambiguous, or alternatively the name of a nearby topographic feature is given in brackets. The geographic coordinates refer to the location of the terminus as determined from the KMS or AMS maps. The precision to which the area figures are given is not intended to reflect the accuracy of the results; a discussion of errors and uncertainties is given in Section 4.1.3.

Several of the larger drainage basins extended beyond the area covered by the images (Fig. 3.2) and, where possible, an estimate for the area of these basins was obtained from the literature. These estimates are given in brackets in Tables 4.1 to 4.4.

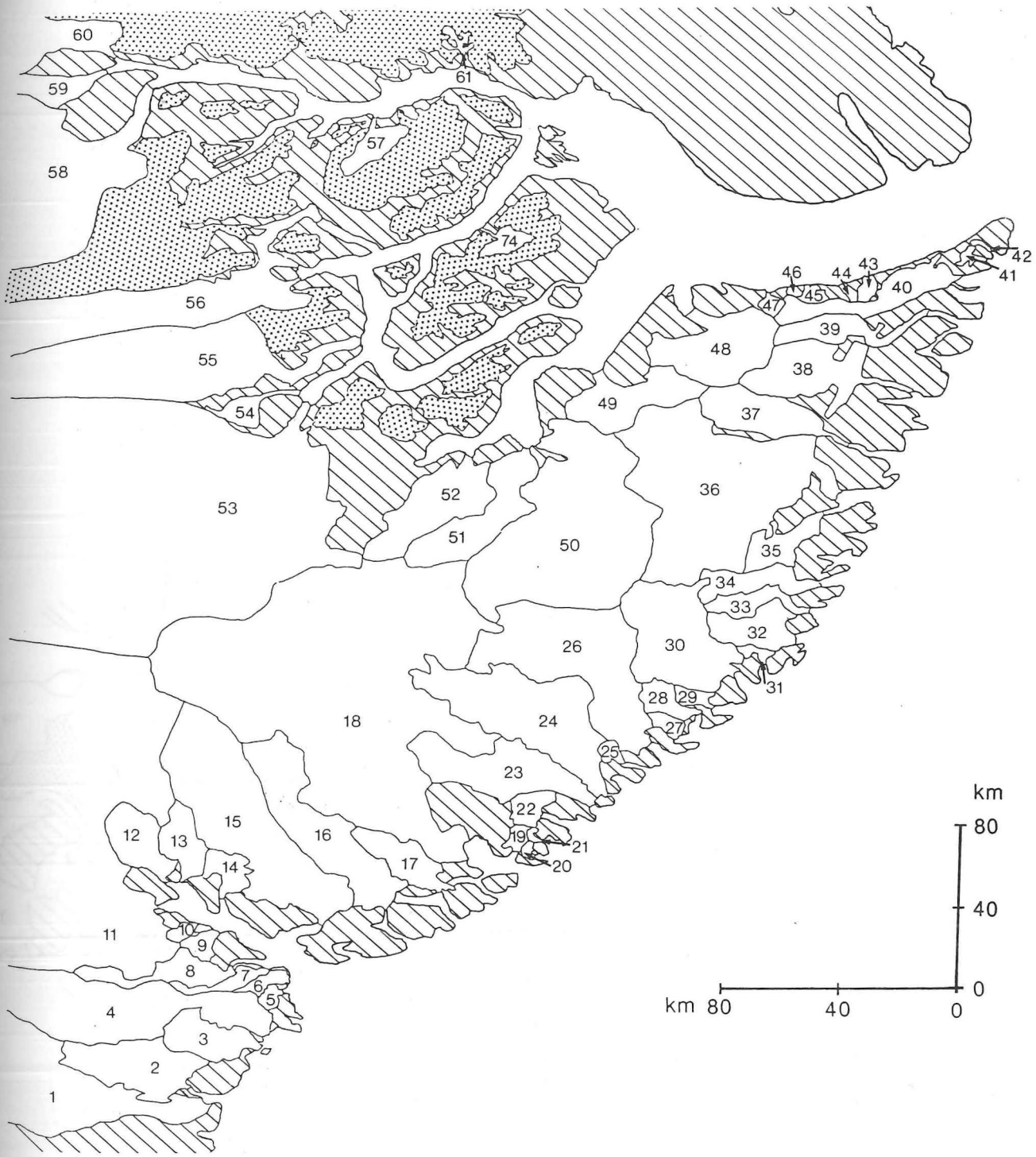

Figure 4.4 Map showing drainage basins for glaciers terminating in tidewater in the Kangerdlugssuaq, Blosseville Kyst and Scoresby Sund regions. Numbers refer to Tables 4.1 to 4.3, where the surface area of each basin is given. Note that vertical and horizontal scales are distorted in the ratio 56 to 79 due to the rectangular pixels (Section 3.1). Drainage basins of tidewater glaciers are shown in white and other snow and ice covered areas are shaded with dots. Diagonally hatched areas indicate bare rock.

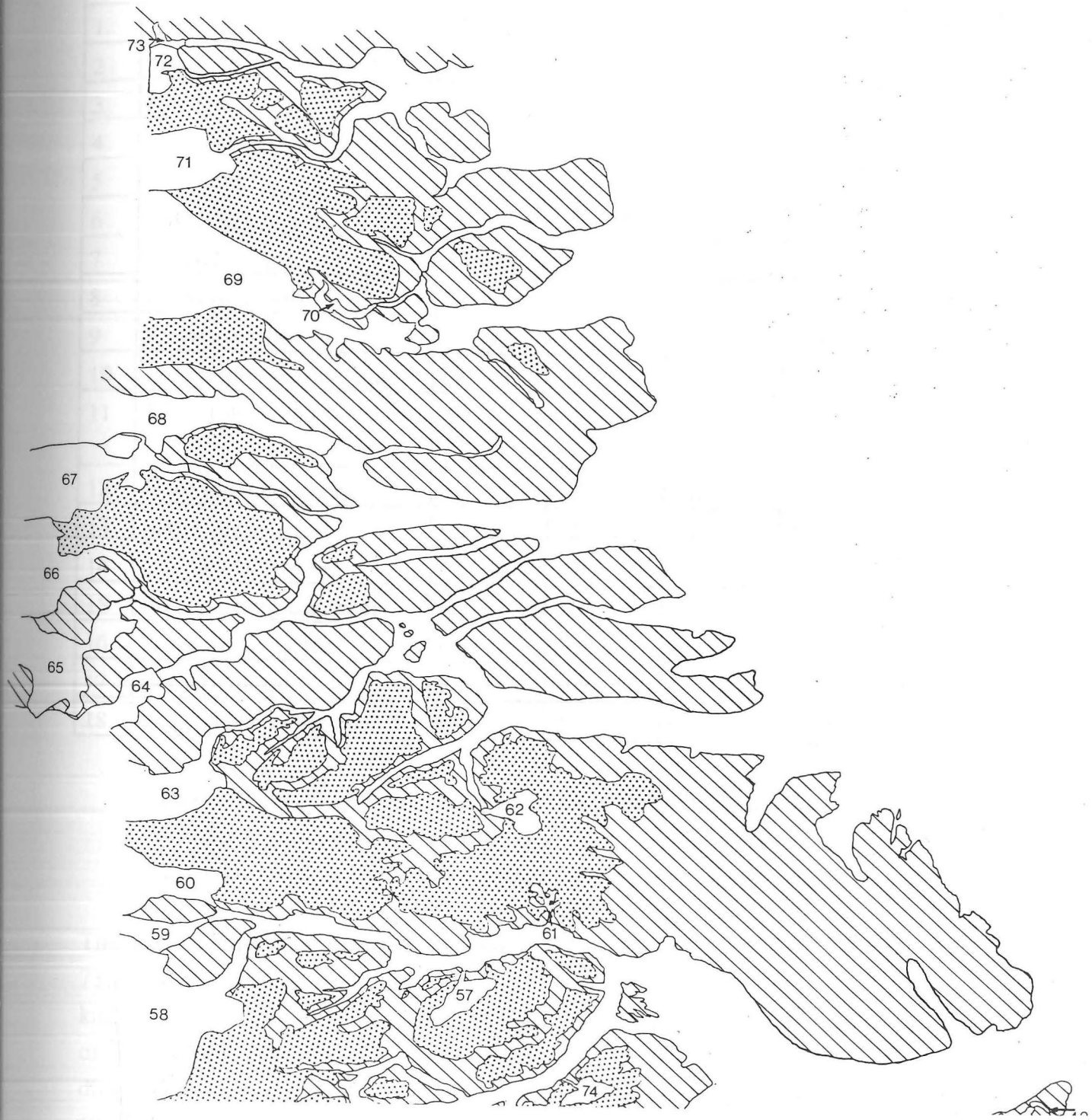

Figure 4.5 As for Figure 4.4 showing drainage basins for the northern fjord region (Table 4.4). Note that many of the glaciers in this region extend beyond the study area.

No.	Name of glacier (or adjacent fjord, island, headland etc.)	Terminus latitude (N)	Terminus longitude (W)	Drainage basin area (km^2)	Terminus width (km)	Area to width ratio
1	(no name)	67° 40'	33° 10'	>3250	4.5	>722
2	Nordre & søndre parallel gl.	67° 41'	33° 10'	938	3.75	250
3	(Fladø)	67° 50'	32° 34'	513	2.75	186
4	Hutchinson Gletscher	67° 53'	32° 26'	>2642	7.5	>352
5	(no name)	68° 02'	32° 10'	69	1.75	39
6	(no name)	68° 06'	32° 03'	106	5.5	19
7	(Kvadderbugt)	68° 09'	32° 13'	162	2.75	59
8	(Amdrup Fjord)	68° 12'	32° 30'	448	2.0	224
9	Kælvegletscher	68° 23'	32° 30'	123	2.5	49
10	(Kangerdlugssuaqs Tinde)	68° 26'	32° 35'	69	1.5	46
11	Kangerdlugssuaq Gletscher	68° 33'	32° 44'	>>11820 (≈50000)	5.0	≈10000
12	Nordfjord Gletscher	68° 38'	32° 22'	510	2.0	255
13	Styrte Gletscher	68° 38'	32° 30'	391	1.5	261
14	Courtauld Gletscher	68° 30'	32° 14'	245	1.75	140
15	Frederiksborg Gletscher	68° 16'	31° 34'	2396	2.5	958
16	Sorgenfri Gletscher	68° 17'	30° 49'	1410	5.5	256
17	(Ryberg Fjord)	68° 15'	30° 28'	218	3.0	73
18	Christian IV's Gletscher	68° 23'	30° 00'	9517	15.0	634

Table 4.1 Drainage basin areas and terminus widths for tidewater glaciers in the Kangerdlugssuaq region (Figs. 4.1 and 4.4). Basin area estimates derived from maps in Bindschadler *et al.* (1989) are given in brackets.

The Kangerdlugssuaq fjord area (Table 4.1 and Fig. 4.4) drains a total of about 73,000 km^2, and is dominated by Kangerdlugssuaq Gletscher (no. 11) at about 50,000 km^2, with Christian IV's Gletscher (no. 18) as the only other basin of significant size. Most of the smaller basins are defined by local topography bordering the basin of Kangerdlugssuaq Gletscher, and drain into Kangerdlugssuaq Fjord. The Kangerdlugssuaq Gletscher basin borders directly onto the Vestfjord Gletscher basin in the north, and the eastern boundaries of these two basins thus form the divide between the Greenland Ice Sheet and the independent flow regime of the Geikie Plateau (Fig. 4.4).

No.	Name of glacier (or adjacent fjord, island, headland etc.)	Terminus latitude (N)	Terminus longitude (W)	Drainage basin area (km^2)	Terminus width (km)	Area to width ratio
19	(no name)	68° 18'	29° 36'	78	1.5	52
20	(Kap Nansen)	68° 16'	29° 28'	31	1.25	25
21	(no name)	68° 19'	29° 20'	23	1.25	18
22	(Kivioqs Fjord)	68° 24'	29° 12'	190	2.75	69
23	Rosenborg Gletscher	68° 24'	28° 48'	1118	2.5	447
24	Kronborg Gletscher	68° 25'	28° 38'	1999	2.0	999
25	(Weidemanns Fjord)	68° 31'	28° 20'	73	1.75	42
26	Borggraven	68° 35'	28° 00'	2414	4.5	536
27	(Grivel Bugt)	68° 32'	27° 45'	95	2.75	35
28	(Grivel Fjord)	68° 35'	27° 30'	218	3.25	67
29	(Savary Fjord)	68° 37'	27° 20'	98	2.5	39
30	Sorte Bræ	68° 39'	26° 57'	1529	5.0	306
31	(no name)	68° 43'	26° 17'	59	3.75	16
32	(Johan Pedersens Bugt)	68° 46'	26° 18'	474	6.25	76
33	Stor Bræ	68° 49'	25° 53'	273	4.5	61
34	(De Reste Bugt)	68° 57'	25° 43'	418	3.75	111
35	(Barclay Bugt S.)	69° 14'	25° 16'	382	2.25	170
36	Dendrit Gletscher	69° 17'	25° 08'	3810	6.25	610
37	(Knighton Bugt)	69° 26'	24° 43'	756	2.25	336
38	(Henry Land)	69° 35'	24° 00'	978	2.5	391
39	Stenos Gletscher	69° 51'	23° 23'	457	1.75	261
40	Torv Gletscher	69° 57'	22° 55'	603	2.25	268
41	Roma Gletscher	69° 59'	22° 34'	48	1.0	48
42	Sfinx Gletscher	70° 01'	22° 28'	19	1.0	19

Table 4.2 Drainage basin areas and terminus locations and widths for tidewater glaciers in the Blosseville Kyst region, from Nansen Fjord to Kap Brewster (Figs. 1.2, 4.1 and 4.4).

Most of the glacier basins which drain along the Blosseville Kyst are relatively small (Table 4.2), and even the largest is less than 4,000 km^2 (Dendrit Gletscher, no. 36). The terrain is Alpine and mountainous in character due to the local bedrock geology (Section 2.3.1), often leading to complex patterns of converging and diverging flow. Apart from Magga Dan Gletscher (no. 50, Table 4.3), the majority of the Geikie Plateau area (approximately 16,000

km^2) is drained to the south-west towards the Blosseville Kyst rather than northwards into Scoresby Sund (Fig. 4.4).

No.	Name of glacier (or adjacent fjord, island, headland etc.)	Terminus latitude (N)	Terminus longitude (W)	Drainage basin area (km^2)	Terminus width (km)	Area to width ratio
43	Østre Borggletscher	70° 07'	23° 36	68	1.75	39
44	Vestre Borggletscher	70° 08'	23° 52'	34	2.0	17
45	Månegletscher	70° 12'	24° 09'	55	1.25	44
46	(no name)	70° 13'	24° 15'	21	2.0	10
47	Solgletscher	70° 13'	24° 28'	64	1.25	51
48	Bredegletscher	70° 16'	25° 14	1131	4.25	266
49	Sydbræ	70° 12	26° 20'	899	5.0	180
50	Magga Dan Gletscher	69° 59'	27° 20'	4119	5.75	716
51	Kista Dan Gletscher	69° 58'	27° 28'	999	3.5	285
52	(no name)	70° 01'	27° 57'	1043	3.5	298
53	Vestfjord Gletscher	70° 23	29° 08'	>>5387 (≈17000)	3.0	≈5500
54	Døde Bræ	70° 27'	29° 07'	209	1.75	119
55	Rolige Bræ	70° 35'	28° 18'	>2986 (≈4500)	3.0	≈1500
56	Eielsen Gletscher	71° 08'	27° 53'	>2345 (≈2600)	4.25	≈600
74	Korridoren (Milne Land)	70° 54'	26° 30	160	1.0	160
57	(north side of Renland)	71° 28'	26° 43'	266	1.5	177
58	Daugaard-Jensen Gletscher	71° 55'	28° 33'	>>2633 (≈50000)	5.5	≈9000
59	Charcot Gletscher	72° 05'	28° 40'	>335	2.0	>167
60	Graah Gletscher	72° 08	28° 36'	>692	2.5	>277
61	Løberen	71° 32'	25° 38'	73	1.0	73

Table 4.3 Drainage basin areas and terminus locations and widths for tidewater glaciers in the Scoresby Sund region (Figs. 4.4 and 4.5). Basin area estimates derived from maps in Bindschadler *et al.* (1989) are given in brackets.

The glaciers of the Scoresby Sund fjord system (Table 4.3) drain a total of approximately 84,000 km^2, of which the majority flows through Daugaard-Jensen Gletscher (no. 58, Table 4.3). There are a further four intermediate-sized glaciers in this region (Vestfjord,

no. 53, Rolige Bræ, no. 55, Magga Dan, no. 50, and Eielsen Gletscher, no. 56), and the rest are relatively small. Several glaciers in this region extend beyond the area of data coverage towards the Inland Ice (Figs. 4.4 and 4.5). Observations of iceberg calving fluxes in Nordvestfjord by Olesen and Reeh (1969) indicate that Charcot and Graah Gletschers (nos. 59 and 60) may be draining significant areas (Section 2.2). Despite the broad terminus for which it is named, Bredegletscher (no. 48) drains only about 1000 km^2 of the Geikie Plateau area.

No.	Name of glacier (or adjacent fjord, island, headland etc.)	Terminus latitude (N)	Terminus longitude (W)	Drainage basin area (km^2)	Terminus width (km)	Area to width ratio
62	Sefstrøms & Gully Gl.	72° 07'	25° 30'	248	5.0	50
63	Hisingers Gletscher	72° 51'	27° 25'	>892	2.0	>446
64	Nordenskiolds Gletscher	73° 07'	27° 43'	>851	2.25	>378
65	Jættegletscher	73° 27'	27° 28'	>1277	2.5	>511
66	Edward de Geer Gletscher	73° 30'	27° 18'	>1103	3.25	>339
67	Nunatak Gletscher	73° 57'	25° 47'	>1355	3.0	>452
68	Waltershausen Gletscher	73° 48'	24° 10'	>2313	10.0	>231
69	Wordie Gletscher	74° 05'	22° 30'	>2811	3.25	>865
70	Granta Gletscher	74° 19'	22° 32'	117	1.0	117
71	Heinkels Gletscher	75° 10'	22° 30'	>719	2.25	>319
72	Einar Mikkelsens Gletscher	75° 33'	22° 30'	>205	1.75	>117
73	Storm Gl. (Brede Fjord)	75° 40'	22° 20'	>60	1.0	>60

Table 4.4 Drainage basin areas and terminus locations and widths for tidewater glaciers in the northern fjord region. Many of the glacier basins in this region lie largely outside the study area (Fig. 4.5).

Of the tidewater termini in the northern fjord region (Table 4.4), all are outlet glaciers whose drainage basins lie largely outside the study area, except Sefstøms and Gully Gletschers (no. 62) which are valley glaciers draining the west side of the Staunings Alper (Fig. 1.2) that merge to form a common piedmont terminus. Several of the glaciers (nos. 65 to 69) appear to have significant basin areas, as their outlet glaciers alone each cover an area of over 1000 km^2. No detailed elevation data are currently available for this region on which an estimate of these drainage basin areas could be based, but the flowline map given in Fig. 2.3 indicates that their combined drainage area could be very large, as the central divide of the Greenland Ice Sheet lies further west in this region than it does in the Scoresby Sund and Kangerdlugssuaq regions to the south. However, Koch (1945, p.112) states that of the

glaciers in this region, only Jætte and Edward de Geer Gletschers (nos. 65 and 66, Table 4.4) produce significant quantities of icebergs, while the others are virtually unproductive.

4.2.2 *Size-Frequency Distribution of Drainage Basin Areas*

A total of 54 drainage basins of tidewater glaciers were determined to lie entirely inside the area covered by the MSS imagery. A histogram showing the distribution of these basin areas, together with the 105 smaller glaciers identified from the maps (Section 4.1 and Figs. 4.4 and 4.5), is presented in Fig. 4.6. The distribution is approximately exponential in form with 75% of all tidewater glaciers in the study area having a basin area of less than 90 km^2. The four largest glaciers in the area (Christian IV's, Vestfjord, Daugaard-Jensen and Kangerdlugssuaq) are not shown on this plot. Of these four drainage basins, only Christian IV's Gletscher lies entirely inside the study area, and was determined to have an area of approximately 9500 km^2 (Table 4.1). The areas of the other three large basins (Tables 4.1 and 4.3) were estimated from the surface slope vector maps of Bindschadler *et al.* (1989), which were produced from satellite radar altimetry. Grid points on these maps are spaced 20 km apart, and these estimates are therefore very approximate.

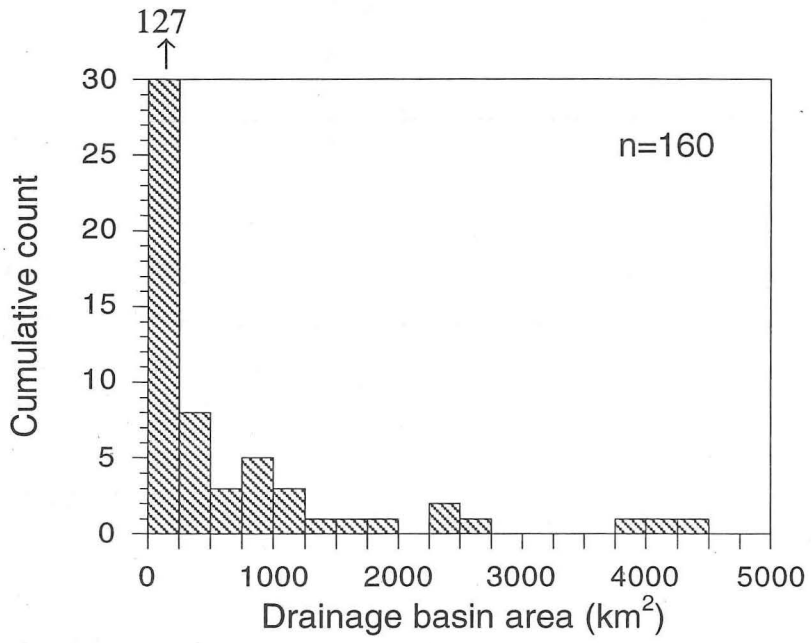

Figure 4.6 Histogram showing the distribution of drainage basin areas within the study area. Not shown are Christian IV (9500 km^2), Vestfjord (≈17,000 km^2), Daugaard-Jensen (≈50,000 km^2) and Kangerdlugssuaq (≈50,000 km^2) Gletschers (Tables 4.1 to 4.4).

4.2.3 *Size-Frequency Distribution of Terminus Widths*

An estimate of the width of each tidewater terminus in the study area was obtained using a combination of digital satellite imagery and the KMS and ICAO maps at a scale of 1:250,000 (Section 4.1.2). Fig. 4.7 shows the distribution of terminus widths for the 74 glaciers identified in Tables 4.1 to 4.4, plus the 105 smaller glaciers which were not digitized (Section 4.1.1). The location of each terminus is shown in Fig. 4.1. As is the case for the basin areas, the distribution is seen to be approximately exponential with 85% of glaciers having a terminus width of 3 km or less.

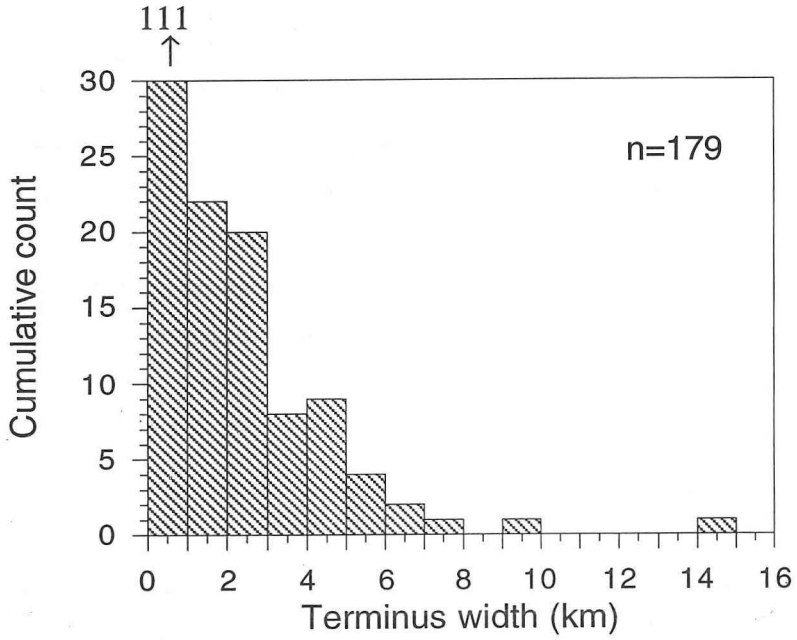

Figure 4.7 Histogram showing the distribution of terminus widths for tidewater glaciers within the study area. The two widest termini are Waltershausen Gletscher (no. 68, 10 km) and Christian IV's Gletscher (no. 18, 15 km) (Tables 4.1 to 4.4).

4.3 INTERPRETATION AND DISCUSSION OF RESULTS

As discussed in the introduction to this chapter, the basin area to terminus width ratio has implications for the dynamic regime and mass balance of tidewater glaciers. Figure 4.8 shows a graph of basin area versus terminus width for the 59 tidewater glaciers within the study area for which the total basin area was determined. Where an estimate of the total basin area was derived from Bindschadler *et al.* (1989), the estimated values are included as data points (Kangerdlugssuaq, Vestfjord Gletscher, Rolige Bræ, Eielsen Gletscher and Daugaard-Jensen Gletscher; see Tables 4.1 and 4.3). Due to the very wide range of basin areas, it was necessary to plot this axis on a logarithmic scale.

A data point in the upper left portion of the graph (i.e. a glacier with a high basin area to terminus width ratio) would have a high balance velocity, and is therefore likely to have a high terminus velocity or to be gaining mass. Similarly, a point on the lower right part of the graph would imply that the glacier has a low balance velocity, and hence would be expected to have a lower terminus velocity, or to be losing mass.

It can be seen from Fig. 4.8 that there is a relationship between the two variables, although the coefficient of correlation is low. This indicates that there is a wide variety of flow regimes in the tidewater glaciers of this area. Kangerdlugssuaq and Daugaard-Jensen Gletscher, in particular, drain very large basin areas through rather narrow termini, and must therefore have high balance velocities. Daugaard-Jensen Gletscher is known to have a mean velocity of approximately 10 m day^{-1} close to its terminus (Olesen & Reeh, 1969) (Section 2.2). This is 50% of the velocity of the terminus of Jakobshavns Isbræ (Echelmeyer *et al.*, 1991), which exhibits the fastest known persistent glacier flow in the world (Section 2.1.2). Kangerdlugssuaq Gletscher has a similar basin area and a slightly narrower terminus than Daugaard-Jensen Gletscher (Tables 4.1 and 4.3), and could therefore be expected to have similar terminus flow velocities.

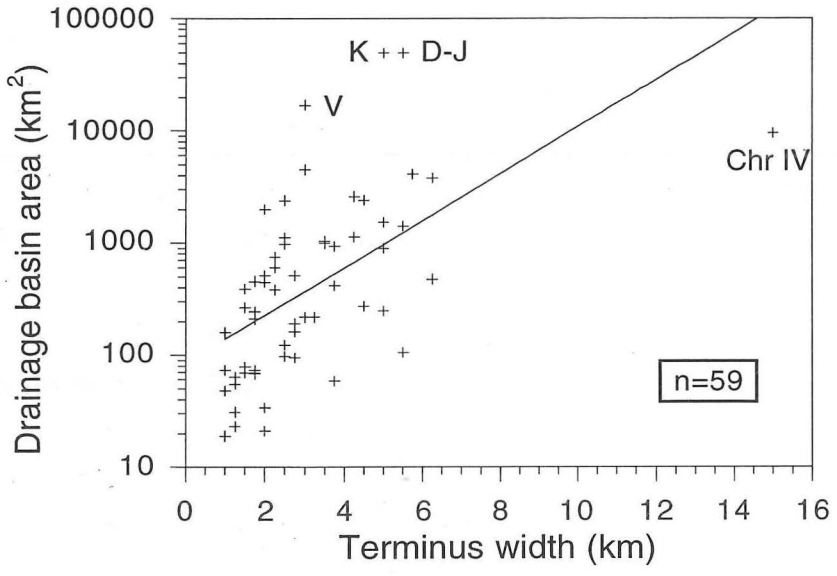

Figure 4.8 Scatter plot showing the relationship between drainage basin area and terminus width for glaciers within the study region terminating in tidewater (Tables 4.1 to 4.4 and Section 4.3). Data points representing Kangerdlugssuaq (K), Daugaard-Jensen (D-J), Vestfjord (V) and Christian IV's (Chr IV) Gletschers are indicated.

The largest of the outlet glaciers in this region (Kangerdlugssuaq, Vestfjord Gletscher and Daugaard-Jensen Gletscher) exhibit strongly convergent flow until only a short distance before the terminus. These glaciers all have a very high basin area to terminus width ratio (Tables 4.1 and 4.3, Fig. 4.8), and are known to have high flow velocities (Olesen & Reeh, 1969; Henriksen, 1973; Reeh & Olesen, 1986). Christian IV Gletscher (no. 18, Table 4.1) appears to be anomalous for this region (Fig. 4.8), as it has a very wide terminus, but only an intermediate basin area, and would therefore be expected to have a low balance velocity. The ratio of basin area to terminus width also shows some correlation with observed iceberg flux rates, as Daugaard-Jensen and Vestfjord Gletschers are known to have high calving rates (Section 2.2) (Olesen & Reeh, 1969; Henriksen, 1973), whereas Christian IV's and Waltershausen Gletschers are observed by Koch (1945, p.116) to be 'large but slightly productive'.

4.4 IDENTIFICATION OF SURGE-TYPE GLACIERS FROM DIGITAL LANDSAT MSS IMAGES

Surging glaciers are those which periodically undergo a sudden increase in velocity, transporting large quantities of ice down-glacier in a relatively short period of time (Sharp, 1988). The mechanisms controlling surges are not fully understood (Raymond, 1987), and the distribution of surging glaciers, in Greenland and elsewhere, is not well determined (Weidick *et al.*, 1992).

Two glaciers in the Staunings Alper (Fig. 1.2) are reported to have surged, based on repeated observations. These are Bjørnbo Gletscher, which terminates on land in Schuchert Dal (Fig. 1.2) (Rutishauser, 1971), and Løberen (no. 61 Table 4.3), which apparently advanced 7 km in 17 years and now reaches the sea at the southern end of Nordvestfjord (Fig. 4.9) (Henriksen & Watt, 1968). Several glaciers in the Blosseville Kyst region, between Scoresby Sund and Kangerdlugssuaq (Fig. 4.1), have been reported to show features associated with surge-type behaviour, such as surface pitting and looped moraines (Meier & Post, 1969). These include an unnamed glacier calving into Johan Pedersen Bugt (no. 32, Table 4.2) (Weidick, 1988), and Torv Gletscher (Fig. 4.10 and no. 40, Table 4.2) at the northern end of the Geikie Plateau (Rucklidge, 1966). Weidick (1988) reports that a total of 26 glaciers in this region show evidence of possible surge behaviour, based on a study of aerial photographs from 1981, but unfortunately the exact locations of these glaciers were not available (A. Weidick, pers. comm.).

Despite the rather coarse resolution of the Landsat MSS imagery (56 m by 79 m, Section 3.1) relative to the size of the features, lobate moraines and/or surface pitting could be identified on several glaciers in the Staunings Alper and Blosseville Kyst regions, including the four mentioned above. Bjørnbo Gletscher exhibits both pitting and looped moraines in its

Figure 4.9 Part of scene 227/010, band 4 acquired on 20 Sept 1988 (Fig. 8, Appendix 1) showing several possible surge-type glaciers in the Staunings Alper. Looped moraines and surface pitting can be seen on the lower reaches of Bjørnbo and Roslin Gletschers (Section 4.4). The area shown is approximately 55 km by 55 km (N.B. image is distorted in the ratio 56.79, Section 3.1).

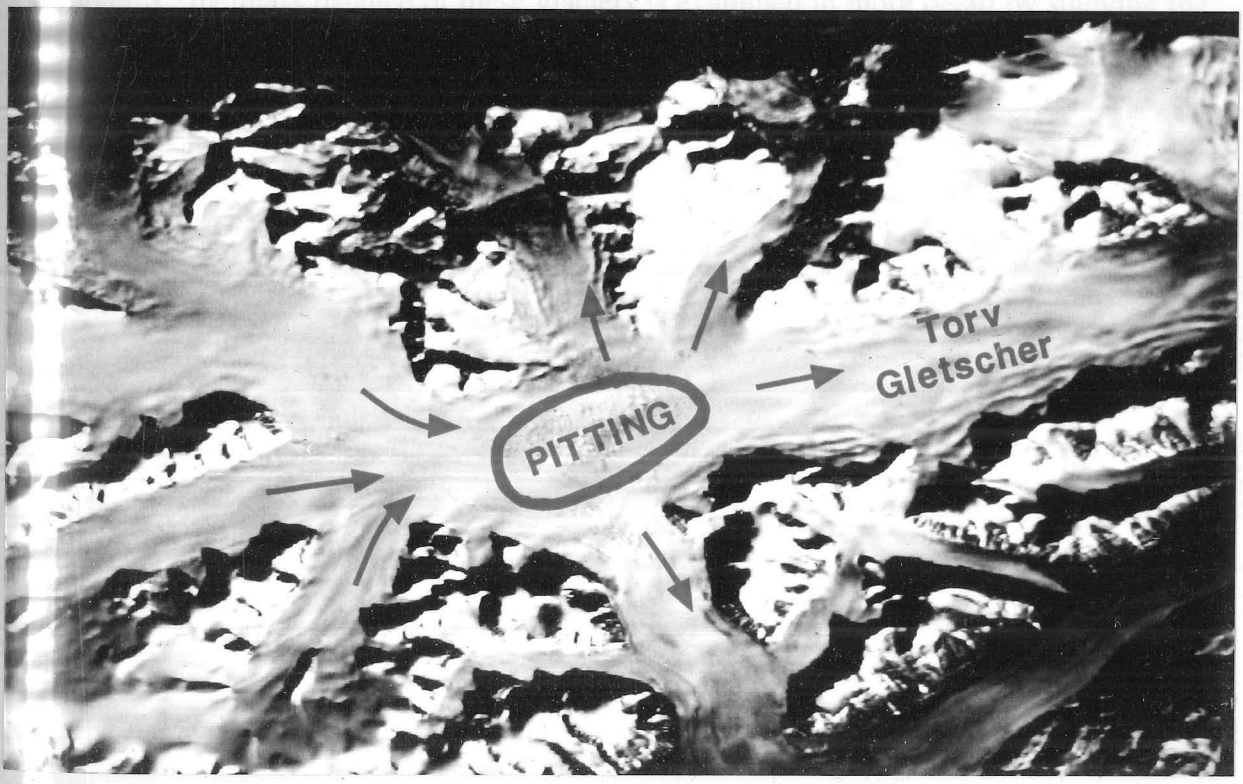

Figure 4.10 Another part of the same scene showing surface pitting on Torv Gletscher (no. 40, Table 4.2). The area shown is approximately 45 km across by 40 km. Flow directions inferred from surface flow features are indicated on the overlay.

Figure 4.9 Part of scene 227/010, band 4 acquired on 20 Sept 1988 (Fig. 8, Appendix 1) showing several possible surge-type glaciers in the Staunings Alper. Looped moraines and surface pitting can be seen on the lower reaches of Bjørnbo and Roslin Gletschers (Section 4.4). The area shown is approximately 55 km by 55 km (N.B. image is distorted in the ratio 56:79, Section 3.1).

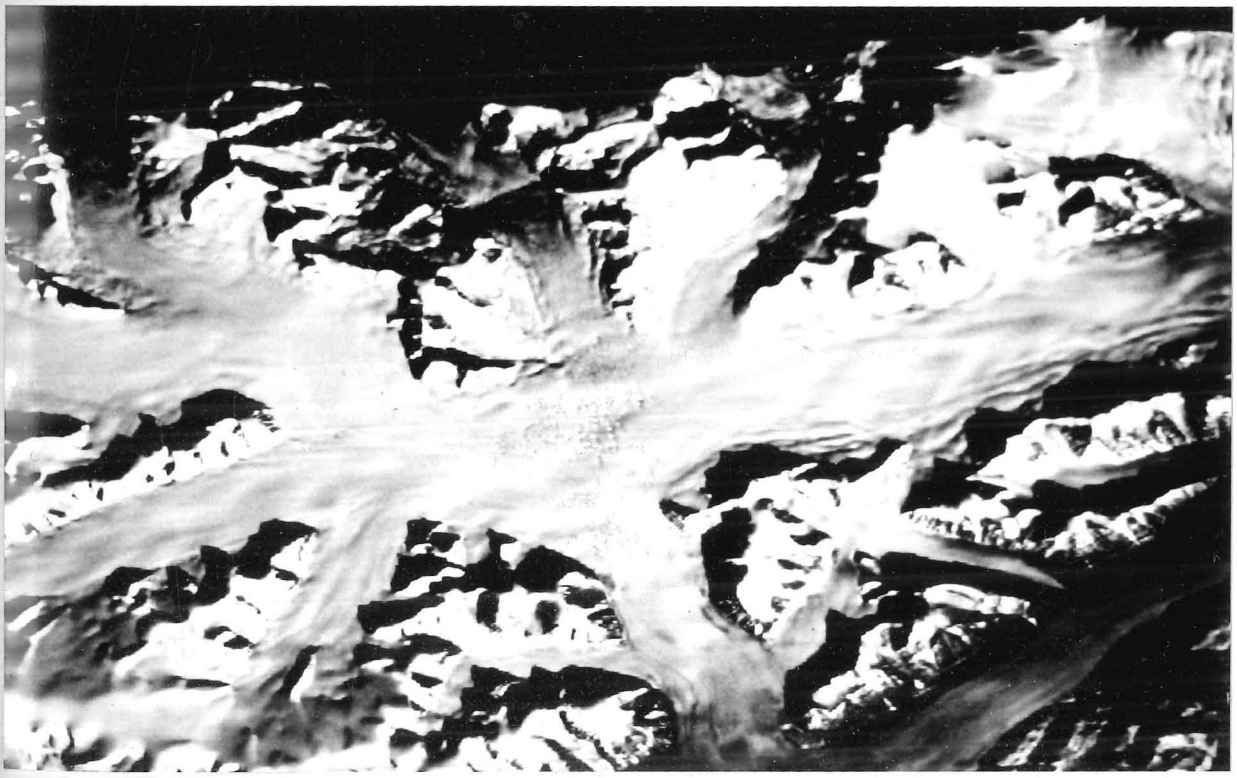

Figure 4.10 Another part of the same scene showing surface pitting on Torv Gletscher (no. 40, Table 4.2). The area shown is approximately 45 km across by 40 km. Flow directions infered from surface flow features are indicated on the overlay.

lower reaches (Fig. 4.9), and the glacier calving into Johan Pedersen Bugt shows pitting over the entire surface. An aerial photograph taken in 1981 (Fig. 3 in Weidick, 1988), shows this pitting in greater detail. Other glaciers showing such features include Sorte Bræ (no. 30, Table 4.2), the left-hand branch of Borgbjerg Gletscher, which terminates on land 10 km to the west of Løberen (Fig. 4.9), and Sorgenfri Gletscher (no. 16 in Table 4.1 and Fig. 2 in Appendix 1) which shows a series of loops in the medial moraine between the main glacier and a side branch.

In conclusion, it appears likely that Landsat MSS imagery can be used to identify possible surge-type behaviour, although further comparison with aerial photography is necessary. A time series of Landsat imagery could also be used to monitor surge behaviour in East Greenland, as has been done in other areas (Dowdeswell, 1986b; Espizua & Bengochea, 1990). Repeated aerial photography is not available for many areas in East Greenland (Weidick, 1988), but considerable Landsat coverage is available for the past 20 years.

The drainage basin data presented in this chapter are fundamental to the understanding and modelling of the mass balance, flow regime and impact on the marine environment of the glaciers in this region. Comparing the basin areas and terminus widths has given an indication of the relative balance velocities which would be expected for each tidewater glacier. In Chapter 5, the mass balance of these glaciers is examined in more detail by studying the snowline elevations, and their variation with latitude and continentality.

Chapter 5

INVESTIGATION OF SNOWLINE ELEVATIONS IN EAST GREENLAND

The aim of this Chapter is to investigate the regional variation of the snowline elevation within the study area using digital Landsat MSS data, as a step towards assessing the mass balance of East Greenland glaciers. The reliability of snowline elevation data from Landsat imagery is investigated by repeated measurements from overlapping images.

5.1 BACKGROUND

The elevation of the transient snowline, which is the boundary between the snow and ice facies on a glacier at any given point in the year, was determined for the tidewater glaciers within the study area. In the absence of superimposed ice, the position of the snowline at the end of the balance year can be considered equivalent to the equilibrium line, which separates the accumulation and ablation areas of an ice mass (Paterson, 1981, p. 53). Superimposed ice, which is formed by the refreezing of meltwater, complicates this distinction as it forms part of the accumulation area, but is nonetheless an ice facies. It is not known whether superimposed ice is widespread in East Greenland (Section 2.1.7).

Studies in West Greenland (Braithwaite, 1984), Svalbard (Lefauconnier & Hagen, 1990), South-East Alaska (Pelto, 1987), Norway and Canada (Østrem, 1975) have shown that a linear correlation exists between the equilibrium line altitude (ELA) and the mass balance of a given glacier. This correlation depends on the precipitation rate in a region and the flow regime of a glacier, and therefore varies greatly from one location to another depending on the latitude, degree of continentality and local topography and bedrock geology. Hence, field validation is necessary to obtain the absolute value of the mass balance for each glacier, but relative values of mass balance over a region or a time series can be obtained by monitoring the ELA using remotely sensed imagery.

The various types of snow and ice found on a glacier have been sub-divided by several authors using the facies concept (Benson, 1962; Paterson, 1981; Williams *et al.*, 1991). Not all the boundaries between these facies are apparent on the surface (Paterson, 1981,

p.7), but those that are can often be detected using satellite imagery (Williams, 1987). A longitudinal profile of satellite-recorded reflectance values from high to low elevations on a glacier shows a transition from higher to lower reflectance values (Williams *et al.*, 1991). Validation studies have shown favourable comparisons between satellite-derived reflectance measurements and values obtained on the ground (Hall *et al.*, 1989; Hall *et al.*, 1990), and have demonstrated that the spectrally similar zones of higher and lower reflectances correspond to snow and ice facies, respectively (Hall *et al.*, 1987).

5.2 METHODOLOGY

Validation of the haze correction procedure described in Section 3.3.4 showed that the most consistent reflectance values for snow and ice were given by bands 2 and 3 (Fig. 3.4 c, d). These two bands would therefore be expected to give the most reliable values for the snowline elevation, enabling scene-to-scene and multi-temporal comparisons to be made. It was decided to use band 3 data for the determination of snowlines, as this sensor represented a compromise between the increased likelihood of saturation at shorter wavelengths (Dowdeswell & McIntyre, 1986), and the increasing sensitivity to solar elevation and grain size effects at longer wavelengths (Wiscombe & Warren, 1980; Yamanouchi, 1983; Aoki, 1991). All reflectance values used in the following analyses are therefore band 3 data, with a wavelength range of 0.7 to 0.8 μm (Section 3.1).

5.2.1 Determination of Snowlines Using Reflectance Profiles

To locate the snowline on the glaciers studied, it was first necessary to identify the reflectance values representing the transition from snow to ice. This was done by extracting a transect of reflectance values along a longitudinal profile down each of several glaciers for each scene. Figure 5.1 shows examples of these profiles from scenes 230/012 (4 September 86) and 226/011 (10 August 87). Figures 5.2 and 5.3 show a part of each of these scenes with the location of the profiles marked.

These profiles show two spectrally similar zones, one of high and one of low reflectance values, separated by a transition zone (Fig. 5.1). The boundaries between the zones are generally characterised by a sharp change in gradient in these examples, although this was not the case for all of the glaciers investigated due to complexities in the surface features (Section 5.2.2). The transition zone from high to low reflectivities is generally narrow for the examples shown in Fig. 5.1 (an average of about 50 pixels, equivalent to 3 to 4 km on the ground), but depends on such factors as the surface slope, orientation and flow regime.

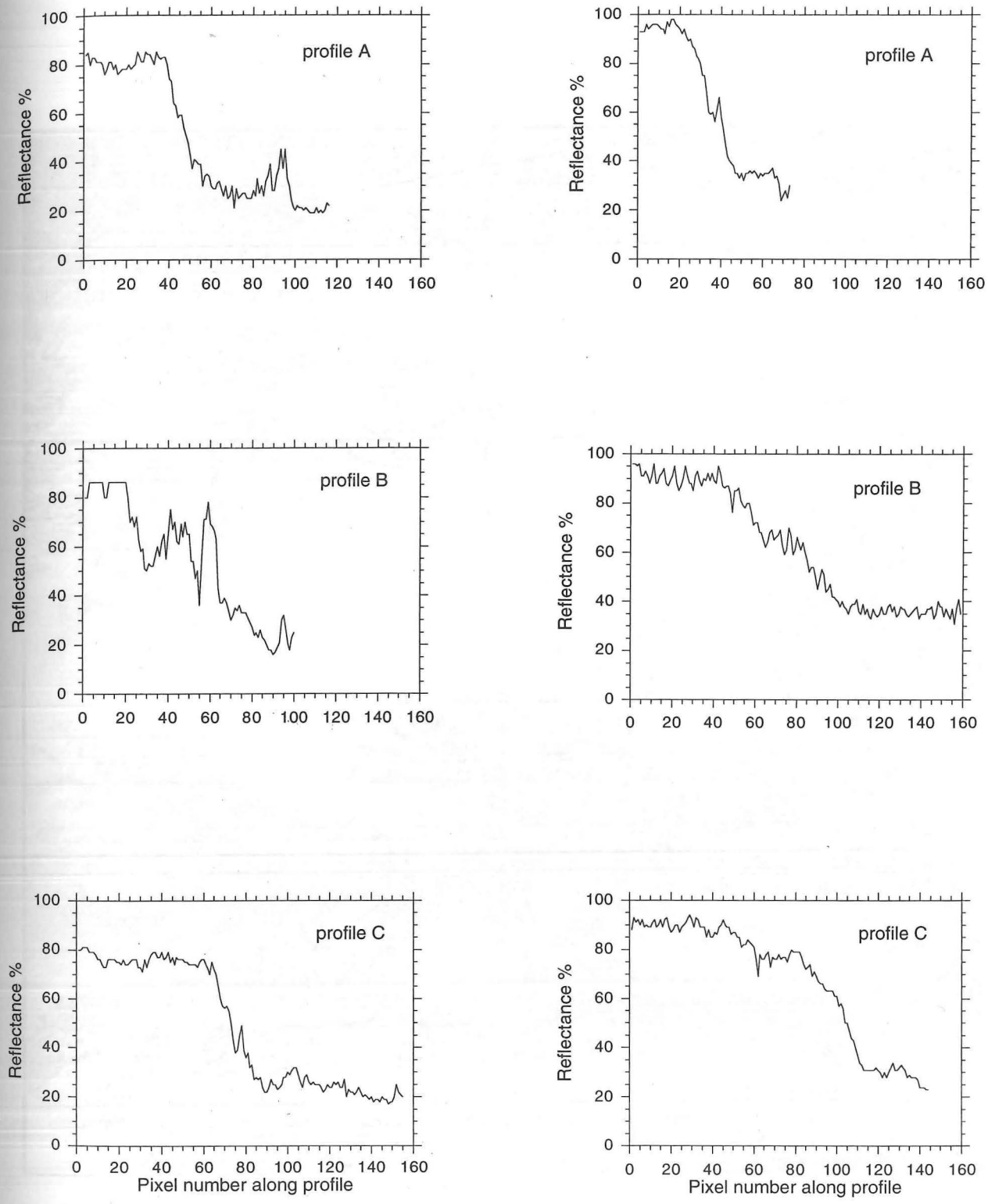

Figure 5.1 Examples of reflectance profiles from scene 226/011 acquired on 10 August 1987 (left column) and scene 230/012 acquired on 4 September 1986 (right column). The location of each profile is indicated on Figures 5.2 and 5.3, respectively. The x-axis scale is in pixels where one pixel represents between 56 m and 79 m depending on the orientation of the profile (Section 3.1). The three zones which can generally be seen indicate ice, slush and snow in order of decreasing reflectance (Section 5.2.1). Data are from MSS band 3 (0.7 to 0.8 μm). Note that profile B from 226/011 shows saturation in the snow zone.

Figure 5.2 Location of profiles A, B and C on scene 226/011, band 3. Profile A (bottom right) is on a tributary of Dendrit Gletscher (no. 36); profile B (centre) is on a tributary of glacier no. 37 and profile C (upper left) is on Bredegletscher (no. 48). Note the striping apparent where the band 3 sensor is saturated over the Geikie Plateau ice cap (Section 3.1).

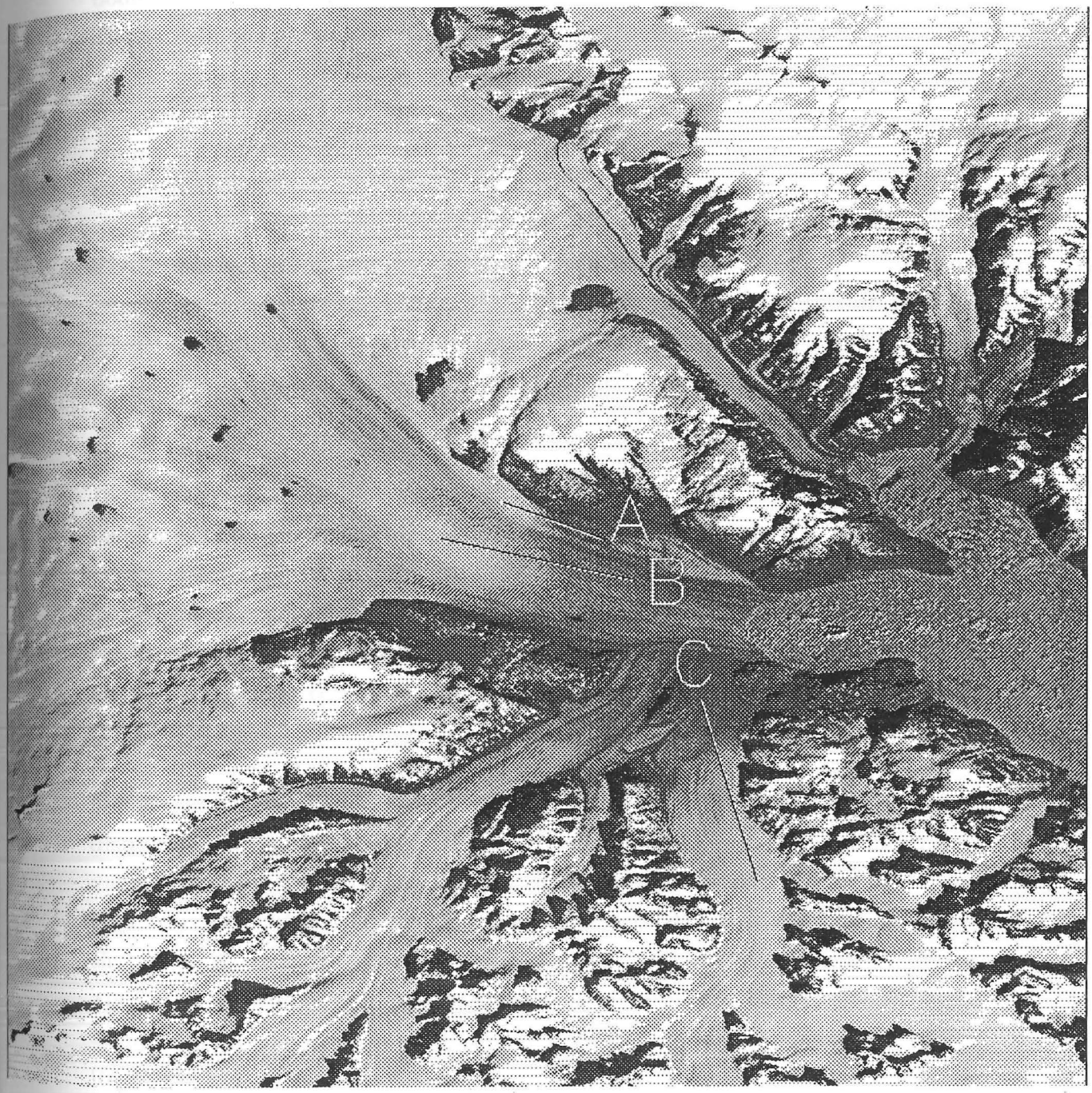

Figure 5.3 Location of profiles A, B and C for scene 230/012, band 3 data, showing terminus area of Kangerdlugssuaq Gletscher (no. 11) and head of Kangerdlugssuaq Fjord.

This transition zone, also evident on reflectance profiles from TM band 4 imagery of Iceland, is assumed by Williams *et al.* (1991) to represent a 'slush zone' of completely water-saturated snow, which is thus part of the accumulation area. They define the boundary between the transition zone and the zone of higher reflectance as the 'slush limit'. The snowline is generally defined to be the lower end of the wet snow zone (Benson, 1962; Paterson, 1981), and is thus represented by the break of slope between the slush zone and the zone of lower reflectance, representing ice (Fig. 5.1). If superimposed ice is not present, then it is this boundary at the end of the ablation season which represents the equilibrium line.

The reflectance value at this lower boundary was determined for each of the 16 MSS images used (Table 5.1), except where new snow obscured the snowlines (227/010, 227/012), insufficient snowlines were present in the scene (230/011, 228/009, 229/008) or the scene was acquired significantly before the end of the ablation season (229/010). For most of these cases, there was sufficient overlap between the scenes that the area was covered by other images, but unfortunately scene 227/012 (Figure 1, Appendix 1) covers 16 tidewater termini which are not included in any other scenes. Snowline elevations could therefore not be determined for this section of the Blosseville Kyst (Fig. 5.6).

These values were confirmed visually on the graphics screen of the image analysis workstation by interactively highlighting the reflectance categories around the transition zone one at a time (Fig. 5.4). For the values typical of the ice areas (Fig. 5.1), each category showed a wide spatial distribution, as would be expected since these zones are reasonably constant in reflectance values. Stepping up one category at a time, the sharp boundary of the transition zone was recognisable as a distinct reduction in the spatial distribution of each reflectance category. This point on the reflectance scale represents a value just above the noise level of the signal for the ice zone, and so the downslope boundary of the pixels with this reflectance value was taken to be the snowline. Figure 5.4 shows a screen image of part of scene 230/012 with two reflectance categories highlighted. The pixels shown in red have a reflectance of 34–36%, which is typical for ice on this scene (Fig. 5.1) and the green pixels have a reflectance of 50–52%, which is in the transition zone. The line between the red and green pixels was thus taken to be the snowline. The location of this line was identified on the 1:250,000 KMS or AMS maps, and the elevation was read off from the contours. For the northernmost glaciers (nos. 71–73), and for Charcot and Graah Gletschers (nos. 59 and 60), which are not shown on the KMS map of the area, the elevations were estimated using the 1:1,000,000 World Aeronautical Chart (WAC) series maps published by the US Air Force.

Figure 5.4 Part of scene 230/012, band 3 (4 September 1986) illustrating the method used to determine the location of the snowline. Pixels highlighted in red have a reflectance value of 34–36%, which represents the top of the ice zone (Fig. 5.1) and those highlighted in green have a reflectance of 50–52%, which is in the transition zone representing saturated snow (Section 5.2.1). The snowline therefore lies between these two areas.

Scene path/row	Scene date	Snowline reflectance value
229/010	30 June 88	(too early)
227/010	6 Aug 89	22%
226/011	10 Aug 87	32%
229/008	15 Aug 87	(no snowlines)
230/009	22 Aug 87	58%
230/010	22 Aug 87	46%
230/007	22 Aug 87	60%
228/009	24 Aug 87	(no snowlines)
228/010	24 Aug 87	31%
231/008	29 Aug 87	53%
229/011	31 Aug 87	42%
230/011	4 Sept 86	(no snowlines)
230/012	4 Sept 86	34%
226/011	8 Sept 89	31%
227/012	20 Sept 88	(new snow)
227/010	20 Sept 88	(new snow)

Table 5.1 Reflectance values representing the snowline for each image used (or reason for not using, as appropriate). Scenes are listed in chronological order through the year, and their locations are shown in Fig. 3.2

There is a large variation in the reflectance values at the snowlines given in Table 5.1, but there does not appear to be any correlation with the date. Seven of the images for which snowlines were determined are from August 1987, which appears to have been an exceptionally clear month, with no cloud cover apparent on any of the scenes. Although it might be expected that this clear spell would affect the reflectance value at the snowline, there is no discernible trend through the month. The possible effect on the elevation of the snowline is discussed in Section 5.3. The snowline reflectance values do appear to vary with latitude, however, with the southern images (from rows 012, 011 and 010, Fig. 3.2) having reflectance values from 22% to 46%, while the northern images (rows 009, 008 and 007) give values from 53% to 68%. This could be due to the temperature gradient, with the colder temperatures in the north of the region slowing down the metamorphosis of the snow grains which causes their reflectance at these wavelengths to decrease with age (O'Brien & Munis, 1975). Alternatively, there may have been a more recent snowfall in the north of the region.

It is not possible to draw definite conclusions about the reliability of the snowline determination based on the evidence available, since the date of the end of the balance year can vary from one year to the next, and late summer snowfall can occur before the end of the melt season. The ideal situation would be to acquire a time series of images for one location covering the later part of each year's melt season, in order to determine the end of the balance year, and then obtain a latitudinal series of images acquired close to this date. Given the constraints of the 16 day repeat time, the frequency of cloud cover and the large number of scenes this would involve, this is clearly not feasible in practice.

5.2.2 Accuracy of Snowline Elevations Determined Using Landsat MSS Data

Uncertainty in the elevation of the snowline, as determined using this method, can be a result of any of the following problems:

- errors in determining the reflectance boundary from the profiles
- wide spatial distribution of this boundary value leading to uncertain location of snowline on satellite image, especially on the broad, fast-flowing glaciers, e.g. Daugaard-Jensen Gletscher (no. 58) and Christian IV's Gletscher (no. 18)
- error locating this line on the topographic maps
- inaccurate or non-existant elevation data; inconsistant or poorly labelled contours
- the orientation of the surface relative to the sun can affect the apparent reflectivity of the snow, and deep shadowing on a steep, north-facing glacier can obscure the snowline altogether (e.g. on the north side of Scoresby Sund, nos. 45 to 47), as can shadowing from adjacent mountains (e.g. Fig. 4.10).
- the snowline as determined from the reflectance values may not run parallel to map contours, and thus a unique snowline elevation cannot be determined (e.g on Sfinx Glacier, no. 42, the apparent snowline runs almost parallel to the axis of the glacier, probably due to shadowing effects)
- crevasses, surface moraine and meltwater pools can cause the snow surface to appear darker, thus mimicking an area of lower reflectance
- scenes are not all from the end of the melt season
- the end of the melt season may not be consistent from year to year
- accumulation in the form of new snow may occur before the end of the melt season

It can be seen from Fig. 5.4 that the horizontal distance represented by the reflectance interval from 35 to 50% is approximately 1–2 km for Kangerdlugssuaq Gletscher and its two major tributaries, representing a height difference of about 100 m. The error in identifying the location of the snowline on the map by comparing with the image is of the same order of magnitude. Uncertainties in the elevations given on the maps are thus unlikely to be significant.

In general, the reflectance profiles for the northern glaciers were flatter, with higher reflectance values for ice, lower values for snow and a broader, shallower transition zone (Table 5.1). Figure 5.5 shows reflectance profiles for Edward de Geer and Nunatak Gletschers (nos. 66 and 67, Fig. 4.1) from scene 231/008. This means that there is greater uncertainty in determining the threshold reflectance value, and also a greater margin of error in the horizontal location of the snowline. The resulting uncertainty in determining the elevation of the snowline depends on the surface gradient of the glacier in question, since the steeper the surface, the greater the vertical error introduced.

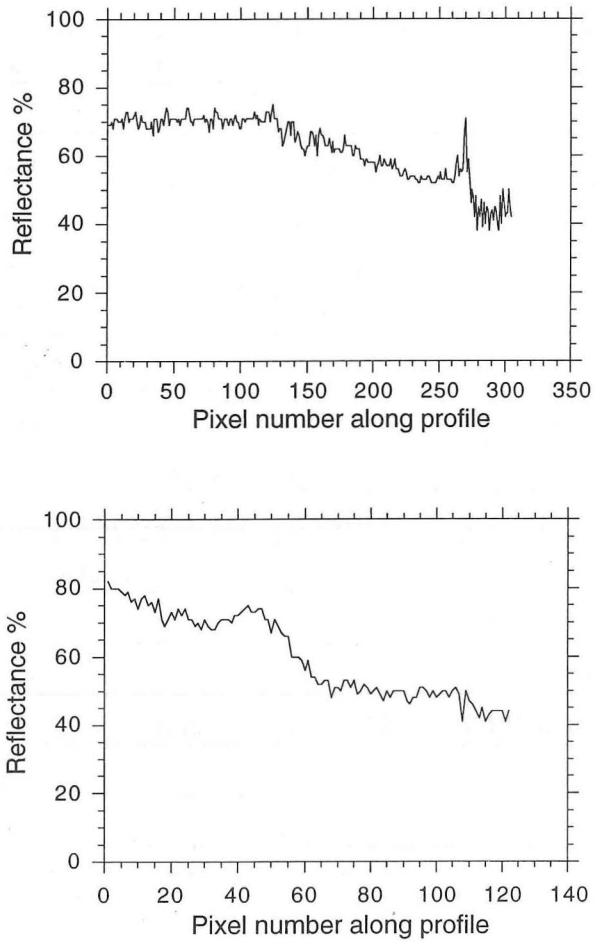

Figure 5.5 Reflectance profiles for Edward de Geer Gletscher (no. 66) and Nunatak Gletscher (no. 67). These profiles demonstrate the broad transition zone between snow and ice facies typical of the glaciers in the northern fjord region (Section 5.2.2). The location of the snowline is not obvious on these profiles, and hence the determination of snowline elevations is subject to greater uncertainties than for the glaciers further south where the transition is more clearly defined.

5.3 RESULTS

A value of the snowline elevation was determined as described in the previous section for each of the 74 tidewater glacier termini, except where new snow or shadow obscured the snowline (Section 5.2.1). The results are presented in Tables 5.2 to 5.5 for each of the four regions within the study area as marked on Fig. 4.1.

No.	Name of glacier (or adjacent fjord, island, headland etc.)	Scene path/row	Scene date	Snowline elevation (m)
1	(no name)	230/012	4 Sept 86	200
2	Nordre & søndre parallel gl.	230/012	4 Sept 86	300
3	(Fladø)	230/012	4 Sept 86	200
4	Hutchinson Gletscher	230/012	4 Sept 86	200
5	(no name)	230/012	4 Sept 86	100
6	(no name)	230/012	4 Sept 86	150
7	(Kvadderbugt)	230/012	4 Sept 86	250
8	(Amdrup Fjord)	230/012	4 Sept 86	400
9	Kælvegletscher	230/012	4 Sept 86	350
10	(Kangerdlugssuaqs Tinde)	230/012	4 Sept 86	200
11	Kangerdlugssuaq Gletscher	230/012	4 Sept 86	500-600
12	Nordfjord Gletscher	230/012	4 Sept 86	350
13	Styrte Gletscher	230/012	4 Sept 86	800
14	Courtauld Gletscher	230/012	4 Sept 86	250
15	Frederiksborg Gletscher	230/012	4 Sept 86	650
16	Sorgenfri Gletscher	230/012	4 Sept 86	500
17	(Ryberg Fjord)	230/012	4 Sept 86	150
18	Christian IV's Gletscher	230/012	4 Sept 86	200-300

Table 5.2 Snowline elevations for tidewater glaciers on the East Greenland coast between Kangerdlugssuaq Fjord and Nansen Fjord (Fig. 1.2). Glacier names are given in Table 4.1, and terminus positions are marked on Fig. 4.1.

In cases where the snowline elevation of a glacier could be determined from more than one image, all values obtained are given in the tables for comparison. The scene number and date from which each elevation estimate was obtained is listed. For the larger glaciers, the snowline was often a zone rather than a sharp transition, and so a range of values is given.

Where the snowline occured across several tributaries of a glacier, an average value is given, although the variation between tributaries was usually minimal.

For the glaciers of the Kangerdlugssuaq region (Table 5.2), all elevations were obtained from the same image, and can therefore be compared directly. Snowlines are generally low in this region (200–300 m) with a few notable exceptions. Kangerdlugssuaq Gletscher is very different in nature to the other glaciers in the region, as it is a fast-flowing outlet of a very large drainage basin (Section 4.2.1), and has a somewhat higher snowline than the smaller glaciers. Styrte Gletscher (no. 13) has by far the highest snowline in the area, and those of Sorgenfri and Frederiksborg Gletschers are also higher than average. The possible reasons for this are discussed in Section 5.4.1.

Unfortunately, a snowline elevation could not be determined for many of the glaciers in the Blosseville Kyst region (Table 5.3), since scene 227/012 of 20 September 1988 appears to have been acquired shortly after a snowfall (Fig. 1, Appendix 1). However, Borggraven (no. 26) can be seen in the corner of image 229/011 (Fig. 5, Appendix 1), and so an elevation estimate was obtainable in this case. This elevation (350 m, Table 5.3) is consistent with the values obtained further south in the Kangerdlugssuaq region (Table 5.2), despite the two images being acquired in different years. For glaciers 33–35, no estimate could be obtained, as no step was apparent in the reflectance profile. For Sfinx Gletscher (no. 42) the apparent snowline appeared to run almost parallel down the length of the glacier, possibly due to shadowing from the steep topography along the northern coast of the Geikie Plateau.

The snowline elevations in the Scoresby Sund fjord region are nearly all from August 1987, and show a high degree of consistency, with a mean of 900 m and a standard deviation of 250 m (Table 5.4). Snowline elevations could not be obtained for three of the smaller glaciers on the north side of the Geikie Plateau due to shadowing (nos. 45–47, table 5.4) (see also photograph, Fig. 4.10).

Just as for Kangerdlugssuaq Gletscher (no. 11), Daugaard-Jensen Gletscher (no. 58) exhibits a transition zone rather than a sharp dividing line between ice and snow facies. The snowline elevation for Daugaard-Jensen Gletscher is also higher than the average for the area, although not markedly so.

The snowline estimates for the northern fjords region show a very wide range, from over 1000 m for nos. 63 to 68 dropping sharply to 450 m for nos. 69 to 72 (Table 5.5). Within each of these two areas, however, the elevations are consistent. Possible explanations for this pattern are discussed in section 5.4.1 below.

No.	Name of glacier (or adjacent fjord, island, headland etc.)	Scene path/row	Scene date	Snowline elevation (m)
19	(no name)	227/012	20 Sept 88	—
20	(Kap Nansen)	227/012	20 Sept 88	—
21	(no name)	227/012	20 Sept 88	—
22	(Kivioqs Fjord)	227/012	20 Sept 88	—
23	Rosenborg Gletscher	227/012	20 Sept 88	—
24	Kronborg Gletscher	227/012	20 Sept 88	—
25	(Weidemanns Fjord)	227/012	20 Sept 88	—
26	Borggraven	229/011	31 Aug 87	350
27	(Grivel Bugt)	227/012	20 Sept 88	—
28	(Grivel Fjord)	227/012	20 Sept 88	—
29	(Savary Fjord)	227/012	20 Sept 88	—
30	Sorte Bræ	227/012	20 Sept 88	—
31	(no name)	227/012	20 Sept 88	—
32	(Johan Pedersens Bugt)	227/012	20 Sept 88	—
33	Stor Bræ	226/011	10 Aug 87	—
34	(De Reste Bugt)	226/011	10 Aug 87	—
35	(Barclay Bugt S.)	226/011	10 Aug 87	—
36	Dendrit Gletscher	226/011 226/011	10 Aug 87 8 Sept 89	1000 800
37	(Knighton Bugt)	226/011	10 Aug 87	1000
38	(Henry Land)	226/011 226/011	10 Aug 87 8 Sept 89	700 800
39	Stenos Gletscher	226/011 226/011	10 Aug 87 8 Sept 89	600 600
40	Torv Gletscher	226/011 226/011	10 Aug 87 8 Sept 89	1000 600
41	Roma Gletscher	226/011	10 Aug 87	800
42	Sfinx Gletscher	226/011	10 Aug 87	—

Table 5.3 Snowline elevations for tidewater glaciers in the Blosseville Kyst region of East Greenland between Nansen Fjord and Kap Brewster (Fig. 1.2). Glacier names are given in Table 4.2, and terminus positions are marked on Fig. 4.1.

No.	Name of glacier (or adjacent fjord, island, headland etc.)	Scene path/row	Scene date	Snowline elevation (m)
43	Østre Borggletscher	226/011	10 Aug 87	900
44	Vestre Borggletscher	226/011	10 Aug 87	1000
45	Månegletscher	226/011	10 Aug 87	—
46	(no name)	226/011	10 Aug 87	—
47	Solgletscher	226/011	10 Aug 87	—
48	Bredegletscher	226/011 228/010 226/011	10 Aug 87 24 Aug 87 8 Sept 89	900 1000 600
49	Sydbræ	226/011 228/010 226/011	10 Aug 87 24 Aug 87 8 Sept 89	1200 1700 800
50	Magga Dan Gletscher	229/011	10 Aug 87	600
51	Kista Dan Gletscher	229/011	10 Aug 87	800
52	(no name)	229/011	10 Aug 87	600
53	Vestfjord Gletscher	229/011	10 Aug 87	700
54	Døde Bræ	230/010	22 Aug 87	700
55	Rolige Bræ	230/010	22 Aug 87	800
56	Eielsen Gletscher	230/010	22 Aug 87	800
74	Korridoren (Milne Land)	230/010	22 Aug 87	900
57	(north side of Renland)	230/009	22 Aug 87	900
58	Daugaard-Jensen Gletscher	230/009	22 Aug 87	1000-1300
59	Charcot Gletscher	230/009	22 Aug 87	1100
60	Graah Gletscher	230/009	22 Aug 87	700
61	Løberen	230/009	22 Aug 87	1100

Table 5.4 Snowline elevations for tidewater glaciers in the Scoresby Sund fjord system (Fig. 1.2). Glacier names are given in Table 4.3, and terminus positions are marked on Fig. 4.1.

No.	Name of glacier (or adjacent fjord, island, headland etc.)	Scene path/row	Scene date	Snowline elevation
62	Sefstrøms & Gully Gl.	230/009	22 Aug 87	600
63	Hisingers Gletscher	230/009	22 Aug 87	1200
64	Nordenskiolds Gletscher	231/008	29 Aug 87	1500
65	Jættegletscher	231/008	29 Aug 87	1300
66	Edward de Geer Gletscher	231/008	29 Aug 87	1100
67	Nunatak Gletscher	231/008	29 Aug 87	1100
68	Waltershausen Gletscher	231/008	29 Aug 87	1100
69	Wordie Gletscher	230/007	22 Aug 87	450
70	Granta Gletscher	230/007	22 Aug 87	450
71	Heinkels Gletscher	230/007	22 Aug 87	450
72	Einar Mikkelsens Gletscher	230/007	22 Aug 87	450
73	Storm Gl. (Brede Fjord)	230/007	22 Aug 87	300

Table 5.5 Snowline elevations for tidewater glaciers in the northern fjord region (Fig. 1.2). Glacier names are given in Table 4.4, and terminus positions are marked on Fig. 4.1.

5.4 INTERPRETATION AND DISCUSSION OF RESULTS

5.4.1 Regional Trends in Snowline Elevations

The snowline elevations for East Greenland obtained in this study show a general trend increasing northwards from about 200 m in the area immediately south of Kangerdlugssuaq Fjord, to over 1000 m at the head of the Kejser Franz Josef and Kong Oscars Fjords in the north of the study area (Fig. 5.6). There are some noticeable exceptions to this trend, however, such as the anomalously high snowline on Styrte Gletscher (Table 5.2), and the sharp drop in snowline elevations for the five northernmost glaciers (Table 5.5).

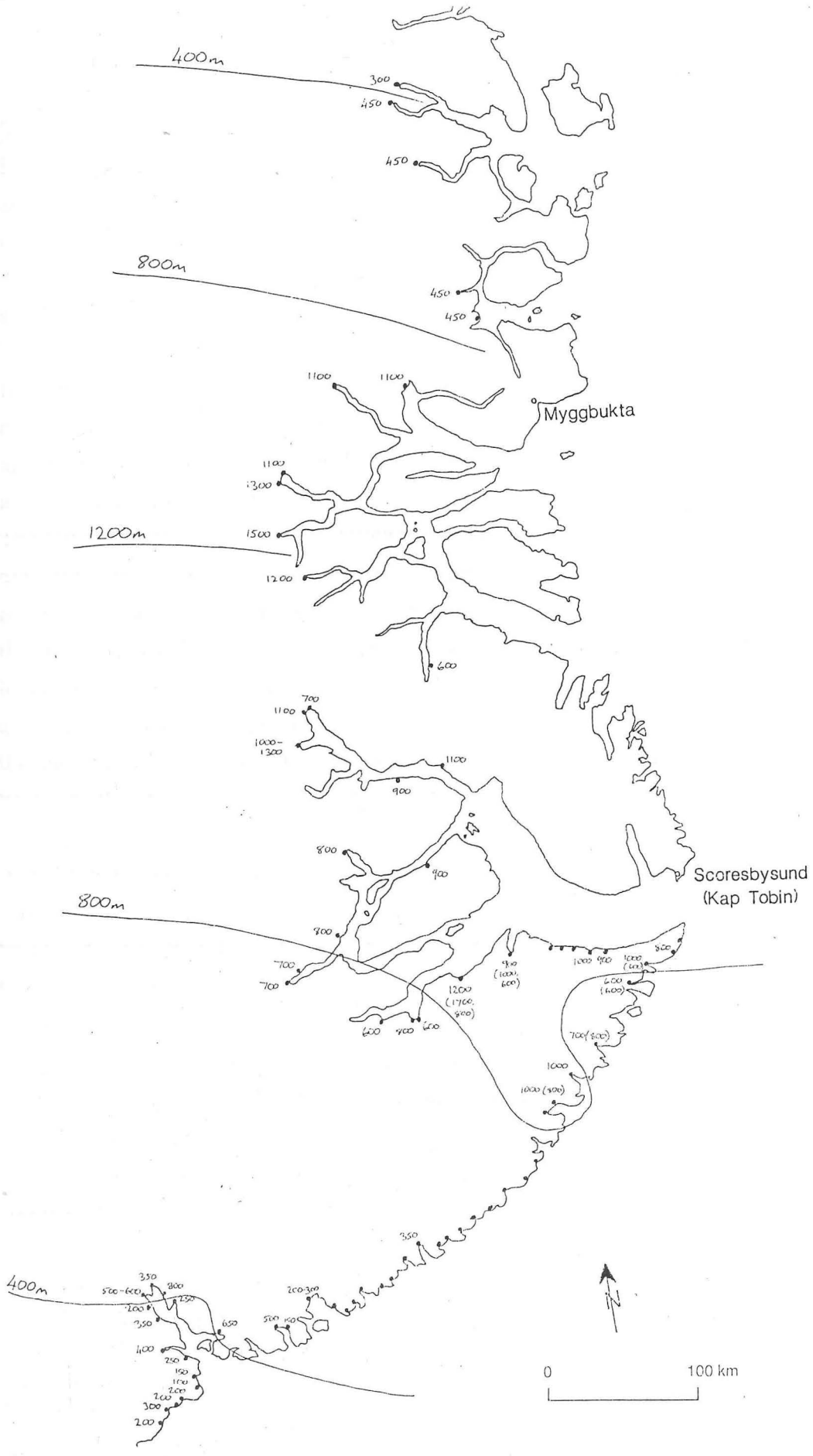

Figure 5.6 Map of study area showing snowline elevations derived from Landsat imagery. Contours indicating trends in elevations are shown (Section 5.4.1), and the locations of two of the weather stations discussed in Section 5.4.2 are marked.

The high snowline elevation for Styrte Gletscher (no. 13) may be related to the fact that it has a steeper terminus than others in the region. Alternatively, this may be because it has a southerly orientation and thus experiences more melting, whereas most of this section of coastline faces west (Fig. 5.6). Frederiksborg and Sorgenfri Gletschers (nos. 15 and 16, Table 5.2) have slightly higher than average snowlines, and their basins are orientated southwards (Fig. 4.4).

Interpreting the drop in snowlines in the far north is more complex, as the snowline elevations were not all interpreted from the same image. It is not clear to what extent the apparent disparity in snowline elevations is due to them having been obtained from scenes acquired on two different dates, although these are only one week apart in the same year. The lower elevations from scene 230/007 could be explained by a late season snowfall, but elevations from another scene acquired further south on the same date (230/009) do not appear to be anomalous (Tables 5.4 and 5.5). It should be noted that the glacier termini in this area are distributed over a distance of several hundred kilometers (Fig. 5.6), and so local climatic conditions may have caused the effects observed. Those glaciers which have a lower snowline are generally closer to the coast (less than 100 km) than those for which the snowlines were higher (100–200 km), so the discontinuity in snowline elevations may be due to the effects of continentality (Fig. 5.6).

For Bredegletscher and Sydbræ, elevations were obtained from dates just two weeks apart (nos. 48 and 49, Table 5.4) and both glaciers show a rise in snowline elevation. This could be an indication that the met season had not ended, and hence the snowline was still rising towards its maximum elevation. Elevations are also available for these two glaciers from 8 September 1989, and these are both substantially lower. This indicates that either the image was acquired after the start of the accumulation season, or the melt season had been interrupted by an early snowfall. Elevation estimates from September 1989 and August 1987 for glaciers no. 36 and 38–40 on the Blosseville Kyst (Table 5.3) show a similar pattern with the September elevations consistently lower than or equal to those from August.

The range of values obtained for Bredegletscher and Sydbræ gives an idea of the uncertainty of the results, with estimates for Sydbræ varying by over 100% (Table 5.4). However, Sydbræ has a very high snowline compared to all others in the immediate area, and should not therefore be considered typical. Much of the variability in the results can be explained due to the fact that the images were not acquired exactly at the end of the balance year, as the snowlines are either still rising due to melting (August 1987), or descending due to snowfall early in the accumulation season (September 1989). The date of the end of the balance year is not necessarily the same over the whole area, as the annual precipitation minimum appears to occur earlier in the year further north (Fig. 5.7).

5.4.2 *Effect of Climate on Snowline Elevations*

A high snowline elevation can indicate either a high surface melt rate (i.e. higher temperatures) or a low precipitation rate. On the west coast of Greenland, the snowline elevation is observed to decrease with increasing latitude (Section 2.1.7), which implies that the temperature has more influence than the precipitation rate, as both generally decrease with latitude. The results from East Greenland, however, show a rising snowline elevation with latitude (Fig. 5.6). Since the temperature decreases northwards along the east coast, as expected (Fig. 5.7), this trend could be explained if the precipitation rate drops off at a faster rate. Figure 5.8 shows the precipitation rates for four stations along the East Greenland coast, averaged over a number of years. The stations are at Angmassalik (Fig. 1.1, 65° 36'N, 37° 38'W), Scoresbysund (Fig. 5.6, 70° 29'N, 21° 58'W), Myggbukta (Fig. 5.6, 73° 30'N, 21° 30'W) and Nord (Fig. 1.1, 81° 36'N, 16° 40'W). It can be seen from Fig. 5.8 that the precipitation rate does drop rapidly with latitude, with the mean annual total for the four stations being 770 mm, 428 mm, 298 mm and 204 mm, respectively (Putnins, 1970). It can also be seen that the maximum precipitation occurs in the winter months in East Greenland, whereas on the north-west coast it occurs in the summer (Putnins, 1970, p. 98). This would lead to lower snowlines in West Greenland at the end of the melt season, and may thus explain the apparently contradictory trends in snowline elevation on the east and west coasts.

Some care must be taken when interpreting the meteorological data, as local orographic effects can have a large influence on temperature and precipitation values at a given weather station. There are insufficient stations in East Greenland to determine to what degree any one station is representative of a region. Also, since the weather stations are all located on the coast, it is not possible to determine the effect of continentality from these data. The interactions between temperature, precipitation, degree of continentality and topo-graphy on a glacier are obviously complex, and have been the subject of several modelling studies (Oerlemans, 1987). Energy balance models have been used to determine the sensitivity of glacier systems to climatic and topographic parameters for the Greenland Ice Sheet (Oerlemans, 1991) and valley glaciers in southern Norway (Oerlemans, 1992). This approach would be useful in identifying which parameters cause the observed trends in snowline elevations.

In conclusion it can be seen that despite the limitations and inaccuracies inherent in determining snowline elevations from Landsat data, the results appear to be consistent. This technique can therefore be used for detecting and monitoring trends in snowline elevation as an indicator of mass balance, although careful examination of meteorological data from around the time of image acquisition is to be recommended.

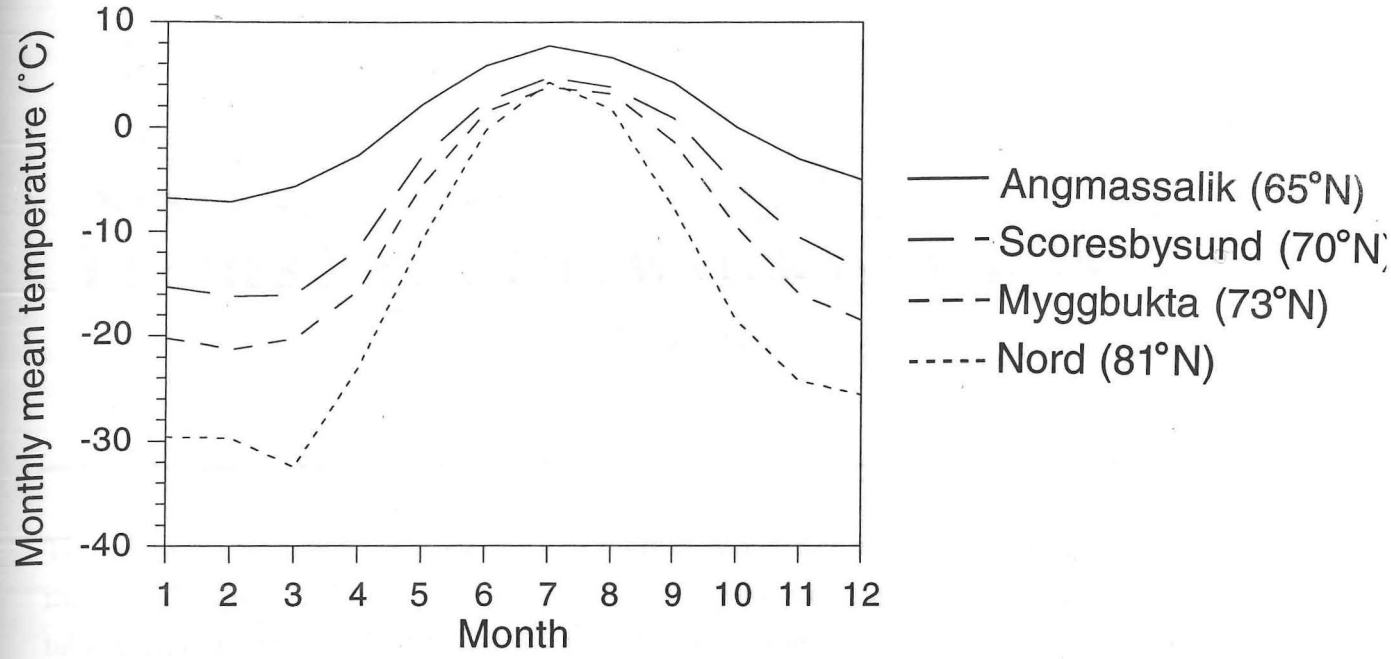

Figure 5.7 Mean monthly temperatures for four stations on the east coast of Greenland. Angmassalik and Nord are shown on Fig. 1.1, and Scoresbysund (Kap Tobin) and Myggbukta are shown on Fig. 5.6. The data are average values over the period 1931 to 1956 (Putnins, 1970, pp. 124-126).

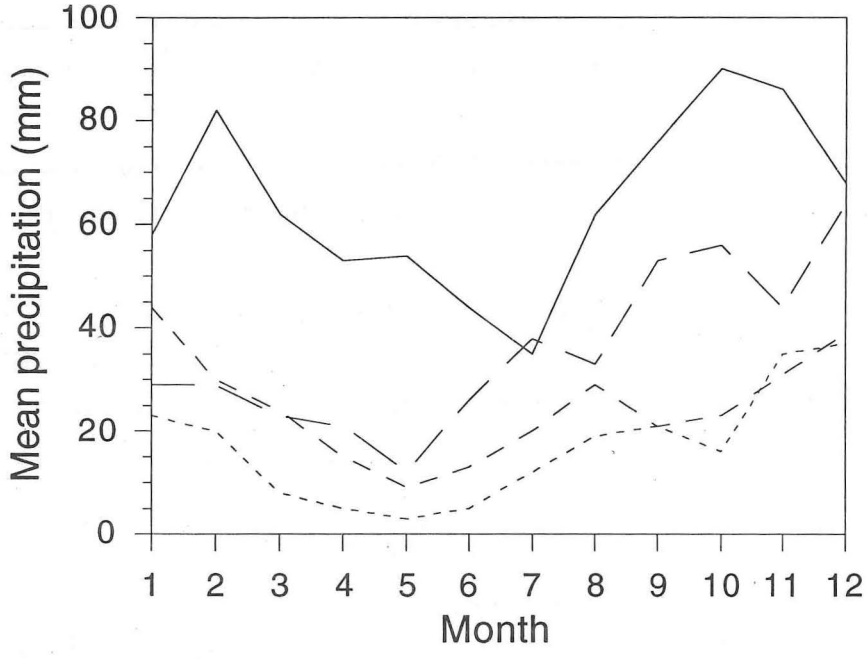

Figure 5.8 Mean monthly precipitation values in mm for four stations on the East Greenland coast. Stations are as for Fig. 5.7 above.

Chapter 6

Suspended Sediments in Meltwater Plumes From Tidewater Glaciers in East Greenland

This chapter presents a brief overview of current knowledge about the glacimarine sediments in the fjords and on the continental shelf off East Greenland. The application of digital Landsat imagery to identify suspended sediment plumes is discussed, and some examples from East Greenland are presented. The possibility of determining a correlation between drainage basin area, as determined in Chapter 4, and suspended sediment production is discussed.

6.1 INTRODUCTION

Plumes of turbid meltwater are often present in glacially influenced marine environments, and derive from either subglacial meltwater streams exiting tidewater glaciers or from subaerial glacier-fed streams. Despite their sediment load, these freshwater plumes have a lower density than the saline fjord water, and are thus buoyant and upwell to the water surface (Powell, 1990). The fact that a plume is present at the terminus of a tidewater glacier indicates that at least part of the bed is undergoing basal melting, and this in turn has implications for the thermal and dynamic regime of the glacier.

As the buoyant, turbid plume rises and spreads away from the source (Fig. 6.1), its debris load is gradually deposited, due to the decreasing flow velocity and hence decreasing capacity of the plume to transport sediment. Suspended sediment concentration (SSC) therefore decreases with distance from the source (the glacier terminus or the mouth of the stream). This is confirmed by field measurements of suspended sediment concentrations in fjords adjacent to tidewater glaciers and/or subaerial streams (Elverhøi *et al.*, 1983; Syvitski *et al.*, 1987). Studies by Sharma (1979) (reproduced in Syvitski *et al.* 1987, p.124) in Port Valdez, Alaska show surface SSCs of about 400 mg l^{-1} immediately offshore of a subaerial meltwater stream, and about 200 mg l^{-1} adjacent to a tidewater glacier terminus, both decreasing with distance from source to about 5 mg l^{-1} at the mouth of the fjord about 10 km distant. The average grain size of the deposited sediment also decreases with

distance from the source, as the coarser sediments have a higher fall velocity and are thus deposited more readily.

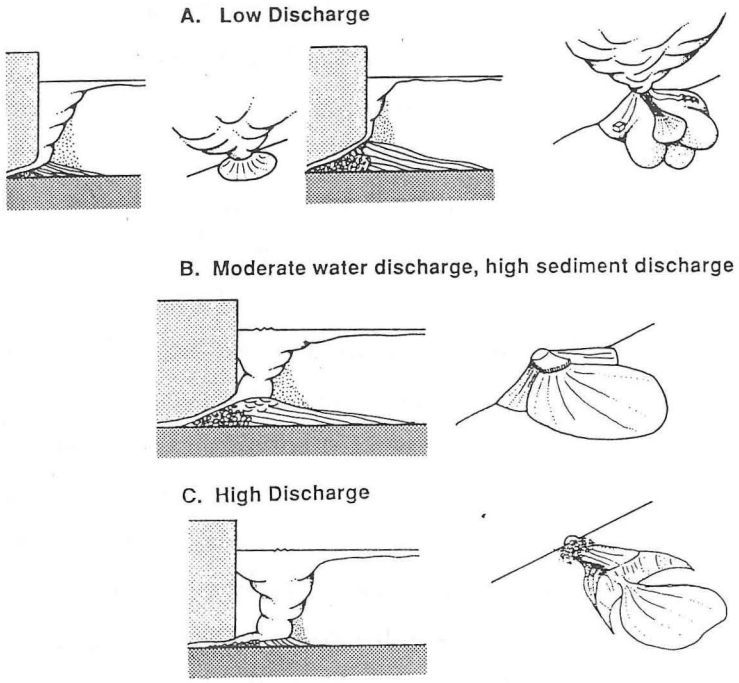

Figure 6.1 Illustration of several types of subglacial meltwater plume, showing buoyant upwelling and deposition of debris (Powell, 1990).

The position and size of a plume varies with time according to the tides, winds and discharge rates of the meltwater stream (Dowdeswell & Cromack, 1991). The stream discharge would be expected to fluctuate diurnally and seasonally as the temperature oscillates, but this effect may be damped if the water is stored in a lake or englacial reservoir before reaching the fjord.

Sediment accumulation rates, which are important for the interpretation of the marine geological record, have been derived for many areas, and vary widely, for example from 0.15 mm yr^{-1} for Igaliko Fjord in south-west Greenland to several thousand mm yr^{-1} for Muir Inlet, Alaska (Syvitski *et al.*, 1987, p.137). The proportion of this accumulation which is due to turbid meltwater plumes, as opposed to iceberg rafting, varies with climate (Dowdeswell & Dowdeswell, 1989). In general, iceberg rafting is more significant in colder regions as the production of meltwater decreases and a greater proportion of mass loss is by iceberg calving. Ice shelves are an exception to this trend, as they have often deposited much of their debris load before calving, due to basal melting close to the grounding line (Jenkins & Doake, 1991).

6.2 GLACIMARINE PROCESSES AND SEDIMENTS IN EAST GREENLAND

The bedrock beneath the outlet glaciers of the Greenland Ice Sheet is eroded by glacier movement, and the resulting debris is eventually deposited in the fjords and on the adjacent continental shelf. These sediments form a record of the fluctuations in the extent of the Ice Sheet through the Late Quaternary, and of the palaeocurrent patterns of the North Atlantic. As such, they provide a valuable proxy climate record which can give an insight into the present and possible future behaviour of the Greenland Ice Sheet in particular and the North Atlantic climate in general. A European Science Foundation programme known as PONAM (Polar North Atlantic Margins: Late Cenozoic Evolution) is currently working to reconstruct the environmental history of the continental margin of East Greenland by studying both the terrestrial evidence, and the marine evidence recorded in sediment cores (Möller *et al.*, 1991). To interpret the record in these cores, it is first necessary to understand the processes which gave rise to the features observed within them, which is achieved by comparison with modern analogues. The processes currently active in the polar regions have, in earlier times, produced sedimentary rocks found in many temperate regions today (Anderson, 1983). Identifying the present day sources of sediments and processes of sedimentation in East Greenland is therefore of interest for several reasons.

Glacimarine sediments, defined as debris deposited in the marine environment from grounded or floating glacier ice (Andrews & Matsch, 1983; Powell, 1984), can be transported from land to the marine environment by any of several processes, as illustrated in Figure 6.2 (Dowdeswell, 1987).

6.3 ANALYSIS OF SUSPENDED SEDIMENTS USING DIGITAL LANDSAT IMAGERY

6.3.1 Review of Previous Studies

It has been demonstrated in several studies that digital Landsat imagery can be used to detect near-surface suspended sediments (Ritchie *et al.*, 1976; Aranuvachapun & LeBlond, 1981; Lindell *et al.*, 1985; Curran & Novo, 1988) as well as chlorophyll concentrations and other water quality parameters (Alföldi & Munday, 1978; Verdin, 1985; Ekstrand, 1992). The presence of suspended sediments causes a increased reflectance in the blue part of the spectrum at about 0.6 μm (Sydor, 1980), and thus is most clearly visible in band 1 (Section 3.1). Quantitative assessment of suspended sediment concentration (SSC) remains a significant problem, however, as the grain size and colour of the sediment have a large influence on the spectral radiance of the near-surface water (Sydor, 1980).

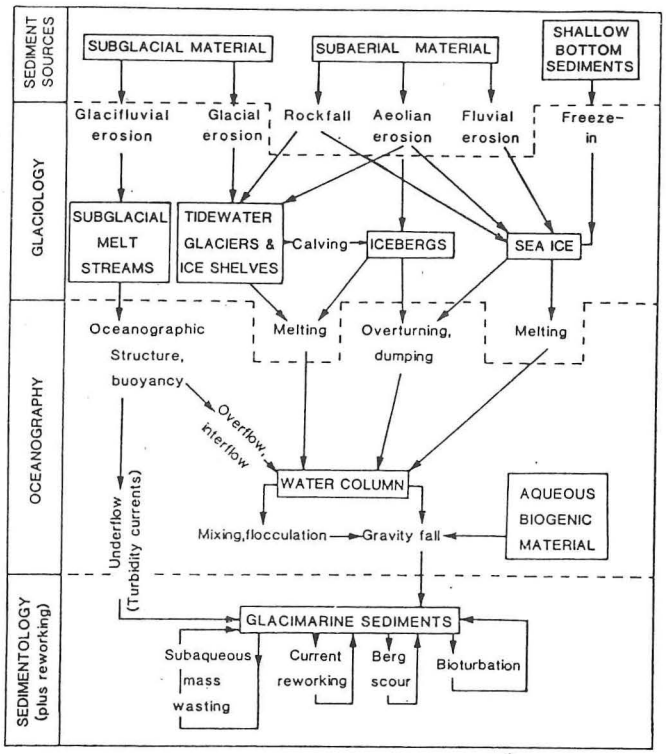

Figure 6.2 Summary of the main sources and processes of glacimarine sedimentation (from Dowdeswell, 1987).

Correlations between remotely sensed spectral radiance and measured SSC or turbidity have been derived for individual sites such as coastal waters (Aranuvachapun & LeBlond, 1981), lakes (Ritchie *et al.*, 1987; Ritchie & Cooper, 1988), reservoirs (Ritchie *et al.*, 1976) and estuaries (Froidefond *et al.*, 1993) using Landsat or other satellite data. These correlations are generally good for each individual site, but show wide variation between sites (Curran & Novo, 1988) indicating that field data are necessary to calibrate remotely sensed data at individual sites.

It should be noted that field measurements of SSC also suffer limitations, in that samples are usually few, widely spaced and non-synchronous. Such samples may not necessarily give representative values, as SSCs often have a high degree of spatial variability (Dowdeswell & Cromack, 1991) and vary considerably with depth. Remotely sensed data can thus be more appropriate where a synoptic value is required.

Several authors have noted the importance of applying a correction for solar elevation and atmospheric haze, such as the method described in Chapter 3, before attempting to infer quantitative values of SSC from satellite imagery (Sydor, 1980; Verdin, 1985). These corrections are also necessary for accurate scene-to-scene comparison, even when absolute values are not required, as the change in reflectance value caused by a change in SSC is only slight, and could easily be obscured by noise due to haze and solar elevation.

In areas where suspended sediments and phytoplankton are both present in significant quantities, it can be difficult to determine the concentration of each separately using remotely sensed data (Ekstrand, 1992). However, it is generally possible to identify the cause of a plume seen on Landsat imagery due to the different spectral responses of sediment and pigment (Cracknell, 1981, Table 11.5). In the polar regions, an additional complication is the presence of sub-pixel scale sea ice and icebergs. Being predominantly white, however, ice exhibits a fairly uniform reflectance across the visible spectrum, whereas suspended sediment shows a greater reflectance in band 1 (0.5 to 0.6 μm), decreasing towards band 4.

6.3.2 *Examples from East Greenland*

Figure 6.3 shows a section of a digitally enhanced band 1 image (scene 230/010 acquired on 22 August 1987, Fig. 11, Appendix 1) of the mouth of a river draining a glacierized basin at the head of Fønfjord, in the Scoresby Sund fjord system (Fig. 1.2). Figure 6.4 shows two views of the same area taken from a helicopter in September 1990 from a height of approximately 1000 m. The satellite image shows a plume which is similar in character and extent to the sediment plume seen in the photographs, indicating that the band 1 sensor is able to detect the presence of suspended sediment.

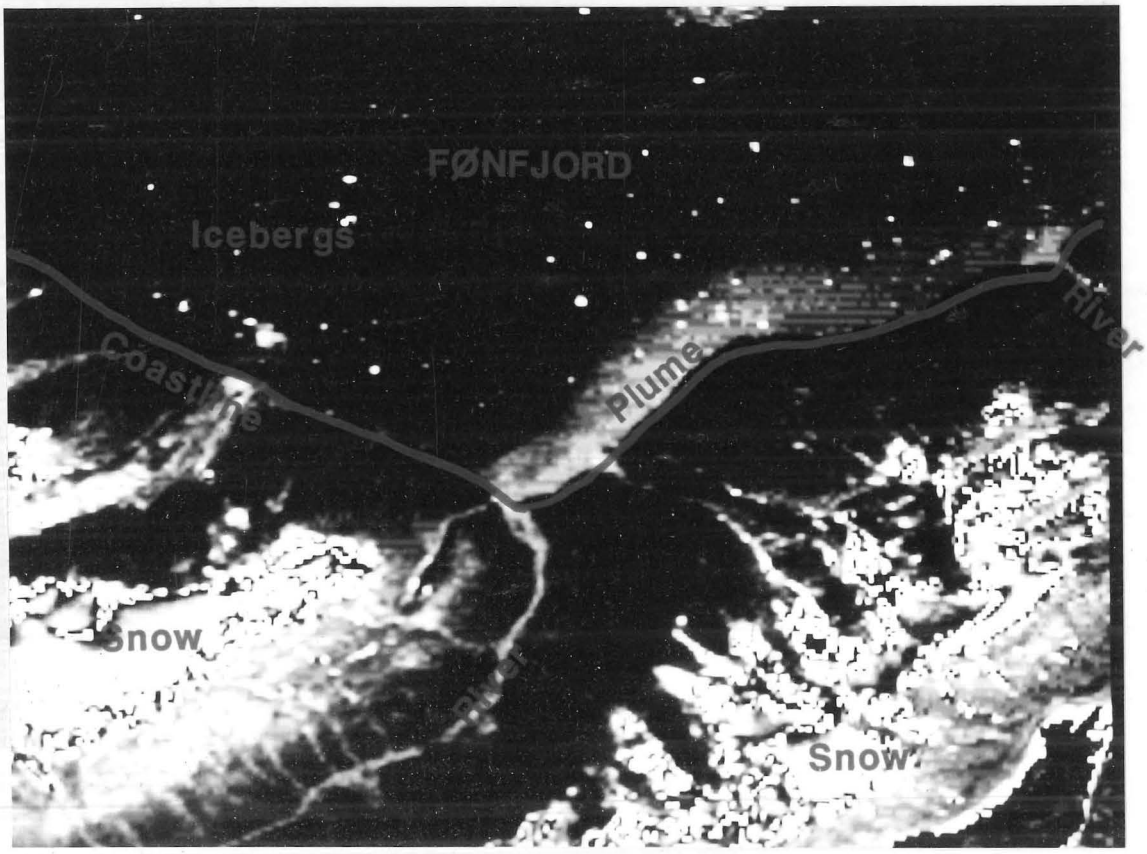

Figure 6.3 Digitally enhanced Band 1 image (230/010) of a plume originating at the mouth of a river at the head of Fønfjord, in the Scoresby Sund fjord system.

In areas where suspended sediments and phytoplankton are both present in significant quantities, it can be difficult to determine the concentration of each separately using remotely sensed data (Ekstrand, 1992). However, it is generally possible to identify the cause of a plume seen on Landsat imagery due to the different spectral responses of sediment and pigment (Cracknell, 1981, Table 11.5). In the polar regions, an additional complication is the presence of sub-pixel scale sea ice and icebergs. Being predominantly white, however, ice exhibits a fairly uniform reflectance across the visible spectrum, whereas suspended sediment shows a greater reflectance in band 1 (0.5 to 0.6 μm), decreasing towards band 4.

6.3.2 Examples from East Greenland

Figure 6.3 shows a section of a digitally enhanced band 1 image (scene 230/010 acquired on 22 August 1987, Fig. 11, Appendix 1) of the mouth of a river draining a glacierized basin at the head of Fønfjord, in the Scoresby Sund fjord system (Fig. 1.2). Figure 6.4 shows two views of the same area taken from a helicopter in September 1990 from a height of approximately 1000 m. The satellite image shows a plume which is similar in character and extent to the sediment plume seen in the photographs, indicating that the band 1 sensor is able to detect the presence of suspended sediment.

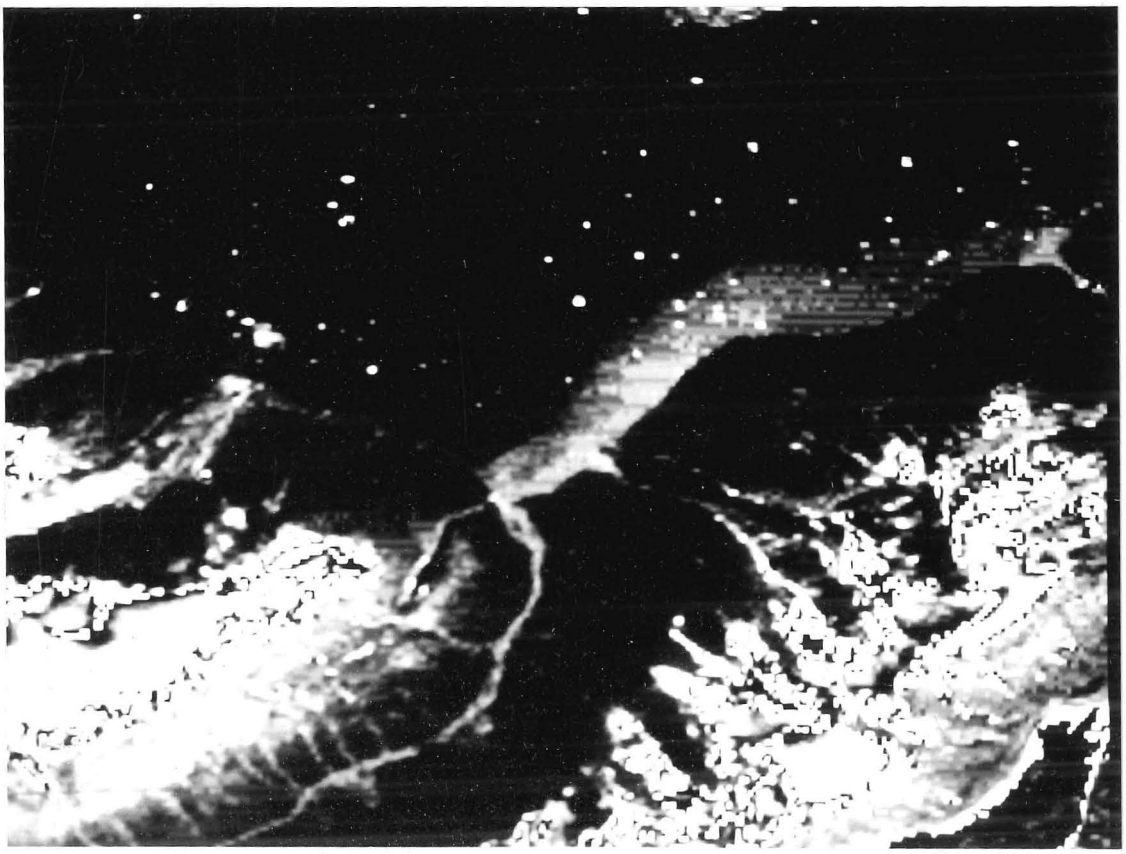

Figure 6.3 Digitally enhanced Band 1 image (230/010) of a plume originating at the mouth of a river at the head of Fønfjord, in the Scoresby Sund fjord system.

Figure 6.4 Two views of the same river mouth as seen in Fig. 6.3, showing suspended sediment plumes (photographs courtesy of Julian Dowdeswell).

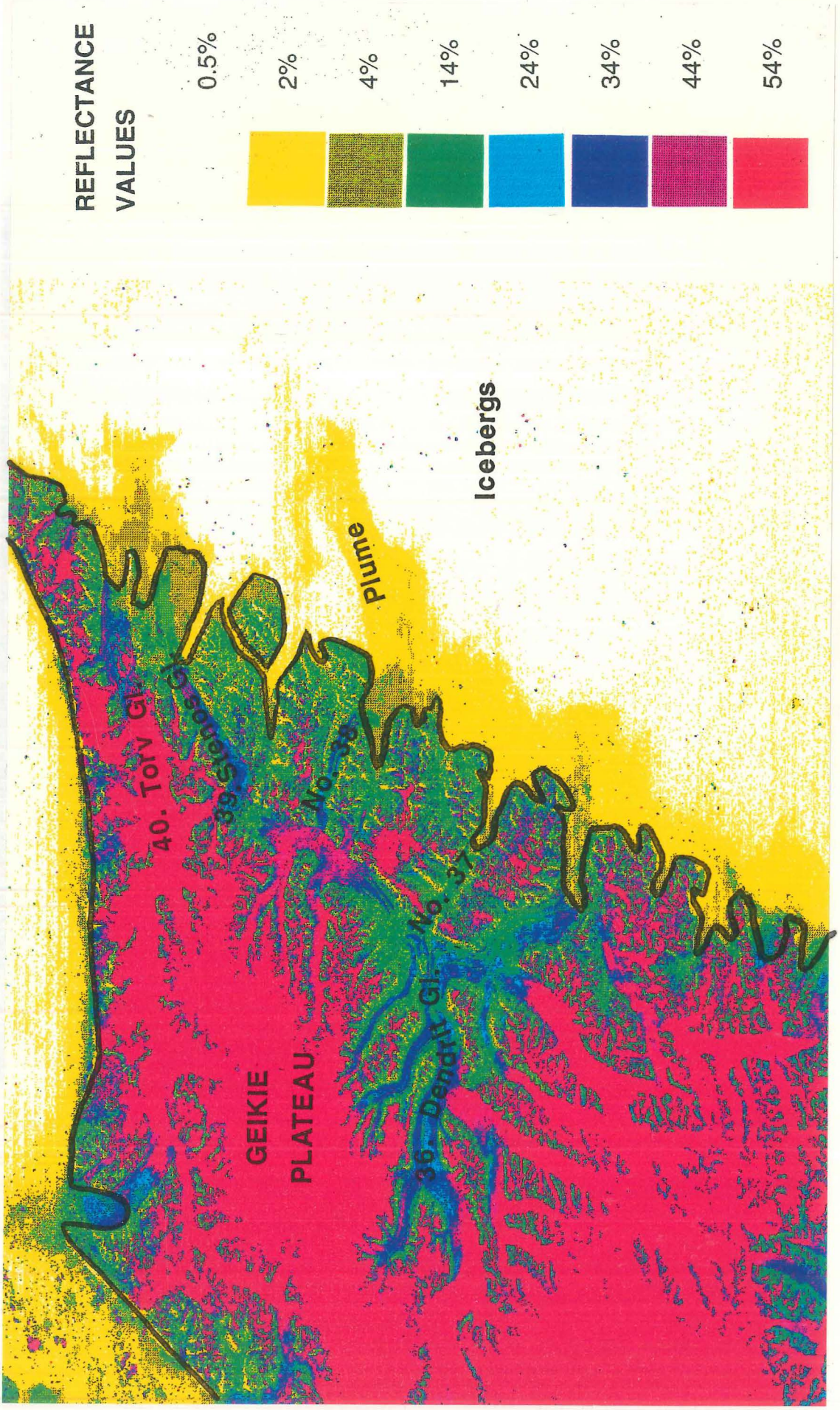

Figure 6.5 Scene 226/011, band 1 of the Geikie Plateau and Blosseville Kyst region acquired on 10 August 1987, showing extensive sediment plume. The area shown is a full scene (185 km by 185 km). Band 4 of the same image is shown in Fig. 4, Appendix 1.

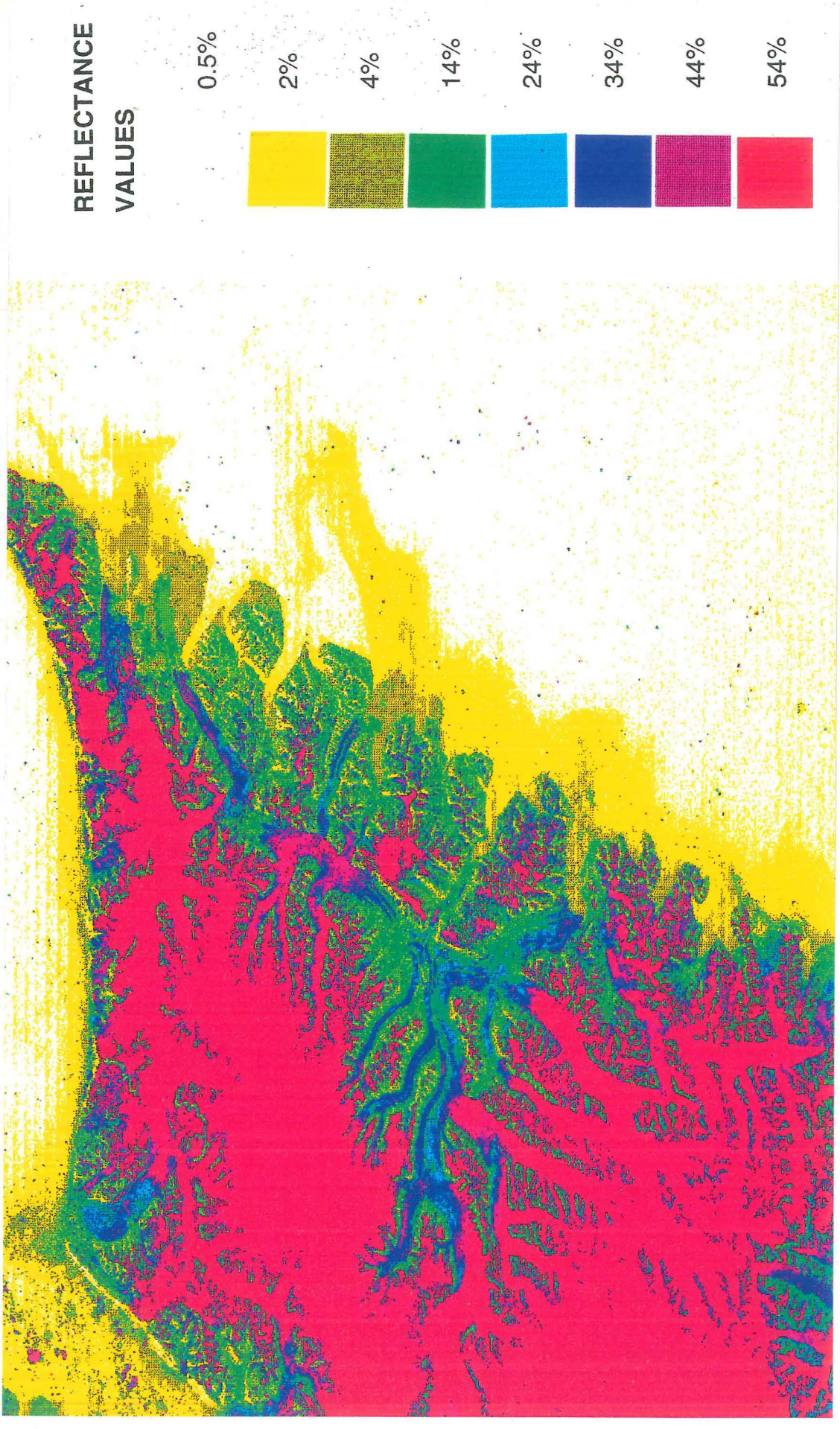

Figure 6.5 Scene 226/011, band 1 of the Geikie Plateau and Blosseville Kyst region acquired on 10 August 1987, showing extensive sediment plume. The area shown is a full scene (185 km by 185 km). Band 4 of the same image is shown in Fig. 4, Appendix 1.

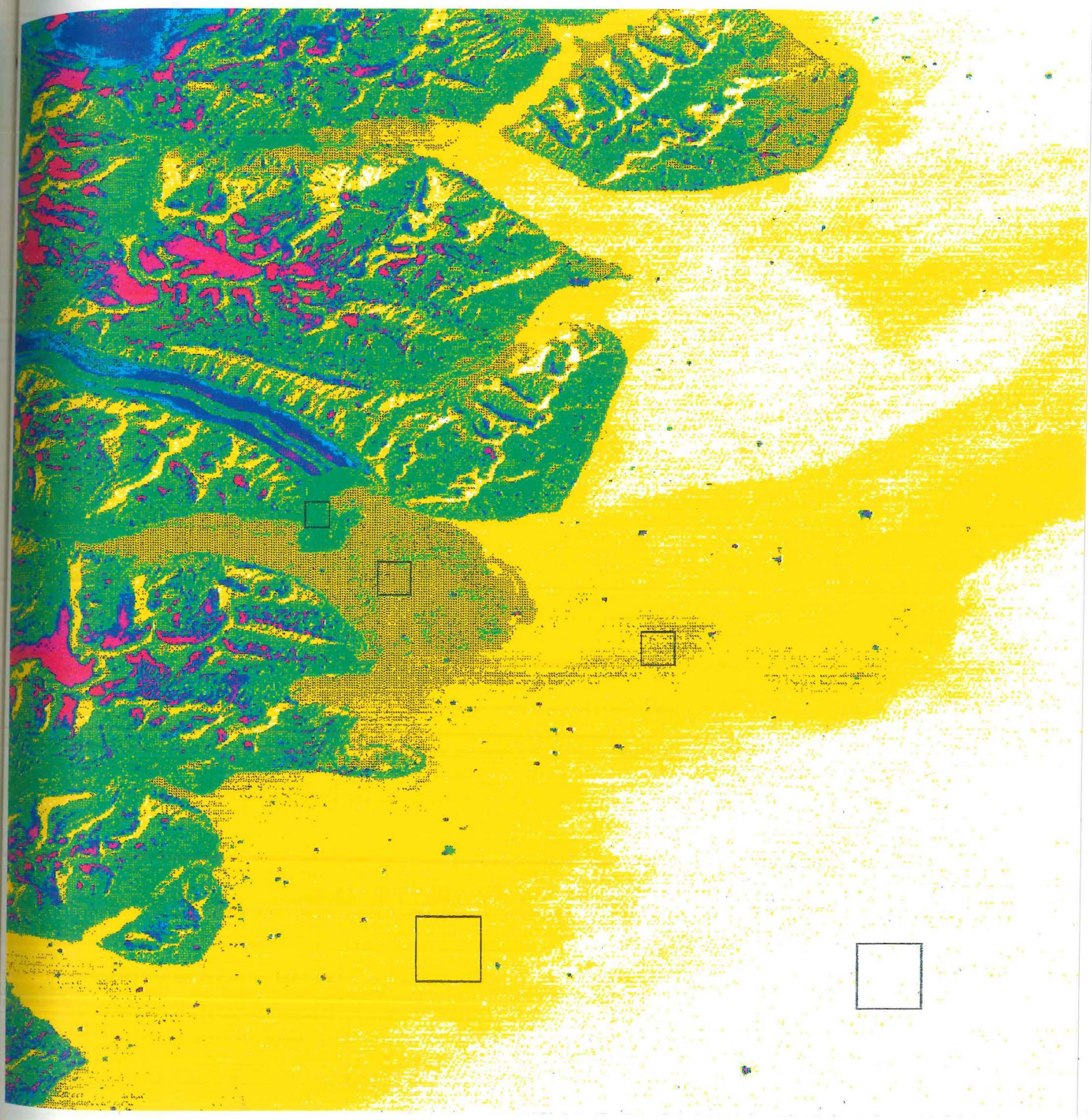

Figure 6.6 Portion of scene 226/011 of 10th August 1987 showing details of sediment plume. Boxes indicate test areas selected for analysis of reflectance values (Section 6.3.2).

Figure 6.5 is a full scene (185 by 185 km) band 1 image (scene 226/011) acquired on 10 August 1987, covering the Blosseville Kyst and the Geikie Plateau (Fig. 1.2 and Fig. 4, Appendix 1). A zone of relatively higher reflectance, assumed to be due to the presence of suspended sediments, is visible along most of the coastline, with a plume extending about 70 km offshore. The darker, coloured dots are icebergs, with a much higher reflectance than the surrounding water, which has a reflectance of almost zero.

Figure 6.6 shows an enlarged portion of the same scene covering an area of approximately 60 km across by 70 km. It appears from this figure that the plume originates mainly from the terminus of glacier no. 38, since the reflectance values of the water decrease with distance from the terminus. Five test locations were selected, as marked by black boxes on Figure 6.6, with areas of either 18 by 18 pixels, 24 by 24 pixels or 48 by 48 pixels. Multiples of six pixels were chosen to give an average over the possible striping effect due to varying gain of the six detectors (Section 3.3.2). Histograms of reflectance were plotted for each area as shown in figure 6.7. It is clear from the figure that each colour observed on the image represents one or two percentage classes of reflectance, with little overlap. It should therefore be possible to map out the areas corresponding to each reflectance class, and thus make comparisons between different regions in terms of relative production of suspended sediments, although the effects of grain size and sediment colour on reflectance must also be considered.

A second scene was acquired for the same path and row on 8 September 1989 (Fig. 3, Appendix 1), but there is no extensive plume apparent on this scene. This may be due to it having being acquired later in the year, and hence the discharge of meltwater is likely to be reduced.

6.4 IMPLICATIONS OF PRESENCE AND DISTRIBUTION OF TURBID MELTWATER PLUMES

6.4.1 Glaciological Implications

Studies in Svalbard have shown a correlation between the presence of turbid meltwater plumes and the temperature and flow regimes of the parent glacier (Dowdeswell, 1984). Along 130 km of ice cliffs bordering Austfonna on Nordaustlandet, Svalbard, major meltwater plumes originating from subglacial drainage streams were observed every few kilometers, except along the 30 km front of Bråsvellbreen. This basin is currently in the quiescent phase of a surge cycle, and is substantially thinner than the theoretically predicted equilibrium profile, whereas the other basins along this ice cliff are not known to have surged and are much thicker (Dowdeswell, 1986a). Since the ice is thin (100–150 m), the bed is unlikely to reach the pressure melting point.

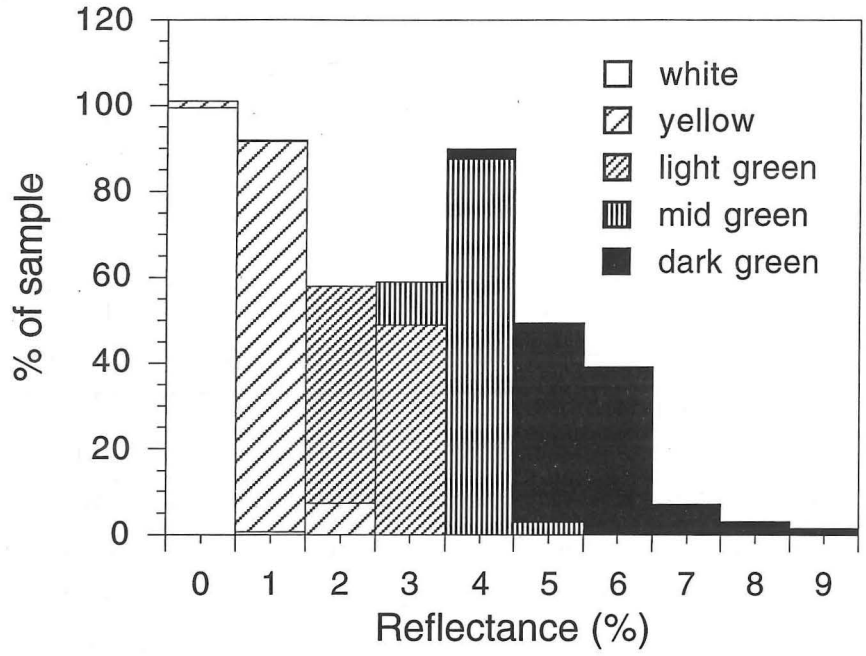

Figure 6.7 Histogram showing band 1 reflectance values for each of the five test areas indicated by boxes on Fig. 6.6 (Section 6.3.2).

This conclusion is supported by measured temperatures at 10 m depth which were reported to be –8°C, and so the glacier is likely to be frozen to its bed. Thus it seems clear that the presence of sediment plumes is an indication of the temperature and flow regime of the parent glacier.

Turbid meltwater plumes only occur where at least part of the bed is at or above the pressure melting point. It could therefore be expected that a transect from south to north along the East Greenland coast would show a cutoff point beyond which meltwater plumes are not observed, and thus indicate the latitude north of which all glaciers are frozen to their beds. Drainage basin area is also likely to have an influence on the quantity of sediment produced. If a correlation could be found between drainge basin area (or ratio of basin area to terminus width, Chapter 4) and the extent of the turbid meltwater plumes, this effect could be corrected for when looking for a latitudinal gradient in suspended sediment production.

6.4.2 Implications for Marine Geology

As discussed in Section 6.1, the relative importance of deposition from turbid meltwater plumes as opposed to iceberg rafting depends on climatic factors and could therefore be expected to vary with latitude. The east coast of Greenland represents a continuous transect from sub-polar to polar climates across a wide latitudinal range, and an investigation of turbid meltwater production in this region could therefore be useful in determining the relationship between latitude and the nature of the sediment source.

If the glacimarine environments of the world are considered as representing a spectrum of climatic settings, from the cold, dry high latitude areas of the Antarctic to the warmer, wetter region of South-East Alaska, then East Greenland represents a considerable portion of the spectrum. In South-East Alaska, large quantities of meltwater are produced due to the relatively warm air and sea surface temperatures, and almost all sediment originates from meltwater plumes (Powell & Molnia, 1989), whereas studies in Svalbard show that about 10% is due to iceberg rafting (Dowdeswell & Dowdeswell, 1989). Recent investigations in Scoresby Sund show that iceberg rafting is predominant in this region, accounting for about 90% of the accumulation (Dowdeswell *et al.*, in press). Further studies of the distribution of turbid meltwater plumes and the rates of iceberg production in East Greenland could extend this transect of data points northwards.

Chapter 7

CONCLUSIONS

7.1 SUMMARY

The main conclusion of this study is that a great deal of useful glaciological information can be obtained using digital Landsat MSS data. The results of the investigations into the glaciology of East Greenland described in this thesis can be summarized as follows:

- the haze correction technique, whereby the radiance value of clear, open water for each band is subtracted from the total radiance, was successful. Reflectance values obtained by independently correcting two overlapping scenes acquired two days apart were shown to be consistent by comparing reflectance values from four test areas on each scene. It can be concluded that this method can be used for correction of any scenes where sufficient clear, open water is present.

- the distribution of drainage basins within the study area was successfully determined using MSS band 4 data. A relatively high degree of accuracy was possible for most of the ice divides since the band 4 data revealed detailed and subtle surface flow features. This technique is particularly suitable for areas, such as the Geikie Plateau, where the scale of the topography makes radar altimetry inadequate due to its poorer spatial resolution.

- the comparison of basin areas and terminus widths showed that the tidewater glaciers of this area exhibit a wide range of flow regimes. The glaciers with the largest basins do not have the widest termini, and thus undergo strongly convergent flow and have high terminus velocities. Christian IV Gletscher was seen to be anomalous for the region, as it has the widest terminus of all glaciers in the study region (15 km), but only an intermediate basin area. The ice cap of the Geikie Plateau is independent of the Greenland Ice Sheet, and drains almost entirely via the glaciers of the Blosseville Kyst.

- the snowline elevations, as determined from digital reflectance profiles, appear to rise northwards along the East Greenland coast from about 200 m near Kangerdlugssuaq to over 1000 m in Kejser Franz Josef Fjord. This is in contrast to the reported trend for West Greenland, possibly due to the precipitation rate decreasing more rapidly with latitude on

the east coast than on the west coast. Comparison of snowlines derived from overlapping imagery shows that the results are consistent, and thus the trend in elevations is probably real, rather than an artefact of the data.

- turbid meltwater plumes are apparent on MSS band 1 data, which can therefore be used to determine the sources and distribution of suspended sediments in glacimarine environments.

7.2 FURTHER WORK

The atmospheric haze correction procedure described in Chapter 3 could be further verified by repeating the scene-to-scene comparison for other overlapping scenes. The spatial variabilty of haze values could be estimated from scenes acquired on the same day in order to assess the feasibility of extrapolating haze correction values from one scene to another, for example from the coast to the interior, where no open water is present.

Further work could be undertaken to correlate the drainage basin areas, and the basin area to terminus width ratios as determined in Chapter 4 to other factors, e.g. snowline elevations, turbid meltwater and iceberg production, and indications of possible surge-type behaviour.

A time series of images of the same scene for the period around the end of the melt season would reveal the exact date of the end of the season, and also the rate of snowline retreat which could be expected. A series of images acquired on the same date, or as close as possible thereto, would reveal any spatial trends in snowline elevations without having the uncertainty of the effect of different dates of acquisition. If detailed meteorological data can be obtained for the months in which the imagery was acquired, then the hypotheses which were proposed in Chapter 5 regarding the date of the end of the melt season, and the interruption of the melt season by snowfall could be tested. The influence on the snowline elevations of factors such as number of days of positive mean temperatures, and the amount and distribution of precipitation could also be investigated.

Systematic investigation of the extent and distribution of turbid meltwater plumes along the coast of East Greenland could be carried out to determine the extent of basal melting, and the latitude beyond which it no longer occurs.

REFERENCES

Alföldi, T.T. & Munday, J.C. 1978. Water quality analysis by digital chromaticity mapping of Landsat data. *Canadian Journal of Remote Sensing* 4, 2, 108-126.

Anderson, J.B. 1983. Ancient glacial marine deposits: their spatial and temporal distribution. In B.F. Molnia (Ed.), *Glacial-Marine Sedimentation.* (3-92). Plenum Press, New York.

Andrews, J.T. & Matsch, C.L. 1983. *Glacial marine sediments and sedimentation: an annotated bibliography* . Geo Abstracts Ltd., Norwich.

Aoki, T. 1991. A multiple scattering model for the atmosphere-snow system. In S. Kawaguchi (Ed.), *14th Symposium on Polar Meteorology and Glaciology.* Tokyo: National Institute of Polar Research.

Aranuvachapun, S. & LeBlond, P.H. 1981. Turbidity of coastal water determined from Landsat. *Remote Sensing of Environment* 84, 113-132.

Benson, C.S. 1962. *Stratigraphic studies in the snow and firn of the Greenland Ice Sheet,* Research Report No. 70, U.S. Army Snow Ice and Permafrost Research Establishment.

Bindschadler, R.A., Zwally, H.J., Major, J.A. & Brenner, A.C. 1989. *Surface Topography of the Greenland Ice Sheet from Satellite Radar Altimetry* . NASA, Washington DC.

Braithwaite, R.J. 1980. *Regional model of ablation in West Greenland,* Report No. 98, Grønlands Geologiske Undersøgelse.

Braithwaite, R.J. 1984. Can the mass balance of a glacier be estimated from its equilibrium-line altitude? *Journal of Glaciology* 30, 106, 364-368.

Braithwaite, R.J. & Thomsen, H.H. 1984. *Runoff conditions at Paakitsup Akuliarusersua, Jakobshavn, estimated by modelling,* Gletscher-hydrologiske Meddelelser No. 84/3, Grønlands Geologiske Undersøgelse.

Budd, W.F., Jacka, T.H., Jenssen, D., Radok, U. & Young, N.W. 1982. *Derived physical characteristics of the Greenland ice sheet,* No. 23, University of Melbourne Meteorology Department.

Crabtree, R.D. & Doake, C.S.M. 1980. Flow lines on Antarctic ice shelves. *Polar Record* 20, 124, 31-37.

Cracknell, A.P. 1981. *Remote Sensing in Meteorology, Oceanography and Hydrology* . Ellis Horwood Limited, Chichester.

Curran, P.J. & Novo, E.M.M. 1988. The relationship between suspended sediment concentration and remotely sensed spectral radiance: a review. *Journal of Coastal Research* 4, 3, 351-368.

Dansgaard, W., Clausen, H.B., Gundestrup, N., Johnsen, S.J. & Rygner, C. 1985. Dating and climatic interpretation of two deep Greenland ice cores. In C.C. Langway, H. Oeschger, & W. Dansgaard (Ed.), *Greenland Ice Core: Geophysics, Geochemistry, and the Environment.* American Geophysical Union, Washington D.C.

Douglas, B.C., Cheney, R.E., Miller, L., Agreen, R.W., Carter, W.E. & Robertson, D.S. 1990. Greenland Ice Sheet: is it growing or shrinking?*Science* 248, 4953, 288.

Dowdeswell, J.A. 1984. *Remote Sensing Studies of Svalbard Glaciers.* Unpublished PhD thesis, University of Cambridge.

Dowdeswell, J.A. 1986a. Drainage-basin characteristics of Nordaustlandet ice caps, Svalbard. *Journal of Glaciology* 32, 110, 31-38.

Dowdeswell, J.A. 1986b. Remote sensing of ice cap outlet glacier fluctuations on Nordaustlandet, Svalbard. *Polar Research* 4 n.s., 1, 25-32.

Dowdeswell, J.A. 1987. Processes of glacimarine sedimentation. *Progress in Physical Geography* 11, 52-90.

Dowdeswell, J.A. & Cromack, M. 1991. Behavior of a glacier-derived suspended sediment plume in a small Arctic inlet. *Journal of Geology* 99, 111-123.

Dowdeswell, J.A. & Dowdeswell, E.K. 1989. Debris in icebergs and rates of glaci-marine sedimentation: observations from Spitsbergen and a simple model. *Journal of Geology* 97, 221-231.

Dowdeswell, J.A. & McIntyre, N.F. 1986. The saturation of Landsat MSS detectors over large ice masses. *International Journal of Remote Sensing* 7, 1, 151-164.

Dowdeswell, J.A. & McIntyre, N.F. 1987. The surface topography of large ice masses from Landsat imagery. *Journal of Glaciology* 33, 113, 16-23.

Dowdeswell, J.A., Villinger, H., Whittington, R.J. & Marienfeld, P. 1991. The Quaternary marine record in the Scoresby Sund fjord system, East Greenland: preliminary results and interpretation. In P. Moller, C. Hjort, & O. Ingolfsson (Ed.), *The last glacial-interglacial cycle: preliminary report on the PONAM fieldwork in Jameson Land and Scoresby Sund, East Greenland*, Lundqua report 33 (149-155). Skanor, Sweden: Lund University Department of Quaternary Geology.

Dowdeswell, J.A., Whittington, R.J. & Hodgkins, R. 1992. The sizes, frequencies and freeboards of East Greenland icebergs observed using ship radar and sextant. *Journal of Geophysical Research* 97, C3, 3515-3528.

Dowdeswell, J.A., Whittington, R.J. & Marienfeld, P. (in press). The origin of massive diamicton facies by iceberg rafting and scouring, Scoresby Sund, East Greenland.

Duffett-Smith, P. 1990. *Astronomy With Your Personal Computer* (2nd ed.). Cambridge University Press, Cambridge.

Echelmeyer, K., Clarke, T.S. & Harrison, W.D. 1991. Surficial glaciology of Jakobshavns Isbræ, West Greenland: part I. Surface morphology. *Journal of Glaciology* 37, 127, 368-382.

Echelmeyer, K., Harrison, W.D., Clarke, T.S. & Benson, C. 1992. Surficial glaciology of Jakobshavns Isbræ, West Greenland: part II. Ablation, accumulation and temperature. *Journal of Glaciology* 38, 128, 169-181.

Ekstrand, S. 1992. Landsat TM based quantification of chlorophyll-a during algae blooms in coastal waters. *International Journal of Remote Sensing* 13, 10, 1913-1926.

Elverhøi, A., Lønne, Ø. & Seland, R. 1983. Glaciomarine sedimentation in a modern fjord environment, Spitsbergen. *Polar Research* 1 n.s., 127-149.

Escher, A. & Watt, W.S. 1976. Summary of the geology of Greenland. In A. Escher & W.S. Watt (Ed.), *Geology of Greenland.* Grønlands Geologiske Undersøgelse, Copenhagen.

Espizua, L.E. & Bengochea, J.D. 1990. Surge of Grande del Nevado glacier (Mendoza, Agentina) in 1984: its evolution through satellite images. *Geografiska Annaler* 72A, 3-4, 255-259.

Froidefond, J.M., Castaing, P., Jouanneau, J.M., Prud'homme, R. & Dinet, A. 1993. Method for the quantification of suspended sediments from AVHRR NOAA-11 satellite data. *International Journal of Remote Sensing* 14, 5, 885-894.

Funder, S. 1989. Quaternary geology of the ice-free areas and adjacent shelves of Greenland. In R.J. Fulton (Ed.), *Quaternary Geology of Canada and Greenland.* Geological Survey of Canada also Geological Society of America.

Funder, S. & Hjort, C. 1973. Aspects of the Weichselian chronology in central East Greenland. *Boreas* 2, 2, 69-84.

Gruell, W. & Oerlemans, J. 1987. The evolution of the englacial temperature distribution in the superimposed ice zone of a polar ice cap during a summer season. In J. Oerlemans (Ed.), *Symposium on Glacier Fluctuations and Climatic Change*, (289-303). Amsterdam: Kluwer Academic Publishers.

Hall, D.K., Bindschadler, R.A., Foster, J.L., Chang, A.T.C. & Siddalingaiah, H. 1990. Comparison of *in situ* and satellite derived reflectances of Forbindels Glacier, Greenland. *International Journal of Remote Sensing* 11, 3, 493-504.

Hall, D.K., Chang, A.T.C., Foster, J.L., Benson, C.S. & Kovalik, W.M. 1989. Comparison of *in situ* and Landsat derived reflectance of Alaskan glaciers. *Remote Sensing of Environment* 28, 23-31.

Hall, D.K., Ormsby, J.P., Bindschadler, R.A. & Siddalingaiah, H. 1987. Characterization of snow and ice reflectance zones on glaciers using Landsat Thematic Mapper data. *Annals of Glaciology* 9, 104-108.

Henriksen, N. 1973. Regional mapping and palaeomagnetic and glaciological investigations in the Scoresby Sund region, central East Greenland. *Grønlands Geologiske Undersøgelse* Rapport 55, 42-47.

Henriksen, N. & Watt, W.S. 1968. Geological reconnaissance of the Scoresby Sund fjord complex. *Grønlands Geologiske Undersøgelse* Rapport, 15, 72-77.

Holtzscherer, J.J. & Bauer, A. 1954. *Contribution a la connaissance de l'Inlandis du Groenland,* No. 39, Association Internationale d'Hydrologie.

Jenkins, A. & Doake, C.S.M. 1991. Ice-ocean interaction on Ronne Ice Shelf, Antarctica. *Journal of Geophysical Research* 96, C1, 791-813.

Johnsen, S.J., Clausen, H.B., Dansgaard, W., Fuhrer, K., Gundestrup, N., Hammer, C.U., Iversen, P., Jouzel, J., Stauffer, B. & Steffensen, J.P. 1992a. Irregular glacial interstadials recorded in a new Greenland ice core.*Nature* 359, 6393, 311-313.

Johnsen, S.J., Clausen, H.B., Dansgaard, W., Gundestrup, N.S., Hansson, M., Jonsson, P., Steffensen, J.P. & Sveinbjørnsdottir, A.E. 1992b. A 'deep' ice core from East Greenland. *Meddelelser om Grønland* Geoscience, 29, 1-22.

Jonsson, S. & Hansson, M. 1990. Identification of annual layers in superimposed ice from Storoyjokulen in northeastern Svalbard. *Geografiska Annaler* 72A(1), 41-54.

Koch, L. 1945. The East Greenland ice. *Meddelelser om Grønland* 130, 3, 1-373.

Larsen, B. 1983. Geology of the Greenland-Iceland ridge in the Denmark Strait. In M.H.P. Bott, S. Saxov, M. Talwani, & J. Theide (Ed.), *Structure and Development of the Greenland-Scotland Ridge.* (425-444). Plenum Press, New York.

Lefauconnier, B. & Hagen, J.O. 1990. Glaciers and climate in Svalbard, statistical analysis and reconstruction of the Brogger glacier mass balance for the last 77 years. *Annals of Glaciology* 14, 148-152.

Lindell, L.T., Steinvall, O., Jonsson, H. & Claesson, T.H. 1985. Mapping of coastal water turbidity using Landsat imagery. *International Journal of Remote Sensing* 6, 629-642,

Lingle, C.S., Hughes, T.J. & Kollmeyer, R.C. 1981. Tidal flexure of Jakobshavns Glacier, West Greenland. *Journal of Geophysical Research* 86, 3960-3968.

Marienfeld, P. 1992. Recent sedimentary processes in Scoresby Sund, East Greenland. *Boreas* 21, 169-186.

Markham, B.L. & Barker, J.L. 1986. *Landsat MSS and TM post-calibration dynamic ranges, exoatmospheric reflectances and at-satellite temperatures,* Landsat Technical Notes No. 1, EOSAT.

Martin, P.J. & Sanderson, T.J.O. 1980. Morphology and dynamics of ice rises. *Journal of Glaciology* 25, 91, 33-45.

Massom, R.A. 1991. *Satellite Remote Sensing of Polar Regions* . Belhaven Press, London.

Meier, M.F. & Post, A.S. 1962. *Recent variations in mass net budgets of glaciers in western North America,* IASH Publication No. 58, International Association of Scientific Hydrology.

Meier, M.F. & Post, A.S. 1969. What are glacier surges? *Canadian Journal of Earth Sciences* 6, 4, 807-817.

Mienert, J., Andrews, J.T. & Milliman, J.D. 1992. The East Greenland continental margin (65°N) since the last deglaciation: changes in seafloor properties and ocean circulation. *Marine Geology* 106, 217-238.

Möller, P., Hjort, C. & Ingólfson, O. (Ed.) 1991 *The last interglacial-glacial cycle: preliminary report on the PONAM fieldwrk in Jameson Land and Scoresby Sund, East Greenland; Proceedings of the PONAM workshop in Skanör, Sweden* . Department of Quaternary Geology, Lund University, Lund.

O'Brien, H.W. & Munis, R.H. 1975. *Red and near-infrared spectral reflectance of snow,* Research Report No. 332, US Army Cold Regions Research and Engineering Laboratory.

Oerlemans, J. (Ed.) 1987 *Glacier fluctuations and climatic change. Proceedings of the symposium on glacier fluctuations and climatic change, held in Amsterdam, 1–5 june 1987* . Kluwer Academic Publishers, Dordrecht.

Oerlemans, J. 1991. Explicit simulation of the mass balance of the Greenland Ice Sheet. In V.M. Kotlyakov, A. Ushakov, & A. Glazovsky (Ed.), *Glaciers-Ocean-Atmosphere Interactions*, IAHS Publication No. 208 . St Petersburg: Institute of Hydrology, Wallingford, Oxfordshire.

Oerlemans, J. 1992. Climate sensitivity of glaciers in southern Norway: application of an energy balance model to Nigardsbreen, Hellstugbreen and Alfotbreen. *Journal of Glaciology* 38, 129, 223-232.

Oeschger, H. & Langway, C.C. (Ed.) 1989 *The Environmental Record in Glaciers and Ice Sheets. Report of the Dahlem Workshop, Berlin, March 13-18, 1988* . John Wiley & Sons, Chichester etc.

Olesen, O.B. & Reeh, N. 1969. Preliminary report on glacier observations in Nordvestfjord, East Greenland. *Grønlands Geologiske Undersøgelse* 21, 41-53.

Østrem, G. 1975. ERTS data in glaciology - an effort to monitor glacier mass balance from satellite imagery. *Journal of Glaciology* 15, 73, 403-415.

Paterson, W.S.B. 1981. *The Physics of Glaciers* (2nd ed.). Pergamon Press, Oxford.

Paterson, W.S.B. & Waddington, E.D. 1984. Past precipitation rates derived from ice core measurements: methods and data analysis. *Reviews of Geophysics and Space Physics* 22, 2, 123-130.

Pelto, M.S. 1987. Mass balance of south-east Alaska and north-west British Columbia glaciers from 1976 to 1984: methods and results. *Annals of Glaciology* 9, 189-194.

Powell, R.D. 1984. Glacimarine processes and inductive lithofacies modelling of ice shelf and tidewater glacier sediments based on Quaternary examples. *Marine Geology* 57, 1-52.

Powell, R.D. 1990. Glacimarine processes at grounding-line fans and their growth to ice-contact deltas. In J.A. Dowdeswell & J.D. Scourse (Ed.), *Glacimarine Environments: Processes and Sediments.* (53-74). The Geological Society, London.

Powell, R.D. & Molnia, B.F. 1989. Glacimarine sedimentary processes, facies and morphology of the south-east Alaska shelf and fjords. *Marine Geology* 85, 359-390.

Putnins, P. 1970. The climate of Greenland. In S. Orvig (Ed.), *Climates of the Polar Regions.* Elsevier, Amsterdam etc.

Radok, U., Barry, R.G., Jenssen, D., Keen, R.A., Kiladis, G.N. & McInnes, B. 1982. *Climatic and physical characteristics of the Greenland ice sheet,* No. Cooperative Institute for Research in Environmental Sciences, University of Boulder, Colorado.

Raymond, C.F. 1987. How do glaciers surge? A review. *Journal of Geophysical Research* 92, B9, 9121-9134.

Reeh, N. 1985. Greenland ice-sheet mass balance and sea-level change. In *Glaciers, ice sheets and sea level: effect of a CO_2-induced climatic change.* US Department of Energy.

Reeh, N. 1989. Dynamic and climatic history of the Greenland ice sheet. In R.J. Fulton (Ed.), *Quaternary Geology of Canada and Greenland.* Geological Survey of Canada also Geological Society of America.

Reeh, N. & Olesen, O.B. 1986. Velocity measurements on Daugaard-Jensen gletscher, Scoresby Sund, East Greenland. *Annals of Glaciology* 8, 146-150.

Ridley, J.K., Laxon, S., Rapley, C.G. & Mantripp, D. 1992. Topography of Antarctic ice sheet mapped with the ERS-1 radar altimeter. *Earth Observation Quarterly* 37-38, 14-15.

Ritchie, J.C. & Cooper, C.M. 1988. Comparison of measured suspended sediment concentrations with suspended sediment concentrations estimated from Landsat MSS data. *International Journal of Remote Sensing* 9, 3, 379-387.

Ritchie, J.C., Cooper, C.M. & Yongqing, J. 1987. Using Landsat multispectral data to estimate suspended sediments in Moon Lake, Mississippi. *Remote Sensing of Environment* 23, 65-81.

Ritchie, J.C., Schiebe, F.R. & McHenry, J.R. 1976. Remote sensing of suspended sediments in surface waters. *Photogrammetric Engineering and Remote Sensing* 42, 12, 1539-1545.

Robin, G.de Q. 1977. Ice cores and climatic change. *Philosophical Transactions of the Royal Society of London* B, 280, 143-168.

Robinove, C.J. 1982. Computation with physical values from Landsat digital data. *Photogrammetric Engineering and Remote Sensing* 48, 5, 781-784.

Rucklidge, J. 1966. Observations of hollows in the snow surface of Torv Gletscher, East Greenland. *Journal of Glaciology* 6, 45, 446-449.

Rutishauser, H. 1971. Observations on a surging glacier in East Greenland. *Journal of Glaciology* 10, 59, 227-236.

Schytt, V. 1955. *Glaciological investigations in the Thule Ramp area,* Technical Report No. 28, U.S. Army Snow Ice and Permafrost Research Establishment.

Sharma, G.D. 1979. *The Alaskan Shelf: Hydrographic, Sedimentary and Geochemical Environment* . Springer-Verlag, New York.

Sharp, M. 1988. Surging glaciers: behaviour and mechanisms. *Progress in physical geography* 12, 3, 349-370.

Sydor, M. 1980. Remote sensing of particulate concentrations in water. *Applied Optics* 19, 16, 2794-2800.

Syvitski, J.P.M., Burrell, D.C. & Skei, J.M. 1987. *Fjords: Processes and Products* . Springer-Verlag, New York.

USGS 1984. *Landsat 4 Data Users Handbook* . US Geological Survey, National Oceanic and Atmospheric Administration.

USGS & NOAA 1982. *Index to Landsat worldwide referencing systems (WRS)* .

Verdin, J.P. 1985. Monitoring water quality conditions in a large western reservoir with Landsat imagery. *Photogrammetric Engineering and Remote Sensing* 51, 3, 343-353.

Weidick, A. 1985. *The ice cover of Greenland,* Gletscher-Hydrologiske Meddelelser No. 85/4, Grønlands Geologiske Undersøgelse, København.

Weidick, A. 1988. Surging glaciers in Greenland - a status. *Grønlands Geologiske Undersøgelse Rapport* 140, 106-110.

Weidick, A., Bøggild, C.E. & Knudsen, N.T. 1992. *Glacier inventory and atlas of West Greenland,* Rapport No. 158, Grønlands Geologiske Undersøgelse.

Williams, R.S. 1987. Satellite remote sensing of Vatnajökull, Iceland. *Annals of Glaciology* 9, 127-135.

Williams, R.S., Hall, D.K. & Benson, C.S. 1991. Analysis of glacier facies using satellite techniques. *Journal of Glaciology* 37, 125, 120-128.

Wiscombe, W.J. & Warren, S.G. 1980. A model for the spectral albedo of snow; I: Pure snow. *Journal of the Atmospheric Sciences* 37, 12, 2712-2733.

Yamanouchi, T. 1983. Variations of incident solar flux and albedo on the solar zenith angle and cloud cover, at Mizuho Station, Antarctica. *Journal of the Meteorological Society of Japan* 61, 6, 879-893.

Zwally, H.J. 1989a. Growth of Greenland ice sheet: interpretation. *Science* 246, 4937, 1589-1591.

Zwally, H.J. 1989b. Growth of Greenland ice sheet: measurement. *Science* 246, 4937, 1587-1589.

Zwally, H.J., Brenner, A.C., Major, J.A., Bindschadler, R.A. & Marsh, J.G. 1990. 'Greenland Ice Sheet: is it growing or shrinking?' Response. *Science* 248, 4953, 288-289.

Sharma, G.D. 1979. *The Alaskan Shelf: Hydrographic, Sedimentary and Geochemical Environment* . Springer-Verlag, New York.

Sharp, M. 1988. Surging glaciers: behaviour and mechanisms. *Progress in physical geography* 12, 3, 349-370.

Sydor, M. 1980. Remote sensing of particulate concentrations in water. *Applied Optics* 19, 16, 2794-2800.

Syvitski, J.P.M., Burrell, D.C. & Skei, J.M. 1987. *Fjords: Processes and Products* . Springer-Verlag, New York.

USGS 1984. *Landsat 4 Data Users Handbook* . US Geological Survey, National Oceanic and Atmospheric Administration.

USGS & NOAA 1982. *Index to Landsat worldwide referencing systems (WRS)* .

Verdin, J.P. 1985. Monitoring water quality conditions in a large western reservoir with Landsat imagery. *Photogrammetric Engineering and Remote Sensing* 51, 3, 343-353.

Weidick, A. 1985. *The ice cover of Greenland,* Gletscher-Hydrologiske Meddelelser No. 85/4, Grønlands Geologiske Undersøgelse, København.

Weidick, A. 1988. Surging glaciers in Greenland - a status. *Grønlands Geologiske Undersøgelse Rapport* 140, 106-110.

Weidick, A., Bøggild, C.E. & Knudsen, N.T. 1992. *Glacier inventory and atlas of West Greenland,* Rapport No. 158, Grønlands Geologiske Undersøgelse.

Williams, R.S. 1987. Satellite remote sensing of Vatnajökull, Iceland. *Annals of Glaciology* 9, 127-135.

Williams, R.S., Hall, D.K. & Benson, C.S. 1991. Analysis of glacier facies using satellite techniques. *Journal of Glaciology* 37, 125, 120-128.

Wiscombe, W.J. & Warren, S.G. 1980. A model for the spectral albedo of snow; I: Pure snow. *Journal of the Atmospheric Sciences* 37, 12, 2712-2733.

Yamanouchi, T. 1983. Variations of incident solar flux and albedo on the solar zenith angle and cloud cover, at Mizuho Station, Antarctica. *Journal of the Meteorological Society of Japan* 61, 6, 879-893.

Zwally, H.J. 1989a. Growth of Greenland ice sheet: interpretation. *Science* 246, 4937, 1589-1591.

Zwally, H.J. 1989b. Growth of Greenland ice sheet: measurement. *Science* 246, 4937, 1587-1589.

Zwally, H.J., Brenner, A.C., Major, J.A., Bindschadler, R.A. & Marsh, J.G. 1990. 'Greenland Ice Sheet: is it growing or shrinking?' Response. *Science* 248, 4953, 288-289.

APPENDIX 1

On the following pages, a print of band 4 (0.8 to 1.1 μm) of each of the 16 scenes is shown, arranged from south to north. The location of each scene relative to the East Greenland coast is illustrated in Figure 3.2. Each scene represents an area of 185 km by 185 km on the ground.

227/012 20th September 1988 Solar elevation 21.8 deg. Fig. 1

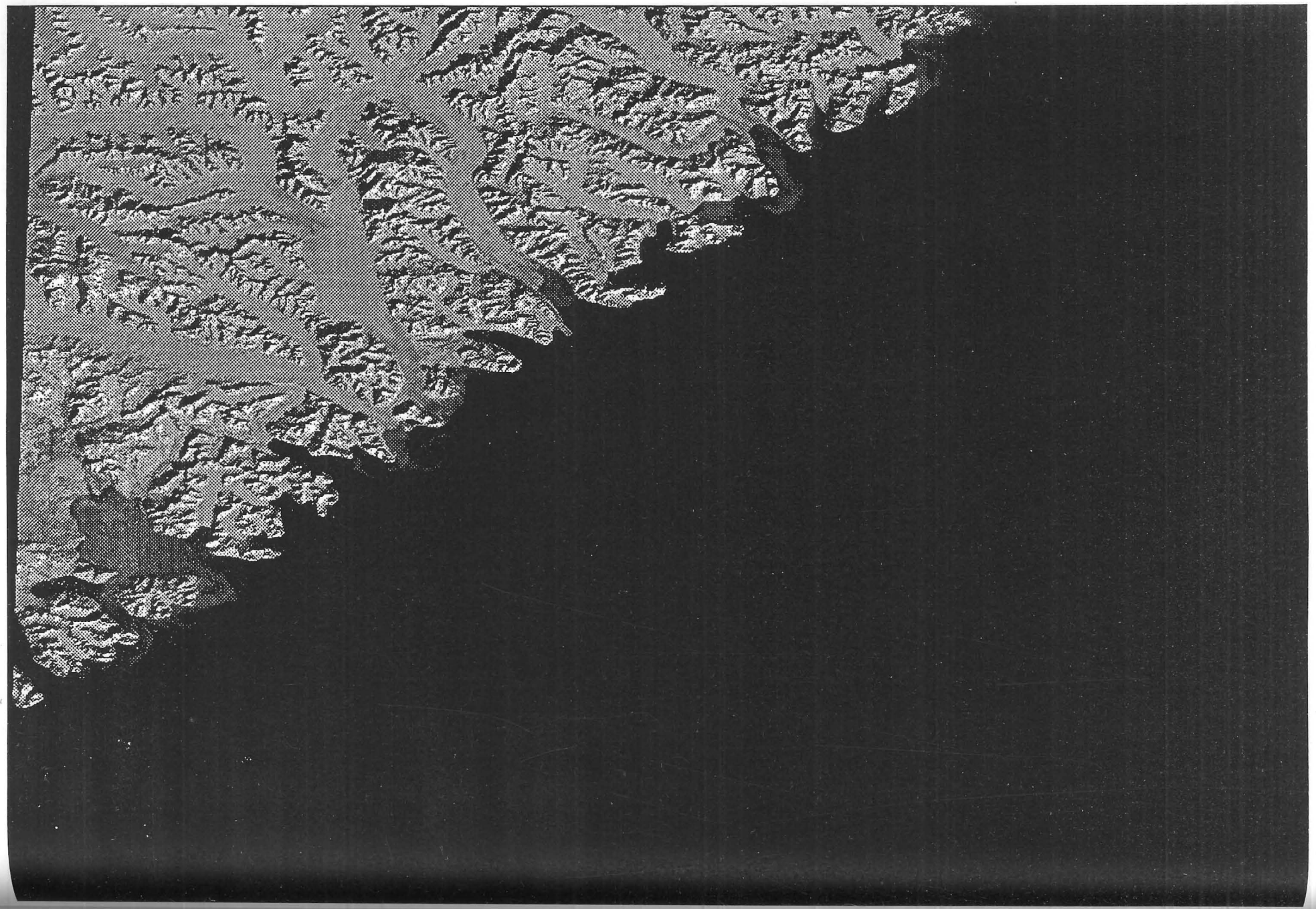

230/012 4th September 1986 Solar elevation 27.6 deg. Fig. 2

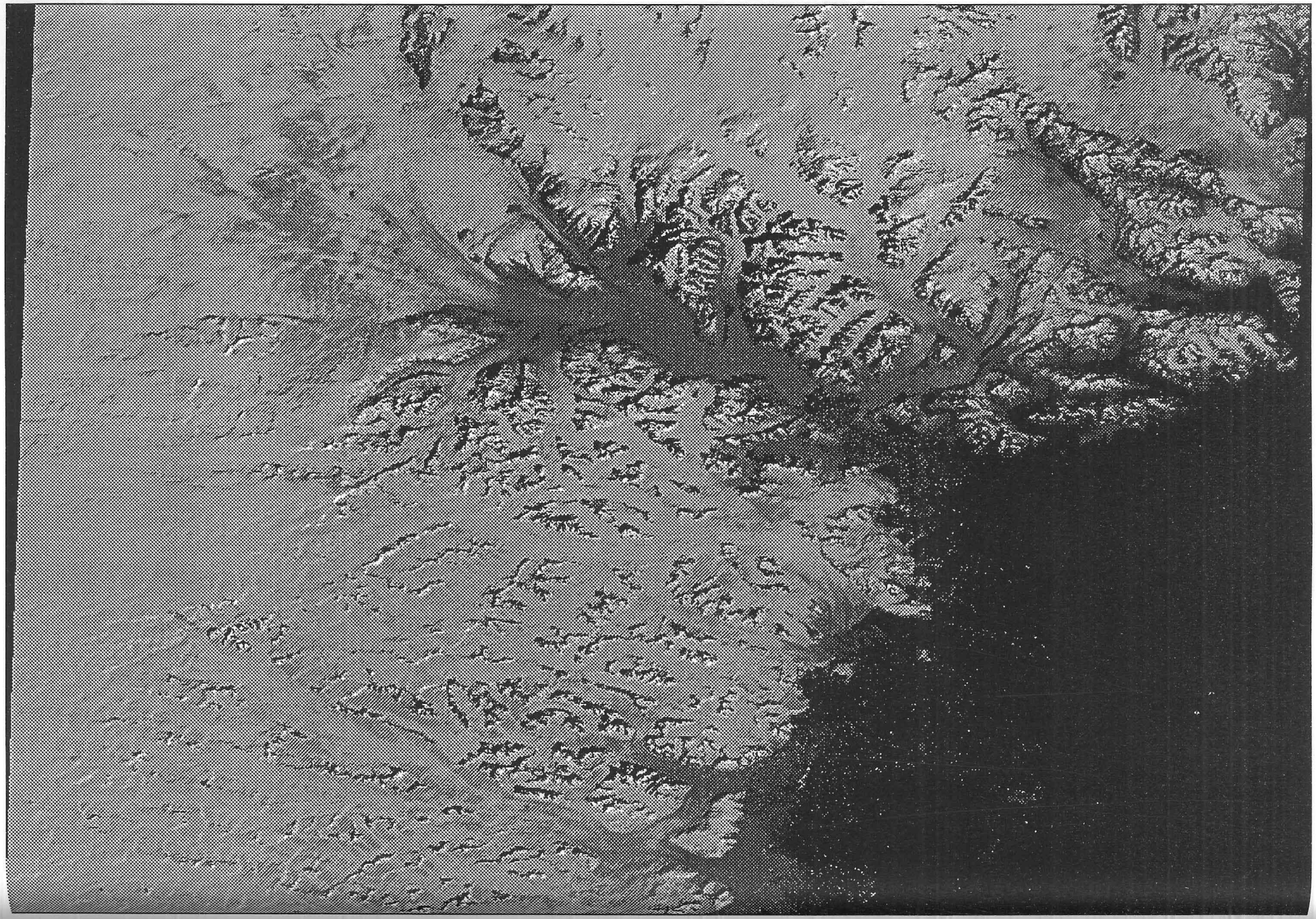

226/011 8th September 1989 Solar elevation 25.1 deg. Fig. 3

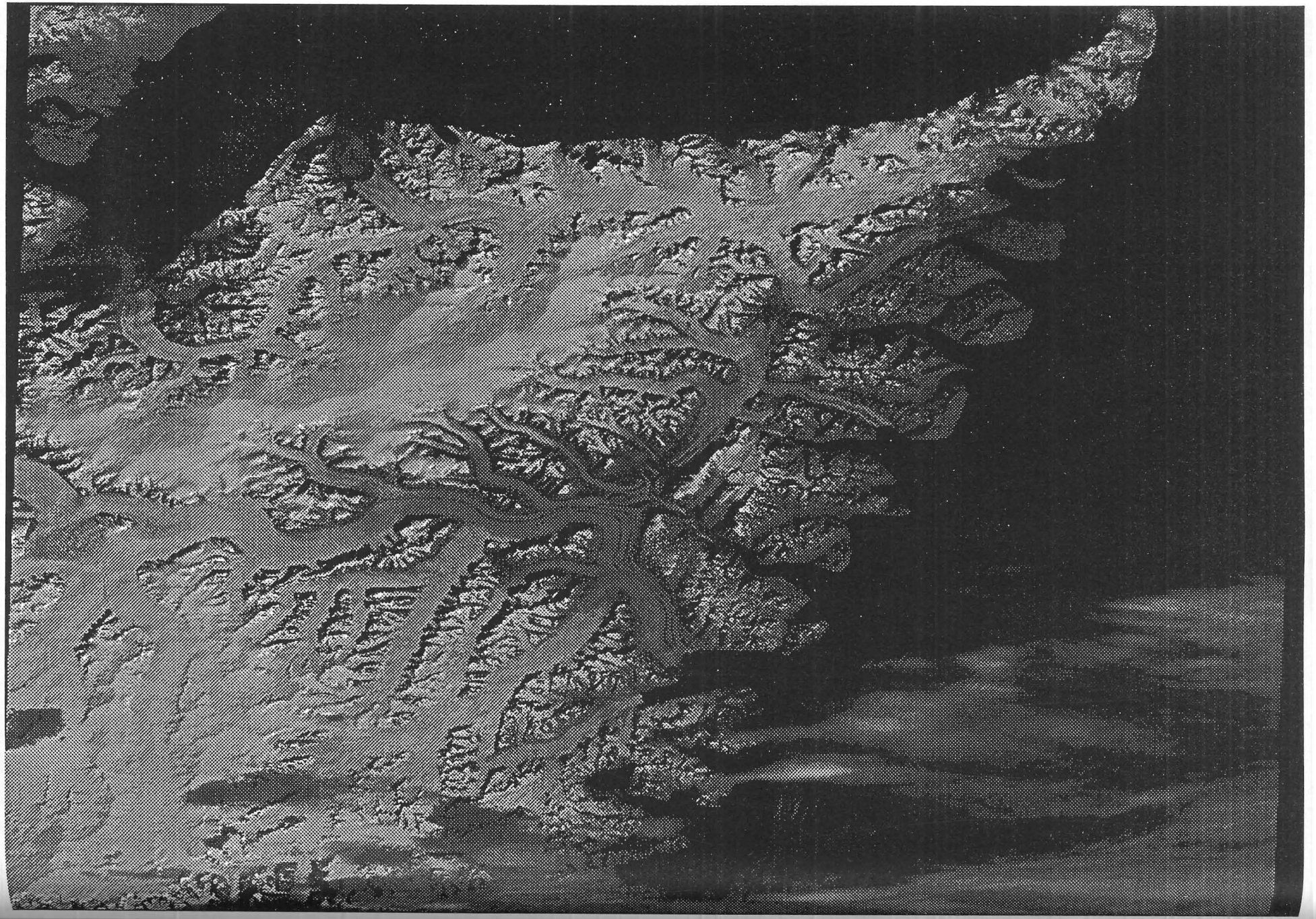

226/011 10th August 1987 Solar elevation 35.2 deg. Fig. 4

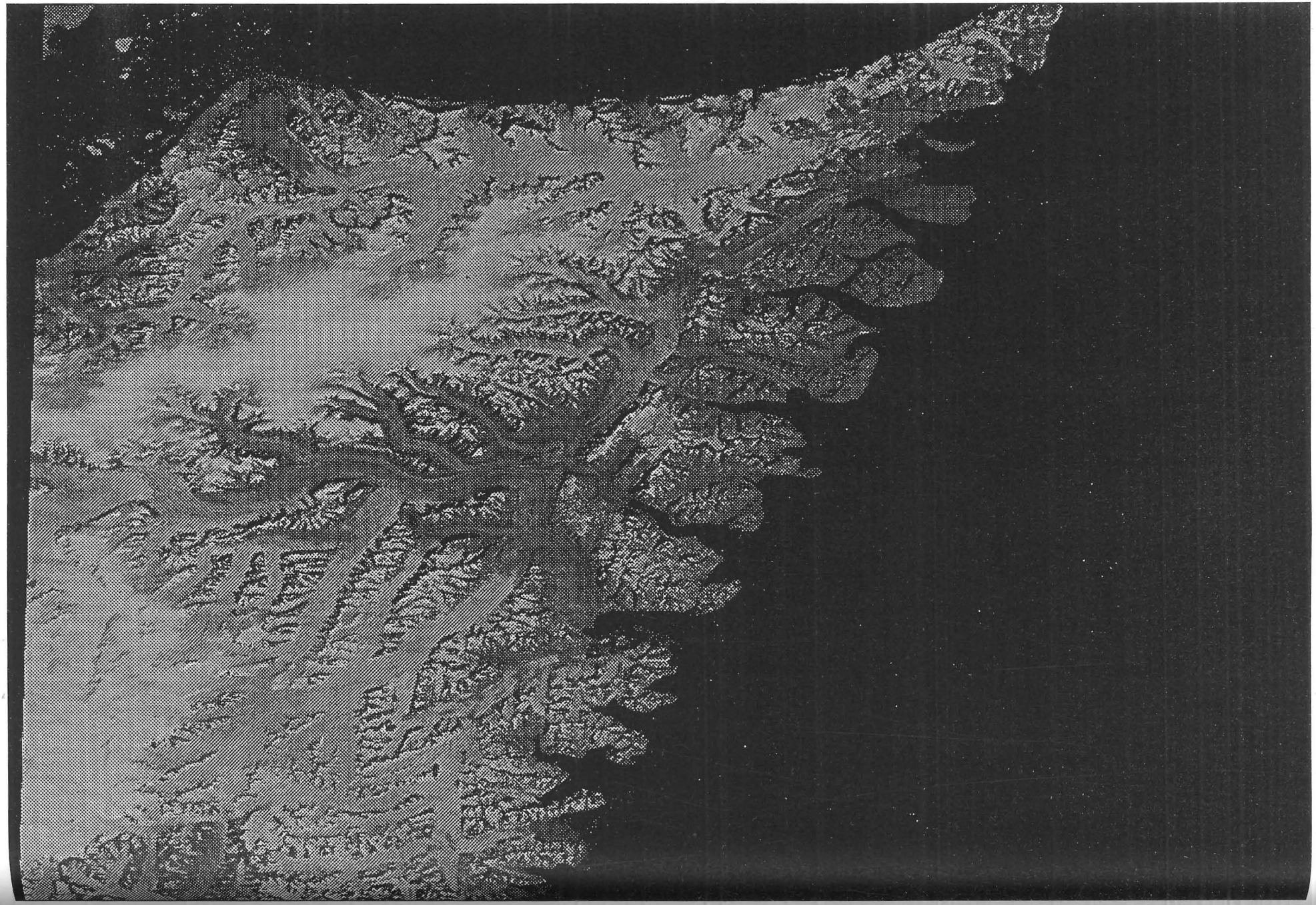

229/011 31st August 1987 Solar elevation 28.3 deg. Fig. 5

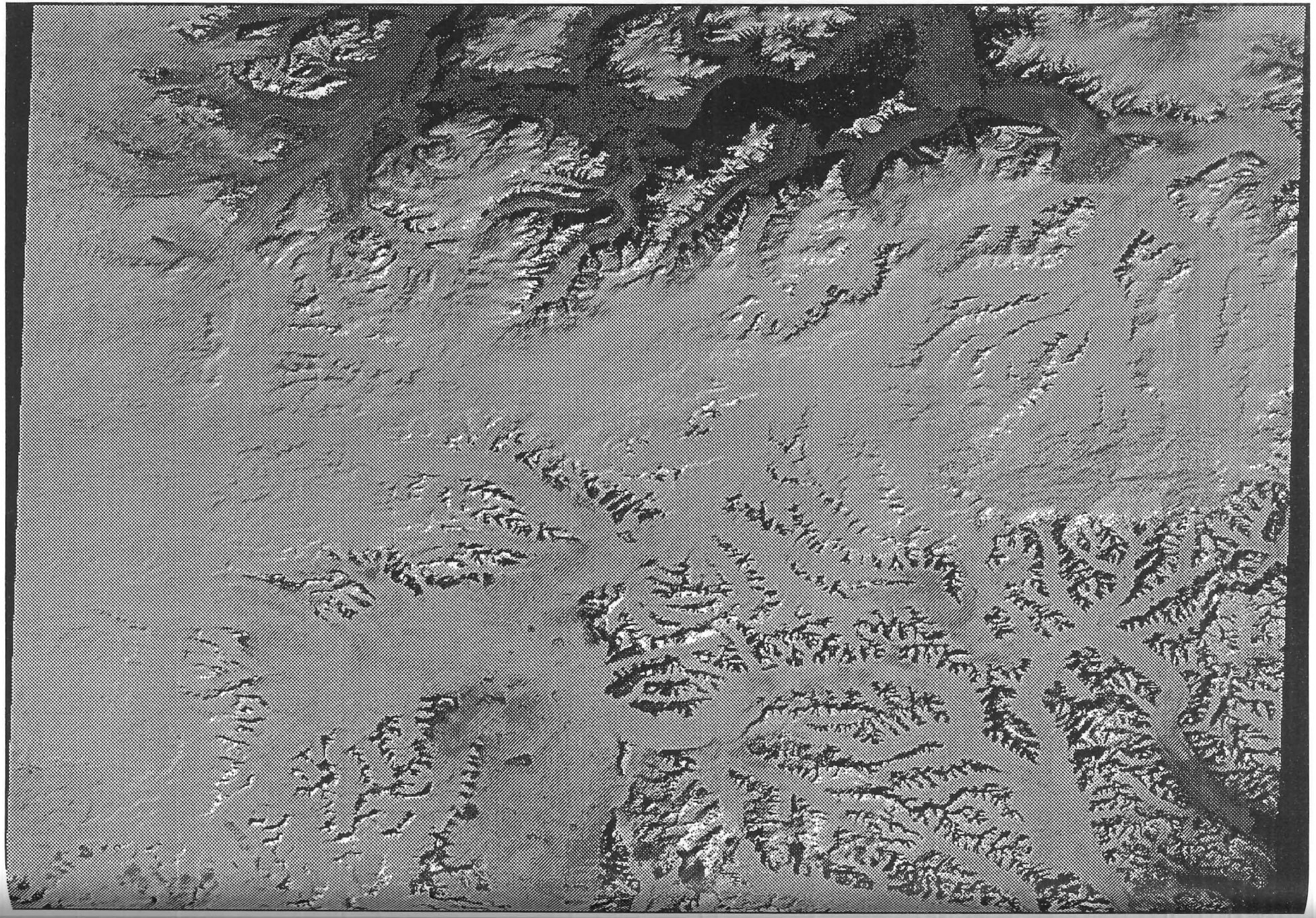

230/011 4th September 1986 Solar elevation 27.6 deg. Fig. 6

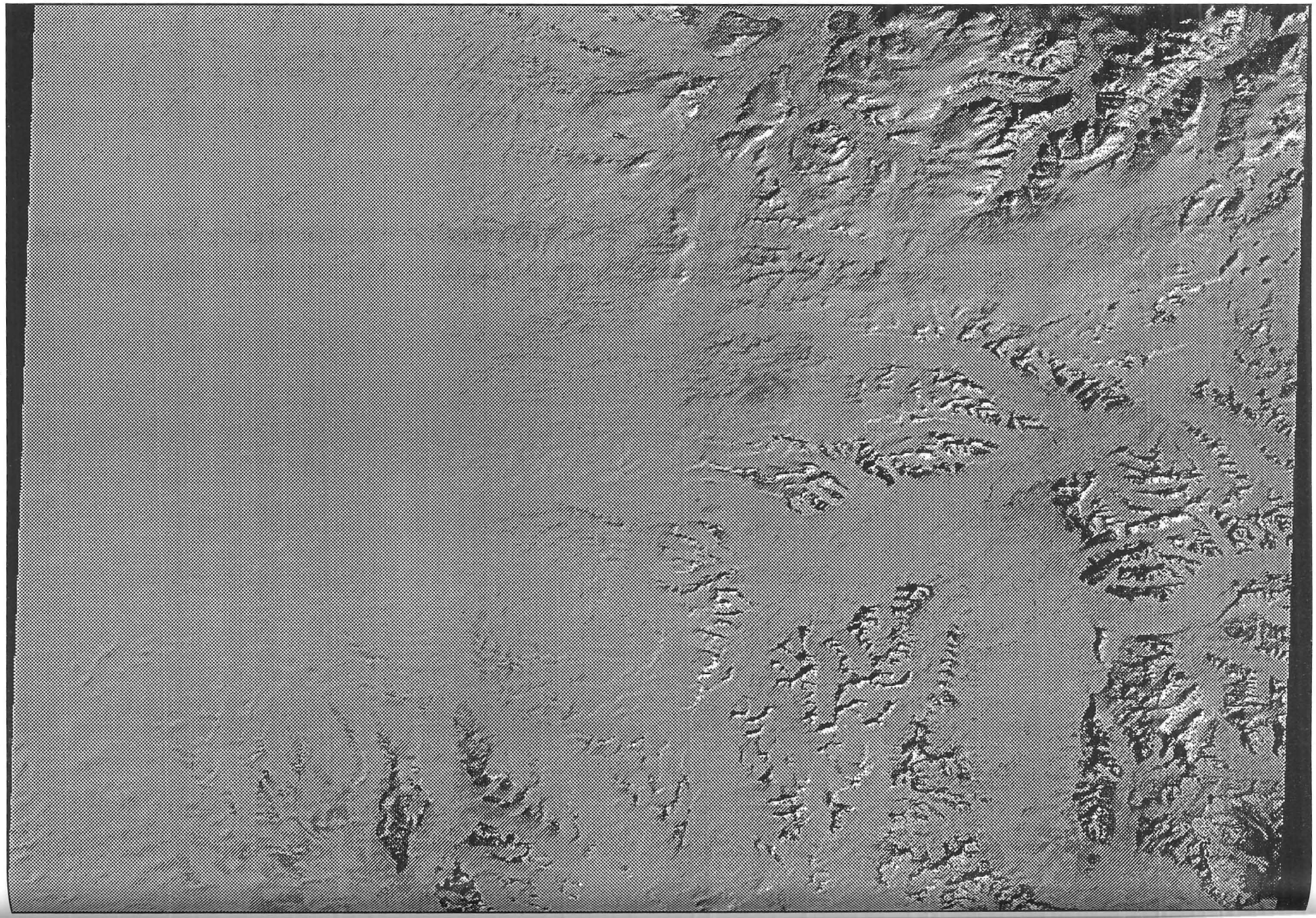

227/010 6th August 1989 Solar elevation 35.0 deg. Fig. 7

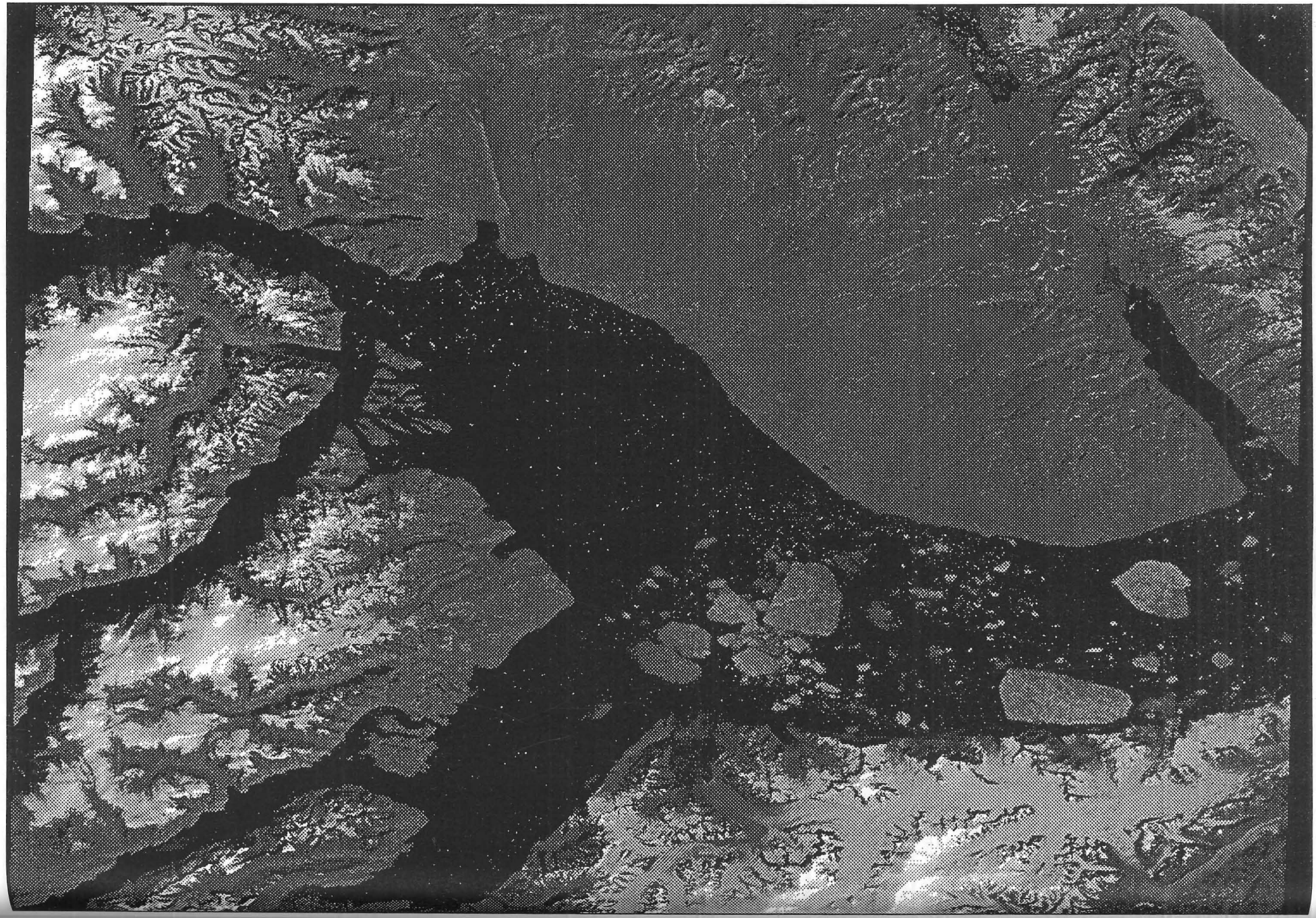

227/010 20th September 1988 Solar elevation 19.4 deg. Fig. 8

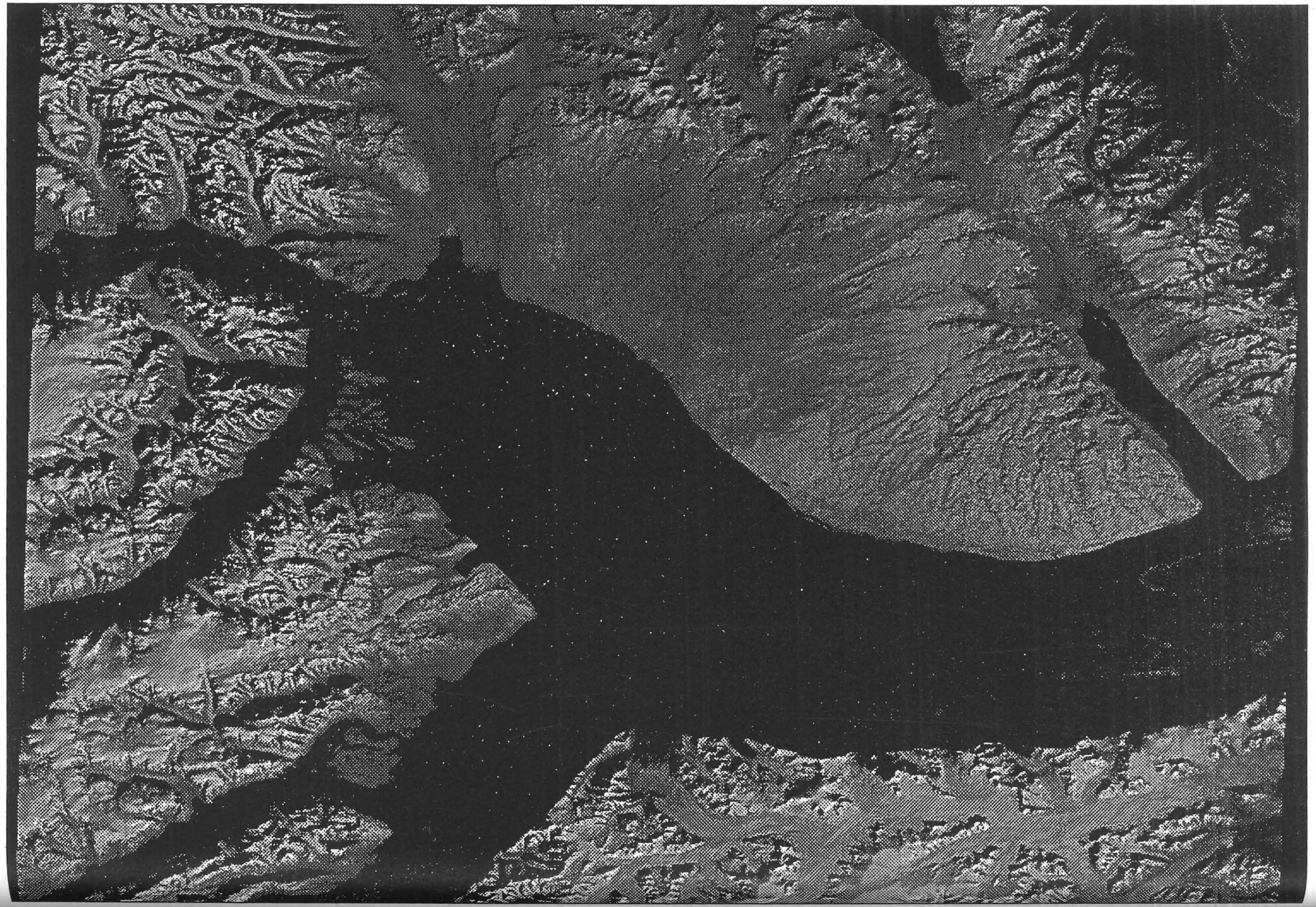

228/010 24th August 1987 Solar elevation 29.6 deg. Fig. 9

229/010 30th June 1988 Solar elevation 41.8 deg. Fig. 10

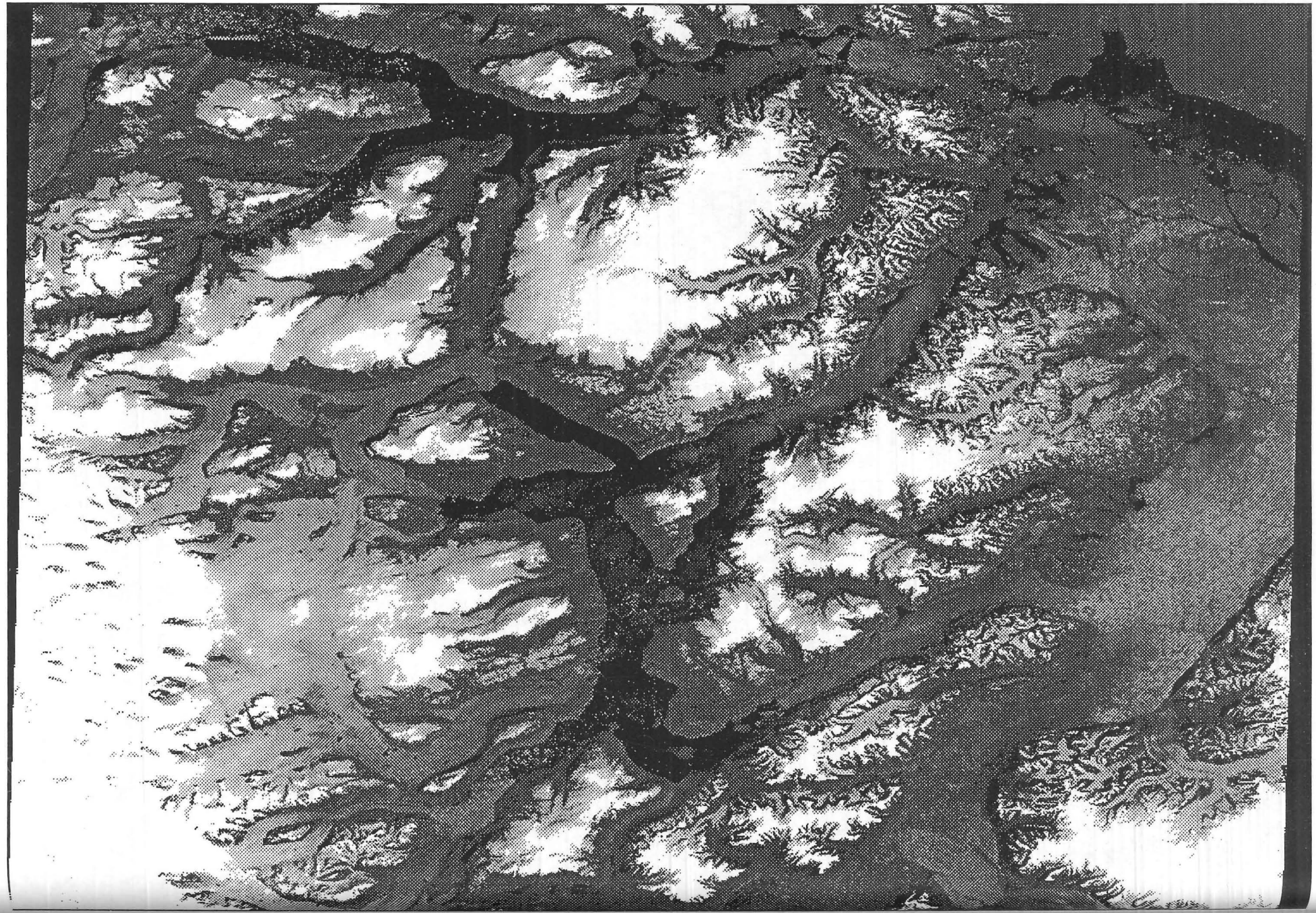

230/010 22nd August 1987 Solar elevation 30.2 deg. Fig. 11

228/009 24th August 1987 Solar elevation 28.4 deg. Fig. 12

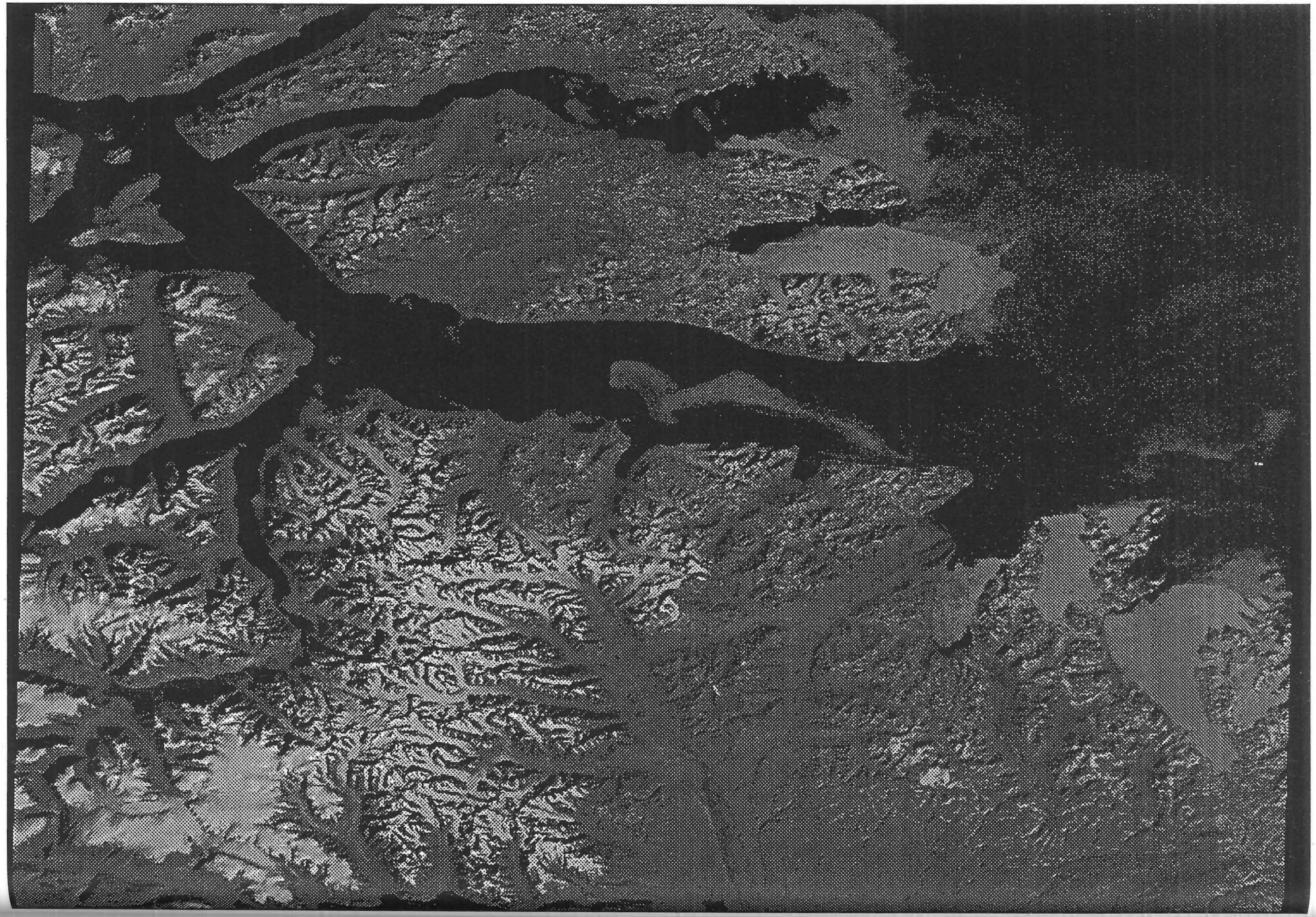

230/009 22nd August 1987 Solar elevation 29.1 deg. Fig. 13

229/008 15th August 1987 Solar elevation 30.2 deg. Fig. 14

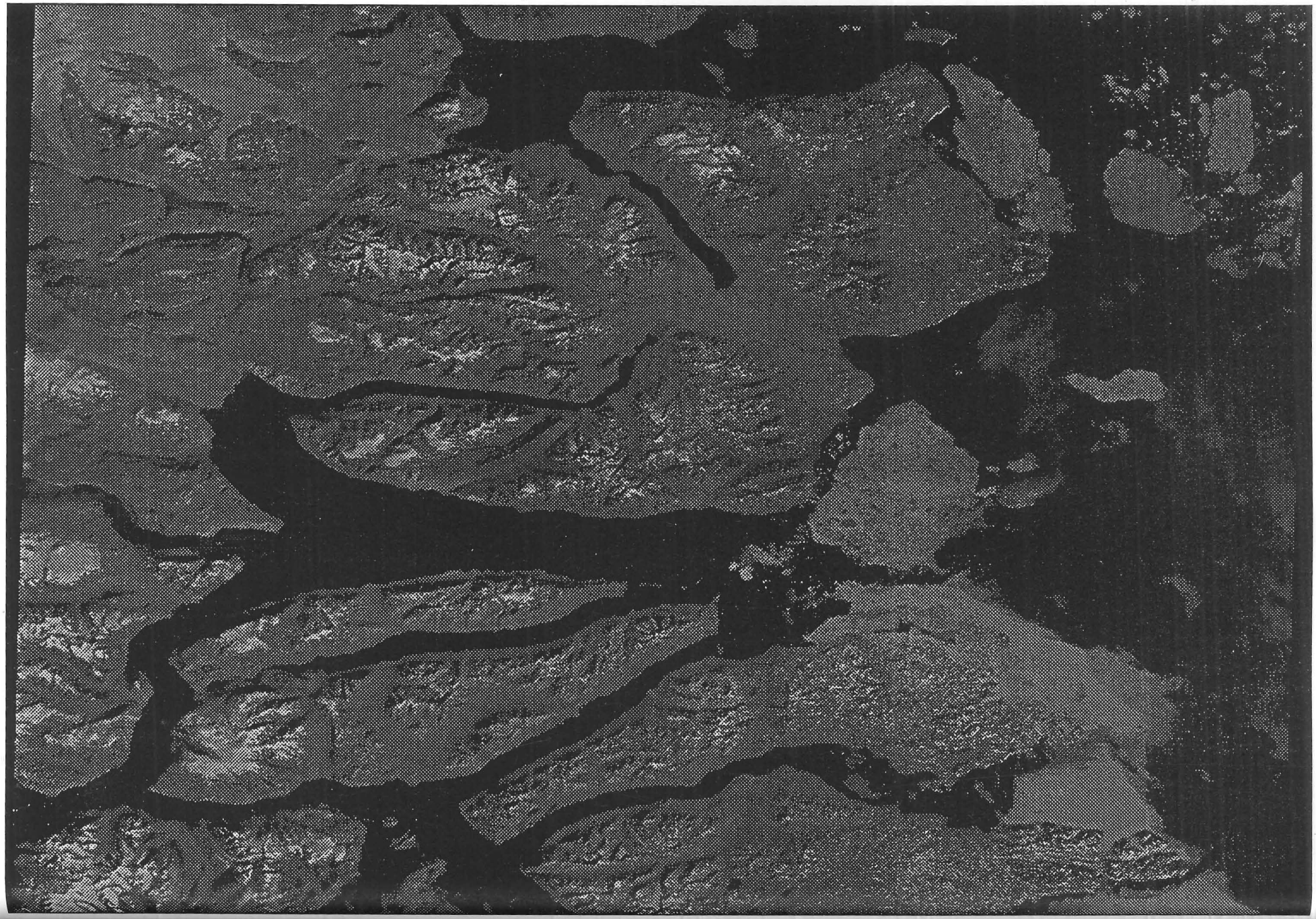

231/008 29th August 1987 Solar elevation 25.5 deg. Fig. 15

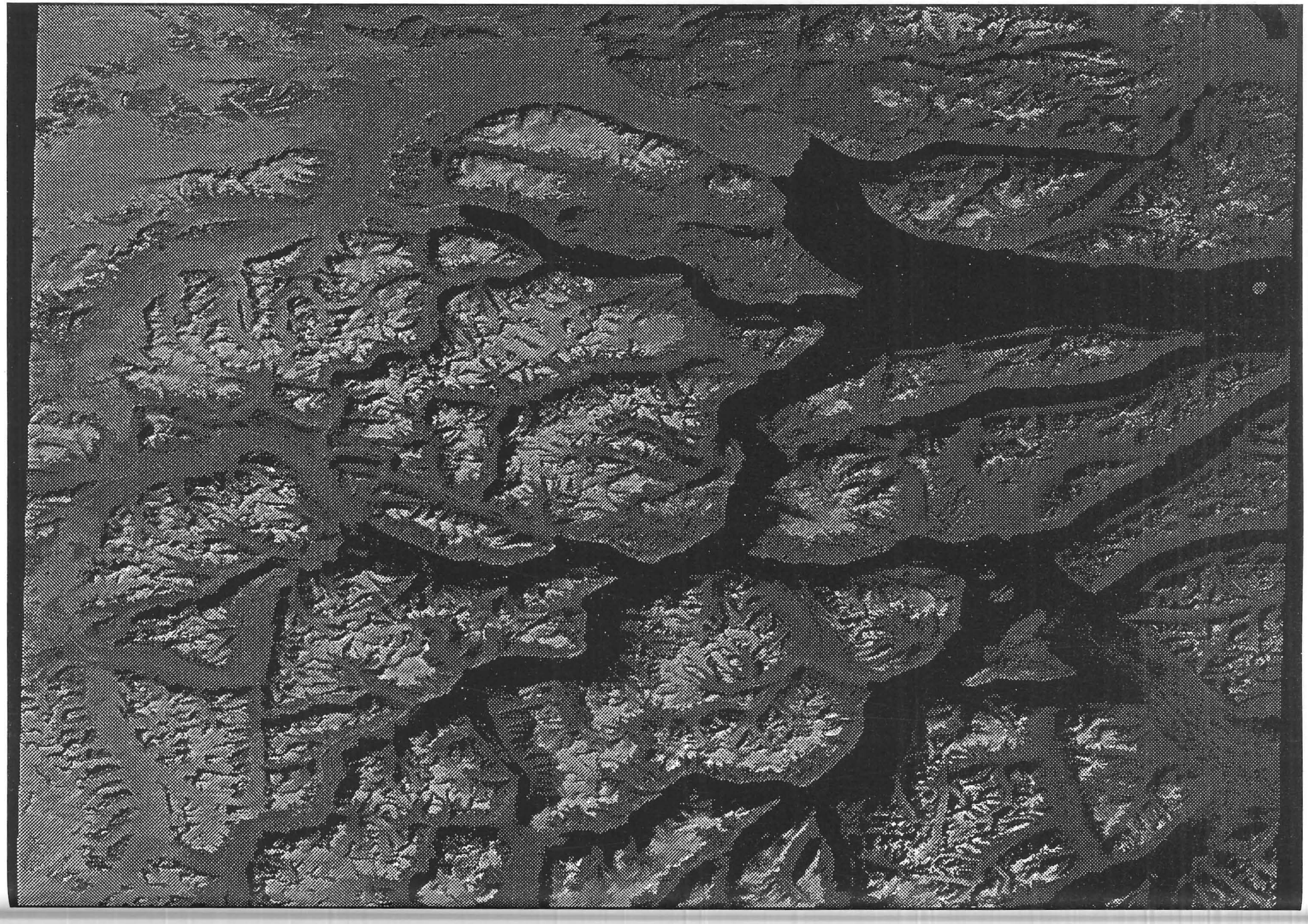

230/007 22nd August 1987 Solar elevation 26.8 deg. Fig. 16